1994

Environmentally enhanced thermal fatigue and cracking of a gamma- based titanium aluminide alloy

William D. Dunfee
Lehigh University

AUTHOR:

Dunfee, William D.

TITLE:

Environmentally Enhanced Thermal Fatigue and Cracking of a Gamma-Based Titanium Aluminide Alloy

DATE: May 29, 1994

Environmentally Enhanced Thermal Fatigue and Cracking of a Gamma-based Titanium Aluminide Alloy

by

William D. Dunfee

A Thesis

Presented to the Graduate and Research Committee

of Lehigh University

in Candidacy for the Degree of

Master of Science

in

Applied Mechanics

Lehigh University

1994

This thesis is accepted and approved in partial fulfillment of the requirements for the degree of Master of Science in Applied Mechanics.

May 16, 1994

Date

Dr. Robert P. Wei

Thesis Advisor

Dr. Robert P. Wei

Chairman of Department

ACKNOWLEDGMENTS

I would like to express my sincere gratitude to my thesis advisor Dr. Robert P. Wei for his guidance and support which made this work possible. Much thanks also goes to Dr. Ming Gao for his generous assistance with the thermal fatigue experiments and fractographic studies. I would also like to thank Mr. Carl Miller for his technical expertise which aided in the development of the experimental apparatus, and Mr. Beizhi Zhou for his polishing skills.

Finally, many thanks go to Lehigh University for offering financial support in the forms of a fellowship and a teaching assistantship, and also to Motoren-und-Turbinen Union of Germany and Dr. Robert P. Wei for a research assistantship.

TABLE OF CONTENTS

LIST OF TABLES AND FIGURES

ABSTRACT

To critically assess the thermal fatigue resistance of γ-titanium aluminides in gaseous environments, thermal fatigue test equipment and methodologies were developed. The equipment consists of a rigid frame with fixed grips and an environmental chamber. Direct electrical resistance heating was used to heat the specimen, and cooling was accomplished by a chilled gas jet. This type of thermal control allows for rapid heating and cooling rates and excellent repeatability between cycles.

Tests were performed on a Ti-48Al-2Cr alloy in hydrogen, air, and helium (as an inert reference) with temperature cycling ranges of 25 to 900, 750, and 550°C, and a prestress of 241 MPa (50% of the material's room temperature yield strength). At 900°C, fatigue lives were less than 30 cycles in hydrogen and ranged as low as 2,100 cycles in air, but no failures were observed in helium. Failure in hydrogen was found to be a result of rapid growth of numerous cracks developing over the entire specimen, while failure in air was due to the growth of a single main crack. Fractographic analysis revealed that grain boundaries, cleavage planes, and α_2/γ interfaces are the preferred cracking sites in hydrogen. For thermal fatigue in air, the fracture surface showed distinct nucleation, propagation, and rapid fracture zones. The propagation zone was essentially transgranular and non-crystallographic.

Hydrogen attack was also evident at the lower cycling temperatures of 750 and 550°C, but was in competition with residual oxygen. In the early cycles, hydrogen attacked the material, producing cracks and pits,

while oxygen attempted to react with the surface to form a protective Al_2O_3 oxide. Lifetime appears to be a strong function of temperature and the partial pressure of oxygen at temperatures below 800°C.

These results suggest that γ alloys are severely embrittled while thermally cycled in hydrogen, but suffer mainly from oxidation-assisted cracking in air. Since the catastrophic-type failure observed here in hydrogen was not observed in conventional tests, studying the combined actions of thermal cycling and environmental degradation is essential for the critical assessment of materials for high temperature applications.

CHAPTER ONE

INTRODUCTION AND BACKGROUND

1.1 INTRODUCTION

Titanium aluminides are among the most attractive new materials which have surfaced in the ongoing quest for the "next generation" of advanced aerospace materials. The new materials required for future turbine engines and hypersonic aircraft need to be lighter than the current nickel-based superalloys, while retaining the same level of mechanical and oxidation resistance properties. Future turbine engines will be required to operate at higher gas and metal temperatures to improve engine efficiency, thus saving fuel [1]. Also, lighter weight components will provide a higher thrust-to-weight ratio, reduce stresses in rotating parts, and increase the life span of disks, shafts, and the bearing support structure [1,3]. The titanium-based alloys currently in use, although providing a substantial weight savings over nickel-based superalloys, are limited in operation to approximately 600°C due to strength and oxidation problems [3].

1.1.1 Titanium Aluminides

The most promising materials to meet these needs are the titanium aluminides, mainly the alpha-2 (Ti_3Al) and gamma (TiAl) based alloys [1-3]. The ordered intermetallic structure of these alloys provides excellent high-temperature retention of the material's elastic modulus and strength, while also allowing good creep and fatigue resistance [1,3].

Also, these materials are less than half as dense as the nickel based superalloys [3]. Due to these advantages, titanium aluminides have been targeted for use in the National Aerospace Plane (NASP), the Integrated High Performance Turbine Engine Technology (IHPTET) program, and other advanced programs [2]. In the hypersonic NASP, titanium aluminides are being considered for a myriad of uses including skin surfaces, internal structure, rocket nozzles, and various engine parts such as high pressure turbine disks and compressor blades [2].

However, several obstacles remain to be overcome before these materials can be put into service: mainly, low ductility and fracture toughness at ambient temperatures, limited oxidation resistance at elevated temperatures, and the tendency for hydrogen embrittlement at both ambient and elevated temperatures [1-8]. The first concern, room-temperature brittleness, is an obvious drawback since materials used in critical locations need to have a damage tolerance to avoid sudden rapid failure. The second two problems, oxidation and hydrogen embrittlement, become concerns when considering the intended uses for the material, i.e., in high-temperature air or hydrogen environments. For instance, titanium aluminide components in the NASP are expected to be in contact with the degrading effects of both the Earth's atmosphere and the hydrogen fuel, in states ranging from cryogenic to high pressure combustion and exhaust [2]. In this respect, the gamma titanium aluminide alloy holds a distinct advantage over the alpha-2 alloy in that it has a higher oxidation resistance and a significantly lower hydrogen solubility [2,3,9]. Also, studies have found that TiAl does not form embrittling hydrides, whereas in Ti_3Al hydride formation is well

documented [2,9]. Finally, the gamma alloys are lighter and stiffer than the alpha-2 alloys, although they are less ductile at room temperature [1,3].

1.1.2 Thermal Fatigue

When considering the intended applications for γ-TiAl based alloys, it is apparent that the components will undergo thermal cycling while in service within hostile environments. These environments may enhance the degrading effects of thermal cycling. Thus it is necessary to evaluate the material's resistance to these conditions before it can be placed into service.

Two aspects of the degradation problem require attention, both of which are engendered by the combined action of load and thermal cycling [10-13]. The first is referred to thermal-mechanical fatigue, where mechanical fatigue is superposed on cyclic temperature fluctuations. The second, thermal fatigue, refers to the cyclic stresses solely induced by restricted thermal expansion and contraction. For the present study, emphasis is placed on the second aspect, i.e., thermal fatigue.

Spera [10] defined thermal fatigue as the "gradual deterioration and eventual cracking of a material by alternate heating and cooling during which free thermal expansion is partially or completely constrained". These constraints can be of two types, external and internal. An external constraint is produced by boundary forces on the material which inhibit free thermal expansion or contraction. An internal constraint is produced by either thermal gradients within the material or by two dissimilar materials (having different coefficients of

expansion) in intimate contact with each other, such as within a multiple phase or composite material [10,14]. Both types of constraints prevent free expansion or contraction within material elements, producing stresses which can eventually initiate and propagate a fatigue crack.

As with pure mechanical fatigue, thermal fatigue damage to the material accumulates with each cycle. In most cases, 90% of the thermal fatigue life of the material consists of the development of cumulative damage to the microstructure, with cracks nucleating and propagating in the last 10% of the life [14]. Typically, thermal fatigue cracks nucleate in under 50,000 cycles, thus classifying thermal fatigue as "low-cycle fatigue" [10]. Again, like mechanical fatigue, thermal fatigue damage and crack propagation can be accelerated by the actions of a hostile environment. Although limited studies have shown that the tensile and fracture properties of γ-TiAl can be degraded by hydrogen and hydrogenous gases at both ambient and elevated temperatures [2,3,5-8], little has been done to examine the combined effects of thermal cycling and environment on the material's degradation. It is important, therefore, to assess the material's ability to resist environmental degradation while undergoing thermal cycling.

1.2 RELATED WORK ON TITANIUM ALUMINIDES

Hydrogen and hydrogenous environments can severely embrittle many intermetallic compounds [15]. In the alpha-2 titanium aluminides, hydride formation is well documented and is linked to reduced ductility at both low and elevated temperatures. On the other hand, studies on gamma and gamma-based titanium aluminides are few. However,

limited experiments have shown that tensile stress-strain and fracture behaviors of both single-phase and two-phase gamma titanium aluminide alloys can be degraded by hydrogen and hydrogenous gases at both ambient and elevated temperatures [2,3,5-8].

1.2.1 Effect of Environment and Temperature on Mechanical Properties

Gamma-based titanium aluminides can range in microstructure from single phase equiaxed gamma to two-phase ($\gamma + \alpha_2$) duplex (equiaxed gamma and lamellar colonies) to fully lamellar [3,16]. The single phase alloys have proven to be extremely brittle, and thus are of little use [8,16]. The two-phase alloys have slightly higher, albeit still poor, ductilities, typically ranging from about 1-3% elongation at room temperature [2,3,16]. Gamma alloys also suffer from low fracture toughnesses, having values under $K_{IC} \approx 16$ MPa$\sqrt{m}$ for duplex alloys [2,3,16]. The fully lamellar gamma alloys have significantly higher fracture toughness (~16 - 36 MPa$\sqrt{m}$) than the duplex, but suffer from lower ductility (~1% at 25°C) and strength [4,16].

Titanium aluminides only gradually lose their strength and stiffness with increasing temperature (due to their ordered structure), but their fracture toughness and ductility show a marked improvement [2-4]. For instance, at high temperatures, gamma alloys have been shown to have ductilities ranging from 10-90% [3,4,6,8].

Several studies have shown that environment can have a degrading effect on TiAl at both ambient and elevated temperatures [2,3,5-8]. At room temperature, the results of environmental testing have been mixed. Liu

and Kim found that, in tensile testing, a duplex gamma alloy had the highest ductility in pure oxygen (1.2%), and the lowest in air (0.2%), with vacuum in between (0.5%) [7]. They also found that the yield strength was independent of environment, while the ultimate strength decreased along with ductility. Takasugi et al. [8] showed similar results on single phase gamma alloys with vacuum ductilities of about 0.5%. In this case, the highest elongations were found to be in vacuum, followed closely by oxygen, then air and hydrogen; the lowest value was about 0.1% for one particular alloy.

Again, yield strengths were unaffected while ultimate strength decreased with the ductility. Nakamura et al. [5] revealed that duplex alloys with high ductilities (3%) in vacuum are significantly affected when tested in air or hydrogen, dropping the elongation down to about 1% for both environments. The fracture strength was also found to be reduced. However, when testing lower ductility alloys (of both duplex and single phase gamma with under 1% elongation in vacuum), the environment proved to have little effect on either elongation or fracture strength. Chan and Kim [4,6] also reported that a near-fully lamellar alloy with under 1% elongation in vacuum was not effected by test environment at 25°C.

In order to explain the differing results of environmental effect at room temperature, Liu and Kim [7] suggested that with low ductility alloys, the environmental effect may be masked by other predominant embrittlement mechanisms. However, Nakamura et al. [5] suggested that embrittlement may require plastic deformation to form fresh surfaces for

reaction, therefore alloys with little ductility will not be greatly affected by the environment.

On the other hand, there is little doubt that TiAl suffers from environmental embrittlement at elevated temperatures. Takasugi et al. [8] reported that the yield strength of a pure gamma alloy was unchanged between vacuum and air for temperatures ranging up to 1000°C, but both ductility and ultimate strength were reduced in air. The greatest reduction occurred at intermediate temperatures (around 400°C). Near-fully lamellar alloys exhibit the same type of behavior: i.e., significant reductions in elongation and ultimate strength in air as opposed to vacuum at 800°C at a strain rate of 10^{-5} /s, as shown by Chan and Kim [4,6].

Chan and Kim [6] claimed to have found no environmental effect on strength and ductility at 800°C in a near-fully lamellar alloy when testing in air and argon at an increased strain rate of 10^{-3} /s. However, their 800°C tests at the lower strain rate of 10^{-5} /s showed that the ductility and ultimate strength of the alloy was significantly greater in vacuum than air, but comparable between air and argon. No results were reported for testing in vacuum at the higher strain rate. Therefore, Chan and Kim's [6] explanation that environmental effect depends on strain rate cannot be supported. Rather, their results suggest that impurities in the argon (reported as 1 wppm O_2, 3 wppm water vapor, and 0.5 wppm hydrocarbons) were responsible for the lack of observed environmental effect, and thus no conclusions can be drawn about the effect of strain rate. This interpretation is also supported by the similarity between specimen fracture surfaces produced in air and argon, and the

significant differences between these surfaces and those produced in vacuum.

In summary, the effects of temperature and environment are as follows:

1) At room temperature, gamma-based titanium aluminides have low ductilities. Environment seems to have a significant effect on the more ductile alloys, while generally having little observable effect on the less ductile alloys. The degrading effects of air (principally from oxygen or water vapor) and hydrogen environments are comparable, with hydrogen sometimes seen as the more damaging of the two gases.
2) At elevated temperatures, γ-TiAl become significantly more ductile and fracture tough. However, the alloys suffer increasingly from environmental embrittlement.

1.2.2 Fractography

At room temperature, the gamma-based titanium aluminides fracture predominately by transgranular cleavage, with limited grain-boundary separation [5,7,8,16,17]. Alloys with lamellar structure also have been found to exhibit both delamination between lamellar plates and some translamellar cracking [5,7,16,17]. Delamination appears to be predominantly along γ/γ interfaces, and occasionally along γ/α_2 interfaces [4,6]. Room temperature fracture surface morphology of pure gamma alloys seems not to be altered by either air or hydrogen, remaining primarily cleavage in all cases [5,8]. Fracture surfaces of duplex alloys,

on the other hand, might have been affected by the environment. Nakamura et al. [5] reported a higher proportion of grain boundary facets on duplex specimens fractured in vacuum than on those fractured in air or hydrogen. For specimens tested in vacuum, microcracks tended to nucleate along grain boundaries, versus transgranular nucleation in air or hydrogen. Liu and Kim [7], however, found little environmental effect on the fracture mode of a duplex alloy showing predominantly transgranular cleavage mixed with some grain boundary separation.

As the temperature increases, the fracture mode switches from primarily transgranular to primarily intergranular above the ductile to brittle transition temperature of 650°C [4,6,18]. Lamellar colony fracture modes remain unchanged, however, showing interface delamination with some translamellar fracture. Chan and Kim [4] found that translamellar fracture is often accompanied by interface delamination. The γ/γ interface again appears to be the predominate location for delamination. One study, however, found limited evidence suggesting a tendency to move from γ/γ to γ/α_2 as the temperature increased from 20 to 800°C [6].

Again, pure gamma alloy fracture morphologies show no apparent effect of environment at elevated temperatures [8]. Lamellar alloy fracture morphologies, on the other hand, may reflect the effect of the test environment. Chan and Kim [4] found that a near-fully lamellar alloy showed a composite-like fracture surface with interface delamination at 800°C in vacuum. However, specimens tested in air showed dimpled fracture surfaces with significantly less delamination.

In summary, the effects of temperature and environment on the fracture morphology of gamma titanium aluminides are as follows:

1) Transgranular cleavage is the primary fracture mechanism at ambient temperature, but the mechanism changes to intergranular separation above the ductile to brittle transition temperature (650°C).
2) Lamellar colonies fail primarily through interface delamination, with some translamellar cracking, at all temperatures.
3) The fracture modes of pure gamma alloys appear to be unaffected by environment at all temperatures, while duplex and lamellar alloys show increased grain boundary separation and less interface delamination, respectively.

1.2.3 Embrittlement Mechanisms

Gamma TiAl apparently suffers from two types of degradation: oxidation and hydrogen embrittlement. Oxidation becomes a significant problem above 800°C, but hydrogen embrittlement can occur over the entire range of ambient to elevated temperatures [2,3,5-8,19].

TiAl is known to have poor oxidation resistance above ~800°C [2,19]. Below 800°C, a protective film of Al_2O_3 forms, but at higher temperatures, TiO_2 crystallization becomes the dominant oxidation process [2,3,19]. A previously formed alumina oxide layer provides little protection since titanium easily diffuses through it. The randomly growing TiO_2 crystals help to create voids at grain boundaries which become nucleation sites for

cracks. These voids also tend to cause the oxide layer to separate from the substrate, resulting in accelerated oxidation. Thermal cycling is known to enhance this peeling of the oxide layer, accelerating the oxidation process even further [2,19].

Hydrogen is known to embrittle both titanium-based materials and intermetallic compounds, thus the hydrogen embrittlement of titanium aluminides can be expected. In Ti_3Al, hydrogen solubility is substantial and hydride formation is well documented which is linked to embrittlement at both ambient and elevated temperatures [2,3]. On the other hand, TiAl has a very low hydrogen solubility, and no hydride formation has been observed over a wide range of temperatures and pressures [2,3,8,9]. Even so, limited tensile studies have shown hydrogen embrittlement of TiAl at ambient and elevated temperatures [7,8].

Hydrogen embrittlement of titanium aluminides can result from exposure to either gaseous hydrogen or water vapor [7,20]. Water vapor can interact with the material and release hydrogen due to the following oxidation reaction:

$$xM + yH_2O \longrightarrow M_xO_y + 2yH$$

where M is a reactive element, in this case either aluminum or titanium [7]. The hydrogen, whether created by the above reaction or from a gaseous environment, then diffuses to the crack tip to cause brittle fracture [7,20].

Hydrogen solubility in duplex alloys is more complex than in the single phase alloys, apparently due to changes in the alpha-2 volume fraction during hydrogen charging [9]. Gao et al. [9] found the peak hydrogen absorption (~1 at%) in a Ti-48Al duplex alloy to be at 550°C. The

overall hydrogen solubility was between 3 to 7 times higher than the single phase gamma alloy, depending on the temperature, and was attributed to the presence of the alpha-2 phase.

The actual hydrogen embrittling mechanism in γ-TiAl is not well understood. Nakamura et al. [5] found a larger volume fraction of cleavage facets and interlamellar delamination markings on fracture surfaces created in hydrogen and air, and thus reasoned that hydrogen may reduce the cleavage and interface fracture strength. Takasugi et al. [8] reported similar results.

One other mechanism which may add to the embrittlement of TiAl at elevated temperatures is sulfur segregation. Soboyejo and Lou [18] performed an in-situ Scanning Auger Multiprobe (SAM) study showing considerable sulfur segregation at the grain boundaries and γ/α_2 interfaces in the $(\gamma + \alpha_2)$ lamellar structure at temperatures above 650°C (i.e., the DBTT). They attributed the transitions from ductile to brittle and from transgranular cleavage to interlamellar and intergranular separation above the DBTT to the reduction in boundary cohesion caused by the segregated sulfur. This mechanism may also explain Chan and Kim's observation [6] of a possible transition from γ/γ to γ/α_2 interface delamination with increasing temperature.

In summary, gamma titanium aluminides are embrittled by the following mechanisms:

1) TiAl is significantly degraded by oxidation above 800°C due to the formation of TiO_2 instead of Al_2O_3.
2) Limited studies have shown a tendency for hydrogen embrittlement in tensile testing, even though the gamma

phase has a significantly lower hydrogen solubility than the alpha-2 phase and does not form hydrides .

3) Sulfur segregation to the grain boundaries and γ/α_2 lamellar interfaces has been shown to occur above 650°C, which determines the transition from ductile to brittle in the material's mechanical behavior.

1.3 OBJECTIVES FOR THIS WORK

Since the intended applications for gamma-based titanium aluminides will subject the material to thermal fatigue in deleterious environments (especially hydrogen and air), it is necessary to evaluate the material's response to these conditions. Previous studies using tension testing at constant temperatures have given a limited understanding of the mechanisms responsible for the material's environmental embrittlement.

Therefore, the purposes of this research are twofold:

1) The assessment of the ability of gamma-based titanium aluminide alloys to resist degradation by thermal cycling in hydrogen and hydrogenous environments.
2) The development of a scientific understanding of the mechanisms for failure under combined thermal cycling and environmental degradation.

CHAPTER TWO

EXPERIMENTAL APPARATUS AND PROCEDURES

A test system and associated procedures were developed to perform environmentally-assisted thermal fatigue with a fixed-grip condition on specimens of γ-titanium aluminide. The test system used direct electrical resistance heating to rapidly heat the specimen and a chilled gas jet to provide swift cooling. During testing, the specimen was enclosed within an environmental chamber to explore the effect of various gaseous environments: namely, hydrogen, helium, and air. Optical and scanning electron microscopy were then used to characterize the thermal fatigue response of the alloy in terms of crack paths, fracture surface morphology, and microstructural changes from the as-received material.

2.1 SPECIMEN

Specimens were designed specifically for thermal fatigue testing to account for special environmental, thermal, and stress considerations. The specimens were then machined from and ingot of material using Electro-Discharge Machining (EDM) and polished to reduce surface defects.

2.1.1 Specimen Design

The thermal fatigue specimens were designed to be thin and flat, with a 1.3 mm thick by 6.3 mm wide by 12.7 mm long gauge length. This geometry provides a high surface area-to-volume ratio to maximize the environmental exposure area for reaction, allows for rapid forced

convective cooling, and ensures a uniform temperature distribution throughout the sample thickness. The specimen also has a sharp, wedge-shaped edge (< 0.025 mm edge tip thickness) on one side to improve rapid cooling from a chilled gas jet. The details of the specimen geometry are shown in Fig. 2.1.

A uniform cross-sectional temperature distribution in the sample is desirable to prevent the development of lateral thermal stresses, thus keeping the material in pure tension loading. The thermal fatigue specimen was designed to satisfy this condition. This can be demonstrated by calculating the non-dimensional Biot number, which is a measure of the resistance to heat convection at a body's surface versus the resistance to heat conduction within the material:

$$Bi = \frac{hL}{k}$$

where h is the convection heat transfer coefficient, L is half the thickness the specimen, and k is the conduction heat transfer coefficient [21]. If the Biot number is much less than one, heat conduction is so rapid compared to the convection that the entire cross section of the body cools at the same rate [21]. The difficulty in the calculation lies in obtaining values for the convection and conduction coefficients. In most situations the value for the convection coefficient h during forced convection (i.e., the cooling phase of the cycle) lies between 25 and 250 W/m^2 K [21]. For a worst case estimate, a value of 500 W/m^2 K is assumed. Likewise, most metals have a conduction coefficient k between 25 and 400 W/m^2 K, so, again for the worst case estimate, 10 W/m^2 K is chosen, since no measured values for k were available [21]. Using these numbers, the Biot number is found to be

0.03, which is two orders of magnitude less than 1. The actual Biot number should be considerably smaller than this "worst case" estimate, and significant thermal stresses should not develop laterally within the thickness of the specimen. It should be noted, however, that a significant temperature gradient is expected to exist near surface of the sample during forced cooling. This gradient will produce higher stresses at the surface than in the interior of the material, thus enhancing the development of surface cracks.

The sample was also designed to resist buckling during compression. Using the Euler buckling equation for columns with fixed end conditions,

$$P_{cr} = \frac{1.2\pi^2 EI}{L^2}$$

where P_{cr} is the critical load, E is the elastic modulus, I is the moment of inertia, and L is the length [22], the specimen is calculated to withstand compressive loads up to 3300 N without buckling. This load generates a stress of 510 MPa, approximately equal to the tensile yield strength at room temperature [3]. The specimen design was verified experimentally, with ability to withstand compressive loads of at least 1000 N without buckling.

2.1.2 Specimen Preparation

Electro-Discharge Machining (EDM) was used to cut the specimens from the cast ingot of material. The wedge was ground on a computerized grinding machine, which placed all of the machining marks in the longitudinal direction to minimize the influence of surface defects. This

also allows for the easier detection of cracks during testing, since cracks will run perpendicular to the loading axis, and thus also to the marks or scratches.

To further minimize the influence of surface defects on crack initiation and growth, the wedge on each specimen was polished with 6 μm diamond paste to a mirror finish. The remainder of the specimen surface was polished using 600-grade silicon-carbide paper, ensuring that all remaining scratches were in the longitudinal direction, reducing the "notch effect". After polishing, each specimen was carefully inspected for defects using an optical stereo microscope at 50X.

2.2 EXPERIMENTAL APPARATUS

The test system was designed to perform thermal fatigue under an essentially fixed-grip condition with an applied preload. The system consists of a test fixture, an environmental chamber, gas supply/exhaust apparatus, and a thermal cycling controller. The tests are monitored using both a chart recorder and a long focal length traveling microscope. Figures 2.2 and 2.3 are the schematics of the test fixture and the test system, respectively. Figure 2.4 is a photograph of the test equipment.

2.2.1 Test Fixture

The test fixture is a rigid box frame which provides sufficient support to the grip arms to ensure an essentially fixed-grip condition. Total motion of the grips out of a fixed-grip condition during thermal cycling is estimated to be under 0.02 mm, producing a strain of less than 0.08%. The grip arm assemblies are fabricated of 25.4 mm diameter brass

rods (to provide good electrical conduction). The grips at the end of the grip arms use a pin to position the specimen and a clamping plate to lock the specimen in place. The grip arms are electrically insulated from the remainder of the test fixture frame. Each grip arm is water cooled by a coil of 6.3 mm diameter copper tubing soldered to its base.

At the base of the lower grip arm is a screw-driven mechanism which allows for the manual application of a preload to the test specimen. At the base of the upper grip arm are both a 6.7 kN (± 0.5% full scale accuracy) load cell and a grip arm alignment mechanism which allows for the upper grip arm to be aligned with the fixed lower one. Figure 2.5 is a detailed assembly drawing of the test fixture and load train.

2.2.2 Environmental Chamber

The environmental chamber has four feed-throughs: two for the grip arms, one for the inlet gas nozzle, and one for the exhaust gas exit and thermocouple. The front of the chamber has a window to allow for visual monitoring of the specimen during testing. The rear wall of the chamber is internally water-cooled. The chamber is supported by a rigid bracket attached to the frame. Access to the grips for specimen installation and removal is obtained by removing the front and side flanges and sliding the chamber and mounting bracket vertically upward or downward along the grip arms and frame. The seal between the chamber and the grip arms is provided by a set of clamped O-rings. The chamber must be electrically insulated from the grip arms, so care was taken to ensure that only the O-ring touches the grip arm. No metal-to-

metal contact between the chamber and grip arms was permitted. Figure 2.6 details the chamber and associated gas lines on the test fixture.

2.2.3 Cooling Gas Apparatus

The cooling gas system supplies chilled gas to rapidly cool the specimen. Up to three gas cylinders provided the high purity gas (99.995% for He, 99.99% for H_2, and air which contained less than 50 ppm water vapor and 19.5 - 23.5% oxygen) for cooling. The gas flow is controlled by a solenoid valve, and the flow rate is set by adjusting the output pressure of the gas cylinders. A coil in the gas line is immersed in a dewar full of either liquid nitrogen (-196°C) or an ethyl alcohol/dry ice mixture (-83°C). Liquid nitrogen is used during hydrogen and helium testing, while the warmer dry ice solution must be used when testing with air to prevent gas condensation with the coil. This cooling produces a gas jet temperature at the nozzle exit of approximately -26°C with hydrogen, -7°C with helium, and 0°C with air.

Before entering the chamber, the gas passes through a 2.3 kPa check valve which prevents back flow out of the chamber during the heating portions of the cycle, i.e., when the solenoid valve is closed. The gas enters the chamber through a nozzle formed of 0.8 mm ID stainless steel tubing aimed at the center of the knife edge and located 0.6 mm away from the edge. When cooling the specimen from 900°C to 25°C in ten seconds, the gas velocity at the nozzle exit was calculated to be 56 m/sec with air, 45 m/sec with helium, and 30 m/sec with hydrogen.

The 32 mm exhaust line exits the chamber opposite the inlet nozzle. The gas must pass through a 6.9 kPa check valve, again to prevent back

flow into the chamber. The exhaust line vents into a fume hood rated for hydrogen use. Another 2.3 kPa check valve is located at the end of the exhaust line as a hydrogen safety precaution to prevent air from entering the exhaust line. This combination of check valves maintains the chamber pressure at 9 kPa above the barometric pressure.

Safety during testing with hydrogen gas is an important issue. The inflammability range of hydrogen in air by volume is 4.0% to 74.2% [23]. Several precautions are taken to ensure that air cannot enter the system to cause an explosion hazard:

1) The entire gas system is flushed with argon at least 500 times its volume prior to hydrogen introduction.
2) All of the fittings are leak tested both during the argon flush and also during the initial hydrogen introduction.
3) The entire test system is maintained under a positive pressure.
4) Check valves prevent air from back flowing into the system.

The above steps ensure that air cannot enter the system to create an explosion hazard. Note that even if a leak allowed air into the system, it would take a tremendous 25% by volume of air to enter and mix with the hydrogen to cause a safety problem.

Obviously, a build-up of 4% by volume of hydrogen leaking out of the system into the lab poses a greater risk than air leaking in. However, careful leak testing minimizes any possible H_2 leaks, and furthermore, adequate room ventilation will quickly dissipate any escaped hydrogen. The high flow rate of the hood (20.0 m^3/min) compared to the relatively small flow of exhaust hydrogen (<0.03 m^3/min for ten seconds at thirty

second intervals) quickly diffuses the exhaust gas to well below the 4% explosive limit as it is released to the atmosphere.

2.2.4 Thermal Cycling Controller

The thermal cycling controller utilizes three electronic programmable timers to control the timing of the three phases of the thermal cycle: heating, holding at temperature, and cooling.

The rapid heating of the test specimen is achieved by direct electrical resistance heating, i.e., by passing a high electrical current through the specimen. Current is delivered to the specimen via the grip arm/grip assemblies. A manually-set VARIAC variable transformer is used to adjust the voltage (0 to 4.91 V) across the specimen which provides the proper amount of current to achieve the desired temperature profile in the heating phase of the cycle. Thus the heating profile can be adjusted by varying the current and/or the timer setting. At 900°C, the current is nominally 240 A at 1.2 V, producing 290 W. A second VARIAC transformer (0 to 4.91 V) controls the specimen temperature during the holding phase of the cycle.

During the cooling phase, the electrical current is cut off, and the third timer opens the solenoid valve in the gas line, allowing the cooling gas to flow. The cooling profile can be adjusted by varying the gas flow rate, the gas temperature (via the cooling bath), and/or the timer setting.

A Sola Electric constant voltage transformer feeds the thermal cycling controller with a constant 120 V AC ± 3% for a 15% line voltage fluctuation. This permits excellent repeatability (to within ±0.5°C) between adjacent heating cycles.

2.2.5 Data Acquisition

A two-pen chart recorder records the output from both the load cell and the thermocouple for the duration of the test. During typical testing, the chart speed was set at 5 mm/min. Speeds of 150 and 300 mm/min were used to characterize the heating and cooling profiles. The thermocouple output was recorded at the 50 mV range, and the load cell output was recorded at the 5 V range. The load cell is a T-Hydonics 6.7 kN (± 0.5% full scale accuracy) model TC-5. A K-type thermocouple is spot welded to the center of the edge of the specimen directly opposite the wedge, Fig. 2.2. The thermocouple has an accuracy of ±2.2°C or 0.75%, whichever is greater. A long-focal length traveling microscope is used for visual inspection of the specimen at 20X during the test to monitor the development of fatigue cracks. The cycles are counted on an electromechanical rotary type counter connected to the controller.

2.2.6 Thermal Profiles

A proof test was conducted to determine the thermal profile of the specimen during the heating, holding, and cooling phases of the cycle. The temperature profile along the specimen's gauge length was not uniform since it was heated by internal resistance and the grips were cooled. Figure 2.7 shows the thermal profile along the gauge length of the specimen at both maximum and minimum temperatures for four temperature ranges. See Appendix B for a detailed description of the proof test and further results, including heating and cooling rates.

2.3 TEST PROCEDURES

Since environmental thermal fatigue testing is not a "conventional" test, the test procedures needed to be evolved along with the development of the test apparatus. These procedures were designed to ensure accuracy of the data and consistency between tests.

The procedures consist of primarily five steps: test specimen preparation, specimen mounting within the environmental chamber, test initiation, monitoring the specimen and test conditions, and test termination. See Appendix A for a detailed test procedure.

2.3.1 Specimen Cleaning and Thermocouple Attachment

Although each specimen's location in the original ingot is known, the specimens were randomized for testing to avoid subjectively choosing specimens for the tests. As described earlier, each specimen was polished and carefully inspected at 50X with an optical microscope. Prior to mounting in the test fixture, each specimen was ultrasonically cleaned in acetone and then methanol for 15 minutes each. From this point on, the specimen was handled only with rubber gloves. A K-type thermocouple was formed by twisting 0.381 mm diameter chromel and alumel wires together. It was then spot welded to the edge of the specimen using a Unitek spot welder. The two thermocouple wires were then fed through the exhaust flange of the chamber. To prevent contact between the two wires while within the chamber and exhaust pipe, they were encased in a ceramic sheath near the specimen, and a Teflon sheath at a further distance. A Teflon bushing in a swage-lok fitting was used to seal the thermocouple exit port.

2.3.2 Mounting the Specimen

Prior to mounting the specimen and closing the chamber, all chamber flanges were cleaned with acetone. The specimen was then carefully moved into the chamber and placed in the grip slots. Care was taken to ensure that the upper grip arm and grip were perfectly aligned with the specimen. Once the specimen was locked in place, the chamber was sealed.

At this point a Digital Volt Meter (DVM) was utilized to test for electrical continuity between the chamber and the grip arms. If continuity existed, the chamber mounts were adjusted to tilt the chamber slightly in order to bring it parallel to the grip arms. Once continuity was eliminated, the chamber mounts and O-ring seals were tightened, locking the chamber in place.

2.3.3 Test Initiation

First, the system was flushed with the test gas long enough so that over 500 system volumes of gas had flowed through it. When testing with hydrogen, argon was used for the initial flush to remove the air from the system prior to flushing with hydrogen. The cooling coil then was inserted into the cooling bath, and the gas was flushed through once again.

Now that the system was ready to begin testing, the cooling water was turned on and the preload manually applied. The load cell signal amplifier output was monitored with a DVM as well as the chart recorder.

Upon activation of the controller, the thermal cycling began and the maximum and minimum temperatures were adjusted to the required levels. During the first twenty cycles as the grip arms heated up to a "steady-state" temperature, the load was also readjusted upwards to account for the expansion of the grip arms. By the twentieth cycle, the vast majority of this thermal expansion was completed, and the load was not adjusted for the remainder of the test in order to maintain a fixed-grip condition. The temperature (either maximum or minimum) was adjusted whenever it drifted out of a range of ±10°C for the duration of the test.

2.3.4 Test Monitoring

The chart recorder registered the output from both the thermocouple and the load cell for the entire test, enabling any deviations to be detected. The specimen was periodically examined using the long-focal length traveling microscope to detect fatigue cracks and surface damage. However, only those cracks that were on the window-side of the specimen and not covered by oxidation could be detected.

2.3.5 Test Termination

The thermal fatigue test was terminated for one of two reasons: fracture of the specimen or the attainment of a predetermined number of cycles. Upon the completion of the test, the load was immediately released (if the specimen was not fractured), otherwise the cooling of the grip arms would increase the load well beyond the preload level. The specimen was then carefully removed after cool-down (see Appendix A) from the chamber for later analysis.

2.4 MICROSTRUCTURAL AND FRACTOGRAPHIC EXAMINATION

All of the tested specimens were examined with a stereo optical microscope at 50x to locate any fatigue cracks or surface damage. Selected specimens were then examined with a polarized illumination optical microscope, and a scanning electron microscope (SEM).

2.4.1 Optical Observations

A Wild Heerbrugg stereo microscope at 50X was used for the initial post-test survey of each specimen after testing to roughly determine the extent of thermal fatigue and environmental damage. A Zeiss Axiomat optical microscope, operated at bright field and polarized illumination modes, was used to characterize both the microstructure of the alloy and the crack paths in relation to the microstructure.

2.4.2 SEM Observations

An ETEC Autoscan scanning electron microscope (SEM), operated at both secondary electron scanning and back-scattered electron imaging modes at 20 kV and a working distance of 19 to 25 mm, was used to obtain more detailed information on the relationship between crack paths and microstructure, and to identify the features of fracture surface morphology. SEM analyses of mating surfaces from broken halves of selected specimens were performed to further study the micromechanisms for cracking.

CHAPTER THREE

RESULTS

A Ti-48Al-2Cr alloy was used to examine the combined effect of deleterious gaseous environments and thermal fatigue on gamma-based titanium aluminides. The material was thermally cycled from room temperature either 550, 750 or 900°C. Sample lifetimes varied greatly between environments; at 900°C, no failures were observed in helium, while two-thirds of the specimens tested in air failed after several thousand cycles, and all specimens tested in hydrogen failed within thirty cycles. At lower cycling temperatures, failures were only observed in hydrogen. Cracking and fractographic features showed significant differences between environments.

3.1 MATERIAL

A two-phase gamma titanium aluminide with the nominal composition of Ti-48Al-2Cr (at. %) was used in this study. The material was supplied by Motoren- und- Turbinen- Union of Germany in the form of a hot-isostatically-pressed (HIP-ed) 25 x 50 x 75 mm ingot with a two-zone casting microstructure, namely, a thin layer of chill zone and a well-developed columnar zone (Fig. 3.1). The alloy had a deformed duplex ($\alpha_2 + \gamma$) microstructure consisting of regions of ($\alpha_2 + \gamma$) lamellar structure along with equiaxed gamma grains. Grain sizes ranged from 50 to 300 μm. Figure 3.2 illustrates the typical grain structures in the columnar zone,

showing deformed ($\alpha_2 + \gamma$) lamellar structure and equiaxed gamma grains.

The specimens were oriented in the longitudinal direction of the ingot with their surfaces perpendicular to the ingot surface, Fig. 3.3. With this orientation, the specimen gauge length has a microstructure as shown in Fig. 3.2. Figure 3.4 demonstrates that the loading axis of the gauge length is always perpendicular to the columnar zone.

3.2 TEST PARAMETERS

Thermal cycling tests were conducted in three environments (helium, hydrogen, and air) and with several temperature ranges. The period of each cycle was 30 seconds, with the heating phase, high temperature holding phase, and cooling phase being 10 seconds each in duration. The minimum temperature of each test was 25 ± 10°C, while the maximum temperature was either 900°C or 750°C, with one test at 550°C (± 10°C). Typical temperature cycling profiles and rates are shown along with a complete discussion of the thermal proof test in Appendix B. A preload of 1.57 ± 0.02 kN (corresponding to 50% of the alloy's room temperature yield strength [3]) was applied to each specimen. Note that the temperature and load cycles are out-of-phase, i.e., the maximum load occurs at the minimum temperature, and vice-versa, Fig. 3.5. The combination of the temperature and preload parameters dictates the cyclic thermal loading conditions. Table 1 details all of the testing parameters.

3.3 LIFE TO FAILURE AND GENERAL FEATURES

The lifetimes to failure and general features of failure varied greatly between the three environments tested. Table 2 details the lifetime results for all tests. No samples tested in helium, the inert environment, experienced fracture at any temperature. Specimens cycled in air up to 900°C had failure times ranging from approximately 2,000 to above 6,000 cycles, while no failures were observed in air at 750°C. Samples tested in hydrogen at 900°C all failed in under 30 cycles. At 750°C, samples tested in hydrogen had two distinct lifetimes: under 50 cycles and above 1,800 cycles. A single test was conducted in hydrogen by cycling to 550°C without failure. Figures 3.6 - 3.8 show the specimen morphologies after testing in each environment at 900°C, 750°C, and 500°C, respectively. Cracking in each environment generally exhibited different features.

3.3.1 Helium

No failures were observed for samples tested to over 4,100 cycles in helium at either 900°C or 750°C, Table 2. One specimen was tested up to 6,467 cycles at 900°C, again with no failure. A few surface cracks were seen on these specimens after the test. For example, one specimen (tested at 900°C for 4,100 cycles) showed one small surface crack (approximately 1 mm long) perpendicular to the loading direction and several finer cracks (about 100 μm long), Fig. 3.9. These cracks moved from grain to grain without any appreciable changes in direction, as seen in Fig. 3.9b. Thus the cracking in helium appeared to be unrelated to the microstructure, i.e., cracking was purely mechanical in nature.

3.3.2 Air

Failures in air at 900°C were observed to occur over a wide range of test times, ranging from fracture at 2,106 cycles to no failure after 6,330 cycles, Table 2. Fracture was brittle with flat surfaces perpendicular to the loading direction and almost no plastic deformation Fig. 3.6. These failed specimens showed a few surface cracks aside from the main crack, Fig. 3.10.

Figure 3.6 and 3.11 show a thick oxide layer which formed on specimens which were cycled to 900°C. This yellowish oxide layer was observed to locally buckle and flake off of the surface, exposing fresh surfaces below. These fresh surfaces were generally rough in appearance. By the end of the test, many specimens had the once-straight knife edge eroded away into a slightly concave shape. This erosion was not seen in other environments. Higher magnification views of this oxide, Fig. 3.12, reveal its rough and irregular crystallographic appearance.

No samples tested in air to 750°C failed during tests of up to 6,500 cycles, Table 2. Oxidation of these specimens was not as intense as those cycled to 900°C, and no flaking of the oxide layer was observed, Fig. 3.7. The oxide layer was dark blue or gray in appearance, and seem to be more firmly adhered to the surface than the yellow oxide seen at 900°C.

The difference in the oxidation between 750 and 900°C appears to reflect the different types of oxide formed at these two temperatures, namely Al_2O_3 and TiO_2, respectively.

3.3.3 Hydrogen

The results obtained from testing in hydrogen were significantly different from those in helium or air. At 900°C, none of the five specimens tested survived beyond 30 cycles, Table 2. One specimen lasted only for three cycles. Failure by thermal cycling in hydrogen was brittle, with flat fracture surfaces perpendicular to the loading axis and the near absence of plastic deformation, Fig. 3.6. Further examination revealed extensive cracking aside from the main crack; zig-zag surface cracks with many branches were seen over the entire gauge length, Fig. 3.13. These cracks tended to be strongly influenced by the microstructure, i.e., they often changed direction or formed branches, especially when traversing grain boundaries. Also, some grains at the specimen surface had actually fallen off, Fig. 3.14. This extensive damage, not seen on specimens cycled in other environments, indicates a strong attack on the material by hydrogen.

Three distinct crack paths were identified, as shown in Fig. 3.15. These were (1) delamination along the α_2/γ interfaces in the lamellar structure, with some translamellar cracking (i.e., transverse to the lamellar plates), (2) cleavage cracking through the γ grains along what appear to be certain crystallographic planes, and (3) grain boundary separation between γ grains, γ grains and lamellar patches, and adjacent lamellar patches. This preference for certain microstructural features was responsible for the zig-zag shaped crack paths on a microscopic scale. Thus these microstructural sites seem to be the primary hydrogen embrittlement locations.

At the lower temperature of 750°C, two specimens failed at 36 and 46 cycles, respectively, while a third did not fail until 1,828 cycles, and the remaining three specimens survived through test termination, Table 2. As at 900°C, multiple surface cracks were seen to develop and grow on these specimens during the first 30 cycles of testing, but this crack growth slowed and nearly stopped by the 40^{th} or 50^{th} cycle. At this point, a thin oxide layer visible to the unaided eye had formed on the surface. Examination of these cracks following the tests on both the short and long lifetime specimens revealed the same zig-zag cracking pattern as seen at 900°C. Figure 3.16 shows the specimen that fractured after 46 cycles, revealing a light oxide layer on the surface. Extensive secondary cracking aside from the main crack and substantial surface attack (i.e., grain removal) are visible in Figs. 3.17 and 3.18. Although the specimen which survived for 1828 cycles before fracture has considerable more oxidation on the surface, Fig. 3.19, similar surface cracks aside from the main crack are visible, Fig. 3.20. Figure 3.21 is the surface morphology of a specimen after cycling for 200 cycles without fracture, again showing evidence of cracking and surface grain removal like that seen at 900°C. The oxide layer is also visible as the web-like feature across the entire surface. However, the cracks on all of these specimens were, on average, much shallower than the cracks formed during the 900°C tests. In fact, light polishing to remove the oxide also removed most of these cracks. These results suggest a competition mechanism, with a strong hydrogen attack during the early cycles, which is eventually greatly reduced by the onset of oxidation (see section 4.3.2).

A single specimen was cycled in hydrogen to 550°C for 3,000 cycles with no failure. Again, many fine surface cracks and evidence of removed surface grains due to hydrogen attack were visible, Fig. 3.22.

3.4 FRACTOGRAPHY

The fracture surface morphologies produced in air and hydrogen follow the same patterns as the fracture paths. Since none of the specimens tested in helium failed, no fractographic data for that environment is available.

3.4.1 Air

The fracture surfaces produced in air with cycling to 900°C show a typical three zone feature: nucleation, fatigue propagation, and rapid fracture. Figures 3.23 and 3.24 are an optical micrograph of the mating fracture surfaces of a specimen whose lifetime was 2,782 cycles, and its associated sketch of the three-zone structure, respectively. The fatigue propagation zone is clearly visible in these images as a flat, oxidized semi-circular region, with very few microstructural features. The propagation fracture surface covers about 20% of the cross-section. Figure 3.25 shows mating surfaces in the nucleation and propagation zones. Figure 3.26 is an enlarged portion of one of those zones. Again, note how the surfaces are nearly featureless (as compared to the oxidized fracture surface formed in H_2 at 750°C, see section 3.4.2) except for the oxide layer accumulated there as the crack propagated and fresh surfaces became available. All specimens fractured after thermal cycling in air had a similar appearance.

Since no specimens failed when cycled to 750°C in air, no fracture surface data were available.

3.4.2 Hydrogen

Fracture surfaces produced in hydrogen at 900°C were significantly different from those produced in air. As the SEM image of mating fractures in Fig. 3.27 shows, there were no apparent three-zone features, i.e., nucleation, propagation, and rapid fracture zones; the fracture features were basically identical over the entire surface. Also, the fracture surface generally followed the same features as the surface cracks, that is, interlamellar delamination with translamellar cracking, cleavage, and grain boundary separation, Fig. 3.28.

Two types of fracture surfaces were developed when cycling in hydrogen to 750°C: (1) Those specimens which fractured in under 50 cycles had the same features as those produced in hydrogen at 900°C — very brittle features across the entire surface with no clear nucleation/propagation zones, Fig. 3.29, and (2) the specimen which fractured after a longer period of time (1,828 cycles) showed some features similar to those produced in air at 900°C; namely, there was a distinct propagation region like those seen in air. Figure 3.30 is an optical image of the mating fracture surfaces. The propagation region was not as large as those produced in air, covering only about 12% of the surface (as opposed to 20% for a surface produced in air). The propagation zone also showed more features than the corresponding surfaces produced in air, although it was still fairly flat. Figure 3.31 is region in the nucleation/propagation zone, showing signs of flat cleavage and

translamellar fracture, along with some oxidation of the nucleation and propagation surfaces.

3.5 SUMMARY

The primary results of the thermal fatigue testing are as follows:

1) Thermal fatigue testing was performed on a Ti-48Al-2Cr HIP-ed alloy. A 50% of yield strength pre-stress was applied,, and the specimens were thermally cycled from room temperature to various high temperatures, with a 30 second cycle of heating, holding, and cooling, with each phase being 10 seconds in duration.
2) No failures were observed in a helium environment. Surface cracks which formed were primarily normal to the loading direction and unrelated to the microstructure.
3) Specimens cycled in air to 900°C had thermal fatigue lives as low as 2,000 cycles, while no failures were observed at 750°C. Cracks propagated in a flat, cleavage-type manner, with a clear nucleation, propagation, and rapid fracture zones.
4) No specimen survived beyond 30 cycles in hydrogen at 900°C. Many surface cracks developed over the entire specimen, following three main microstructurally-related paths. The fracture surface had no evidence of crack propagation.
5) At lower cycling temperatures, hydrogen also appeared to strongly attack the specimen in the initial cycles, but the attack was greatly slowed by the onset of visible oxidation. Lifetimes at 750°C were mixed, being either below 50 cycles or above 1,800 cycles.

CHAPTER FOUR

DISCUSSION

The results presented in the previous chapter indicate that hydrogen strongly attacks and embrittles the material (an effect that was not observed in previous conventional tensile tests), while air tends to simply accelerate the thermal fatigue degradation by oxidation. These results suggest important mechanisms for hydrogen enhanced cracking which operate during thermal fatigue in gaseous environments. In the following subsections, the understanding of the results are discussed.

4.1 THERMAL FATIGUE IN HELIUM

Since no specimens failed during thermal fatigue in helium, it serves as a good reference for comparison to other environments. Also, the inert nature of helium reveals material damage which is purely thermal-mechanical in nature. Results from tests in helium suggest that thermal fatigue primarily manifests its degradation on the material through the formation of surface cracks, which are generally normal to the loading direction. These surface cracks are probably generated by high thermal gradients at the surface of the material. Surface defects, such as scratches, tool marks, and inclusions are stress concentrations and serve as the nucleation sites for cracking. As soon as the surface cracks form, they begin to propagate both along the surface and into the material. Compared to the other environments, crack propagation in helium appears to be rather slow considering that although several

surface cracks were observed, none had grown fast enough to fracture the specimen within the test time.

The tendency for the majority of the surface cracks to form on the thick portion of the gauge length rather than the knife edge (in all environments, not just helium) may be explained as follows: although the temperature of the cross section is uniform during the holding portion of the cycle, there exists a high thermal gradient (see section 2.1.1) during rapid cooling, with the maximum tension at the surface. However, since the wedge is thinner than the body of the specimen, the wedge's surface thermal gradient, and thus the surface stress, is less as well.

4.2 OXIDATION-INDUCED FAILURE

The results from the thermal fatigue testing an air suggest that oxidation primarily accelerates the actions of thermal fatigue-produced cracking, at least at high cycling temperatures (i.e., 900°C). A second effect observed in air when cycling to 900°C is the degradation of the specimen surface underneath the oxide. This degradation also undoubtedly accelerates failure. Since no specimens failed when cycling to 750°C, it is difficult to determine the full effect of air on the lifetime at these lower temperatures.

4.2.1 Cycling from 25 to 900°C

When cycling to 900°C in air, two-thirds of the specimens failed within the test period, Table 2. This suggests that oxidation when cycling to 900°C accelerates the material degradation and crack propagation. As in the helium environment, cracks developed while cycling in air were

normal to the loading direction and were relatively unaffected by the microstructure. The typical three-zone fracture surfaces (nucleation, fatigue crack propagation, and overload fracture), showing the main crack propagating through the material perpendicular to the loading axis, support this interpretation, Figs. 3.23 and 3.24.

Thermal fatigue-induced surface cracks in air also nucleate at stress concentrations produced by defects or inclusions in the material, and are likely aided by the oxygen attack. The wide scatter in the lifetimes in air, Table 2, suggest that this is the case. Since crack propagation rate under the same conditions (e.g., cycling to 900°C in air) should be similar, the majority of the lifetime is most likely spent in the gradual degrading of the material and the nucleation of cracks [14]. Thus if nucleation is strongly dependent on the material surface defects, then a large spread in lifetimes is to be expected.

Although several cracks were formed during thermal fatigue in helium at 900°C, none of the samples fractured during testing. However, two-thirds of the specimens cycled in air fractured. This suggests that, in addition to accelerating crack nucleation, oxygen also accelerated crack propagation.

Even though the detailed mechanism for oxygen enhanced crack nucleation and growth is not clear, the formation of titanium oxide (TiO_2) when cycling to 900°C undoubtedly contributes to crack nucleation and propagation. As stated earlier, the unprotective TiO_2 oxide forms on the surface of TiAl more readily than the protective aluminum oxide (Al_2O_3) above 800°C [2,19]. The evidence of the formation of TiO_2 oxide and its effect on the material were clear. A heavy layer of the yellowish oxide

would build up and eventually flake off, exposing rough fresh surfaces underneath for further oxidation. The random growth pattern of TiO_2 oxide with many voids can be clearly seen in Fig. 3.12, and compares well with the TiO_2 shown by Umakoshi [19]. This persistent attack obviously assists in crack nucleation.

TiO_2 oxidation also attacks the crack tip during the heating cycles. Thus it can be expected that the material at the tip is degraded similarly to the surface, resulting in an oxidation-enhanced propagation of the crack.

4.2.2 Cycling from 25 to 750°C

Since none of the specimens tested to 750°C in air failed within the test period, Table 2, the effect of air at 750°C on the lifetime could not be determined. As compared with those tested at 900°C, there is no severe surface degradation observed at this lower cycling temperature. The absence of surface damage is attributed to the formation of Al_2O_3 at 750°C, which is a dense and protective surface oxide, i.e., once formed, it prevents further oxidation. Therefore, when cycling to 750°C, a significant reduction in lifetime is not expected between air and an inert environment

.

4.3 HYDROGEN-INDUCED FAILURE

This study has clearly shown that γ-Ti-48Al-2Cr can be severely damaged by hydrogen during thermal cycling, resulting in rapid and catastrophic failure. This catastrophic failure at a stress level of 241 MPa (50% of the room temperature yield strength of the alloy) was not seen in conventional tensile and other tests where the influence of hydrogen was

limited to a loss in an already low ductility. The loss was often comparable in magnitude to that experienced in air. Extensive embrittlement and cracking were not encountered [2,3,5-8]. Apparently, only the combined actions of thermal fatigue and a gaseous hydrogen environment produce the observed effect.

4.3.1 Hydrogen Attack During Cycling from 25 to 900°C

The details for hydrogen attack and associated hydrogen-induced catastrophic failure are unclear; however, a number of sequential processes may be involved in the reaction of hydrogen with the material [20]. The principle processes are: (1) dissociative chemical adsorption of hydrogen from molecular to atomic form at the specimen or crack surface, (2) hydrogen entry and diffusion to the microstructurally related fracture sites, and (3) hydrogen-material interaction leading to embrittlement at the fracture sites. The kinetics of hydrogen induced cracking is governed by the slowest process in this sequence in conjunction with the mechanical driving force and thermal condition [20]. The very rapid failure in hydrogen when cycled to 900°C suggests an accelerated entry of hydrogen into the material resulting from either the breakdown of surface oxide barriers or the production of fresh surfaces, both of which can be caused by thermal fatigue [2,11,14]. Failure results from the rapid growth of numerous cracks across the entire surface of the material, some of which may then link together to precipitate rapid fracture. Identification of the rate-controlling process requires well coordinated chemical, mechanical, and metallurgical studies, and is beyond the scope of this study [20].

The mechanism for the hydrogen embrittlement process is also not fully understood. Two mechanisms may be considered: (1) formation of hydrides and (2) decohesion or reduction of bond strength by hydrogen. Thus far, most studies have suggested reduction of bond strength by hydrogen as the mechanism for hydrogen embrittlement of gamma and gamma-based TiAl alloys since no hydride formation has been observed over a wide range of temperatures and pressures [2,3,8,9,15]. The evidence produced in this study appears to support this mechanism because the hydrogen-induced cracking followed specific microstructural paths, i.e., cleavage planes, grain boundaries, and α_2/γ lamellar interfaces, which are not related to the habit planes of hydrides in α_2 and γ phases [24,25]. The rapid heating and cooling of the thermal fatigue cycling may enhance the weakening and eventual rupturing of these bonds, thus accelerating the embrittlement process.

4.3.2 Hydrogen Attack During Cycling from 25 to 750°C

At lower cycling temperatures, the production of surface cracks and pits during the initial cycles reveals that the hydrogen attack is substantial at these temperatures also. This suggests that the same hydrogen attack mechanisms operating at 900 °C are also at work at lower temperatures. Those specimens (the two fractured specimens out of the six tested) which fractured within 50 cycles showed the same fracture features as those which failed at 900°C. However, their lifetime was slightly longer, which probably reflects the influence of temperature on hydrogen attack.

Although the same types of cracking patterns and removal of grains from the surface observed at 900°C also were seen at both 750 and 550°C in the other specimens (the four unfractured specimens out of the six tested), Figs. 3.21 and 3.22, respectively, the growth of these cracks was retarded or completely halted with the development of a visible oxide layer. Careful examination of the specimens (both as tested and after a slight polish) showed that most cracks on the surface were shallow and not well developed. Their depths appear to have been only a few microns, since most of the cracks were removed by light polishing.

The oxidation which appeared on the specimens by the 40^{th} or 50^{th} cycle indicates that the system was contaminated with oxygen. The source of the oxygen may be either the impurity gas within the hydrogen source itself or residual impurities (oxygen and water vapor) retained in the environmental chamber. The formation of this oxide was apparently responsible for halting further hydrogen attack. Figure 3.21 shows cracking and surface hydrogen attack on a specimen tested for 200 cycles at 750°C in hydrogen and also shows the Al_2O_3 oxide layer as the web-like pattern on the surface.

Therefore, there appears to be two processes, hydrogen attack and oxidation, operating in parallel and competing with one another. The details of this competition are considered in the following section.

4.3.3 Competing Processes: Hydrogen Attack vs. Oxidation

The observations from testing at temperatures below 800°C suggest a competition between hydrogen attack and surface oxidation. The hydrogen generates numerous cracks and assists their growth by

attacking and embrittling specific microstructural sites. At the same time, oxygen begins forming an oxide layer on the surface. Whether or not the specimen fails quickly depends upon which process dominates; that, in turn, depends upon the temperature and the residual oxygen level.

At temperatures above 800°C, the oxide which forms on the surface, TiO_2, is very porous and does not block the hydrogen from entering and reacting with the material. Thus rapid material failure is expected.

However, at temperatures below 800°C, the impurity oxygen begins forming a protective layer of Al_2O_3 on the surface, which effectively blocks the hydrogen from reacting with the material. Also, at these lower temperatures, the hydrogen adsorption and diffusion rates can be expected to be slower. Therefore, at temperatures below 800°C, the partial pressure of oxygen will determine which process, hydrogen attack or oxidation, will succeed.

If the partial pressure of oxygen is too low, the oxidation of the surface will not be complete in time to obstruct the hydrogen attack and prevent hydrogen-induced failure. However, if the partial pressure of oxygen is high enough, the oxide will succeed in covering the surface adsorption sites quickly, preventing further hydrogen attack and dramatically increasing the material's thermal fatigue life span. Therefore, the widely varying lifetime results obtained during the 750°C testing in hydrogen can be explained by slightly different partial pressures of impurity oxygen in the system during each test. The actual partial pressure of oxygen required to form a protective oxide on the surface quickly enough to prevent hydrogen-induced failure has not be

determined yet, but it is expected to be relatively low for gamma-based titanium aluminides [26]. Further work is needed to clarify this issue.

As evidenced by the single specimen which fractured at 1,828 cycles, cracks which have been formed by the initial hydrogen attack may then continue to propagate in a manner similar to those cracks produced in air, resulting in a three-zone fracture surface (nucleation, propagation, and rapid fracture). These zones, however, were not as distinct as those produced in air, and the propagation zone was considerably smaller, Fig. 3.30. The propagation surface of the crack, Fig. 3.31, appeared to be a mixture of fracture features; although primarily flat like the propagation surface produced in air, it had more visible rough or brittle features. Some oxidation was also evident. This indicates that a combination of hydrogen embrittlement and oxidation-induced failure were operating during crack propagation.

4.4 IMPLICATIONS

Hydrogen attack on γ-titanium aluminide has been shown to be tremendously enhanced by thermal cycling. No other constant-temperature test in a hydrogen atmosphere revealed any effect greater than a limited loss in the material's ductility. Therefore, environmental thermal fatigue testing is a critical tool for the assessment of titanium aluminides for use in high temperature applications.

Not only has thermal fatigue testing revealed the strong hydrogen attack, but it also suggests ways to prevent it. Since hydrogen has been identified to attack specific microstructural sites, work could be

performed to create an alloy more resistant to hydrogen attack. Also, it has been shown that dosing the hydrogen with some level of impurity oxygen can be used to protect the material, although this is limited to operating temperatures below 800°C. Further study is required to clarify this issue.

CHAPTER FIVE

SUMMARY AND FUTURE WORK

5.1 SUMMARY

1) A test system and associated procedures were developed to conduct studies on the combined effects of thermal fatigue and gaseous environments on a gamma-titanium aluminide alloy, with the goals of assessing the alloy's resistance to environmentally enhanced thermal fatigue, and developing a mechanistic understanding of the processes involved.
2) Thermal fatigue testing was performed on a Ti-48Al-2Cr HIP-ed alloy. A pre-stress of 241 MPa (50% of the room temperature yield strength) was applied, and the specimens were thermally cycled from room temperature to 900, 750, and 500°C, respectively, with a 30 second cycle composed of 10 second segments of heating, holding, and cooling.
3) No specimens failed while cycling in helium for over 4,000 cycles. Some surface cracks developed which were primarily normal to the loading direction. Cracking in helium appears not to be strongly related to the microstructure. This indicates that thermal fatigue primarily degrades the material through the formation of surface cracks.
4) Specimens thermally cycled in air to 900°C failed as soon as 2,100 cycles, while others did not fail after 6,300 cycles. Significant surface oxidation (TiO_2) and erosion were observed. Fracture surfaces had distinct nucleation, propagation, and rapid fracture zones. The

propagation zone consisted of flat cleavage fracture. The results suggest that air tends to accelerate thermal fatigue-induced degradation through oxidation, at least at high cycling temperatures (900°C).

5) No specimens cycled in air to 750°C failed in tests up to 6,500 cycles. Oxidation was significantly less severe than at 900°C, and composed primarily of Al_2O_3. No surface erosion was evident.

6) Hydrogen strongly attacked and severely embrittled the alloy when thermally cycled from 25 to 900°C, producing catastrophic failure in less than 30 cycles. Failure resulted from the development of multiple surface cracks. This strong attack was not observed in tensile tests.

7) Hydrogen attack was also evident at the lower cycling temperatures of 750 and 550°C, but was in competition with residual oxygen. In the early cycles, hydrogen attacked the material, producing cracks and pits, while oxygen attempted to cover the surface with a protective Al_2O_3 oxide. Lifetime appears to be a strong function of temperature and the partial pressure of oxygen at temperatures below 800°C.

8) Hydrogen induced cracking tended to follow specific features of the microstructure. Alpha-2/gamma interfaces (in the lamellar structure), cleavage planes, and grain boundaries are the preferred cracking sites in hydrogen.

9) Thermal fatigue testing in gaseous environments appears to be a critical tool for evaluating γ-titanium aluminide for use in engineering applications in deleterious environments at high temperatures.

5.2 FUTURE WORK

Much work needs to be performed to increase the understanding of the kinetics and mechanisms of environmentally enhanced thermal fatigue. Longer test times could be used to gain an increased quantification of the magnitude of the environmental effects which accelerate failure, since no specimens tested in the reference environment failed. Also, to verify the competition mechanism suggested for hydrogen at lower cycling temperatures, tests using an ultra-pure hydrogen system should be performed to eliminate the retarding effect of oxidation. Carefully controlled oxygen partial pressures could be used to quantify the critical oxygen level to prevent hydrogen attack.

To gain further insight into the mechanisms that create the massive degradation due to the combined effects of hydrogen and thermal fatigue, the effect of heating and cooling rate needs to be investigated. Also, thermal-mechanical effects could be examined by actively adjusting the phase of the load cycle so that it is no longer 180° out-of-phase with the temperature cycle. This type of testing would enable the evaluation of the effect of load at various portions of the cycle.

	25 to 550 °C	25 to 750 °C	25 to 900 °C
Temperature Upper Limit	550 ± 10 °C	750 ± 10 °C	900 ± 10 °C
Temperature Lower Limit	25 ± 10 °C	25 ± 10 °C	25 ± 10 °C
Heating	10 s from 25 to 550 °C	10 s from 25 to 750 °C	10 s from 25 to 900 °C
Holding	10 s at 550 ± 10 °C	10 s at 750 ± 10 °C	10 s at 900 ± 10 °C
Cooling	10 s from 550 to 25 °C	10 s from 750 to 25 °C	10 s from 900 to 25 °C
Preload	1.57 kN ± 10 lb	1.57 kN ± 10 lb	1.57 kN ± 10 lb
Resulting Maximum Stress	241 ± 10 MPa	241 ± 10 MPa	241 ± 10 MPa
Resulting Minimum Stress	117 ± 7 MPa	65 ± 7 MPa	34 ± 7 MPa
Load Ratio (R)	0.70	0.27	0.14

Table 1: Thermal and preload test parameters and resulting stresses for the tested thermal cycling temperature ranges. Note that the stress is out-of-phase with the temperature.

		Helium	Air	Hydrogen
25 to 900 °C	Failure	None	2782 2647 4786 2106	24 3 30 11 10
	Test Terminated (No Failure)	4100 4164 6467 4145 4626	4100 6330	None
25 to 750 °C	Failure	None	None	36 1828 46
	Test Terminated (No Failure)	4108 4230	6262 6033 5626 3000 4000	1430 200 3000
25 to 550 °C	Test Terminated (No Failure)	N/A	N/A	3000

Table 2: Test results of thermal fatigue testing in helium, hydrogen, and air.

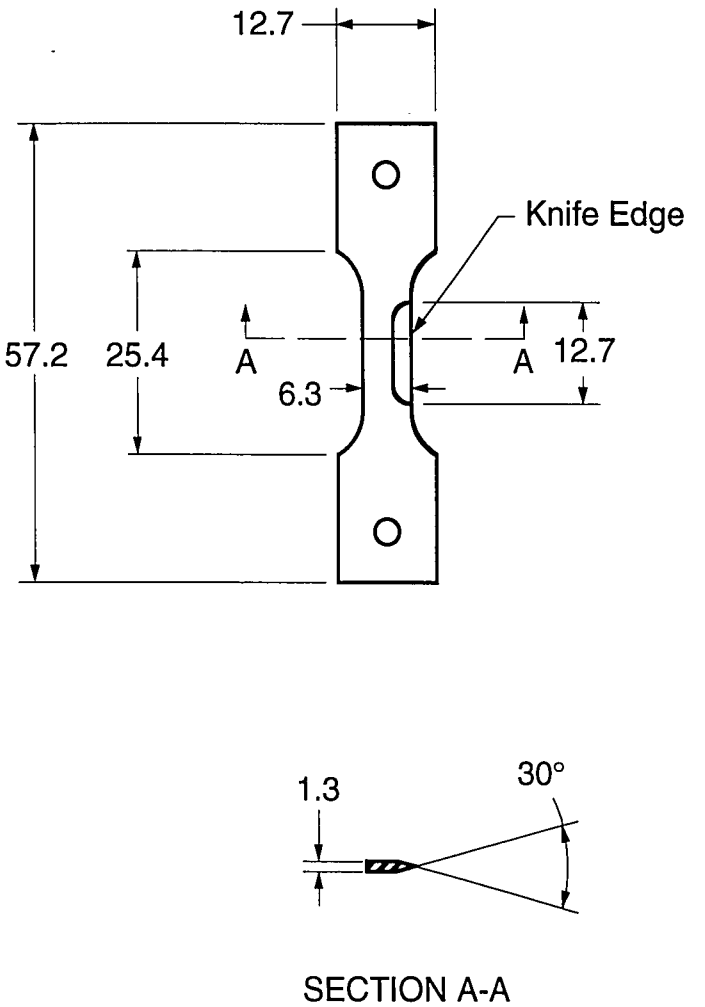

Dimensions in millimeters

Figure 2.1: Thermal fatigue test specimen design.

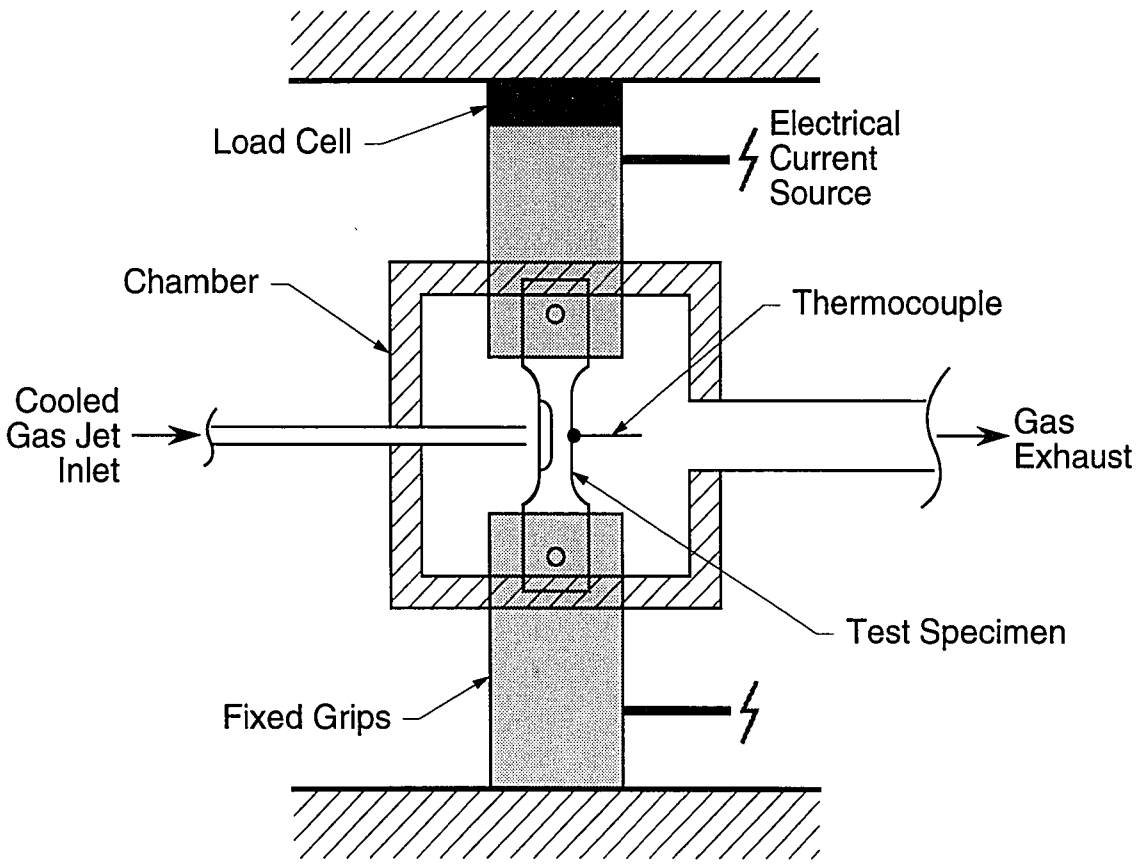

Figure 2.2: Schematic diagram of the thermal fatigue test fixture.

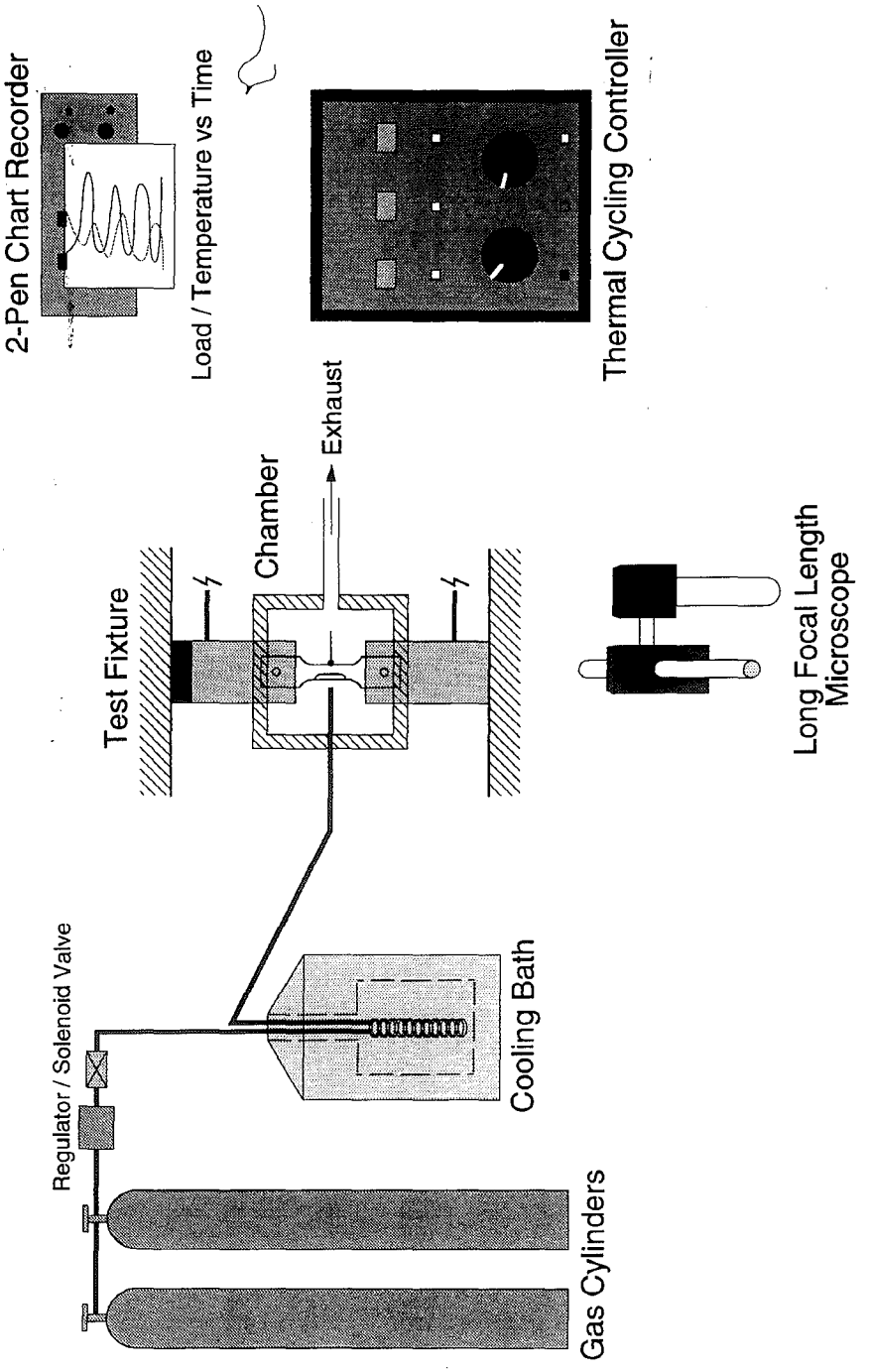

Figure 2.3: Thermal fatigue test system schematic.

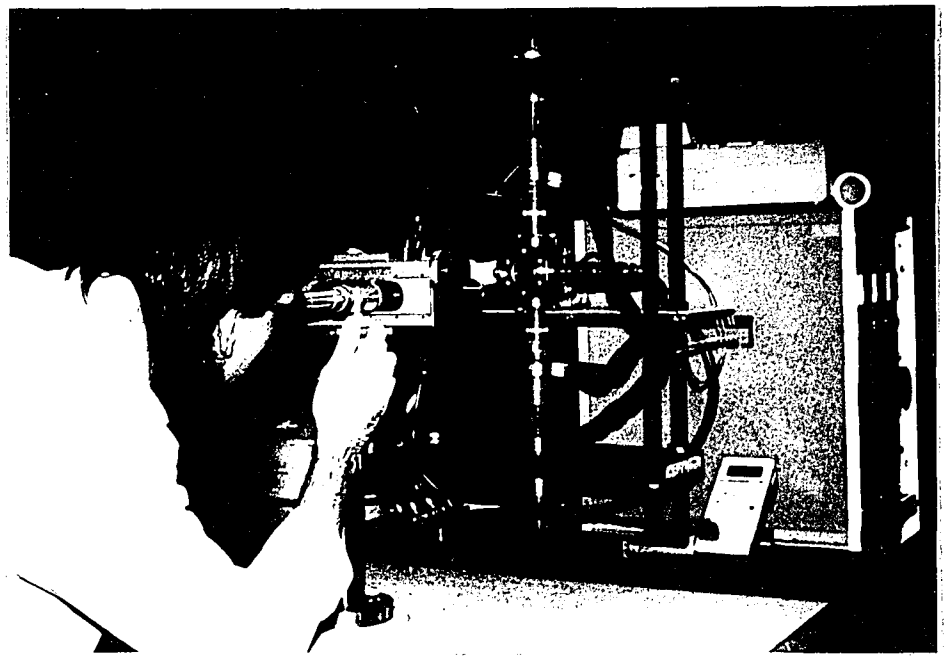

(a)

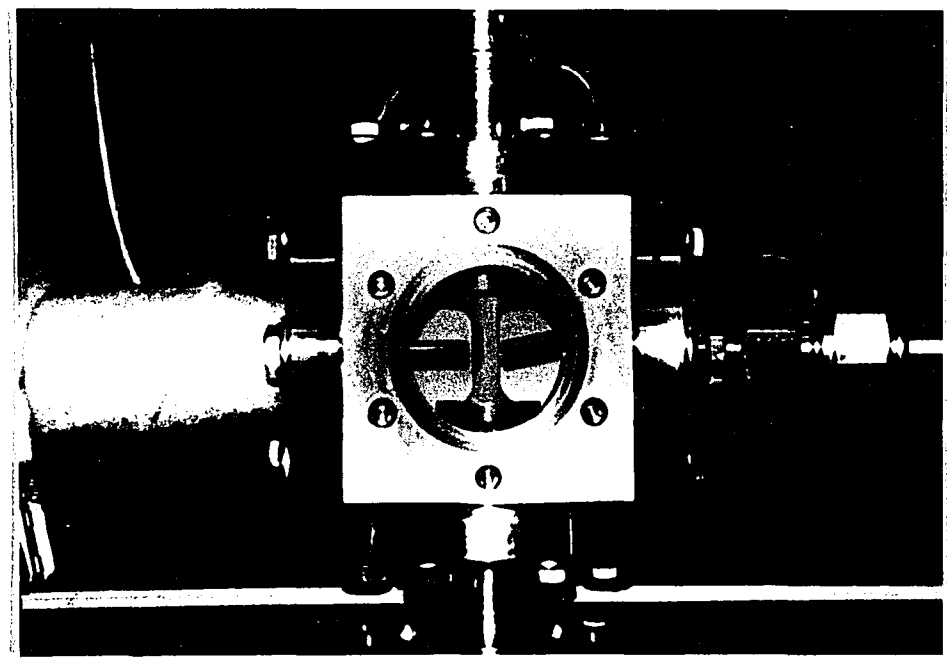

(b)

Figure 2.4: Photographs of the (a) thermal fatigue test apparatus and (b) test chamber with front window flange removed.

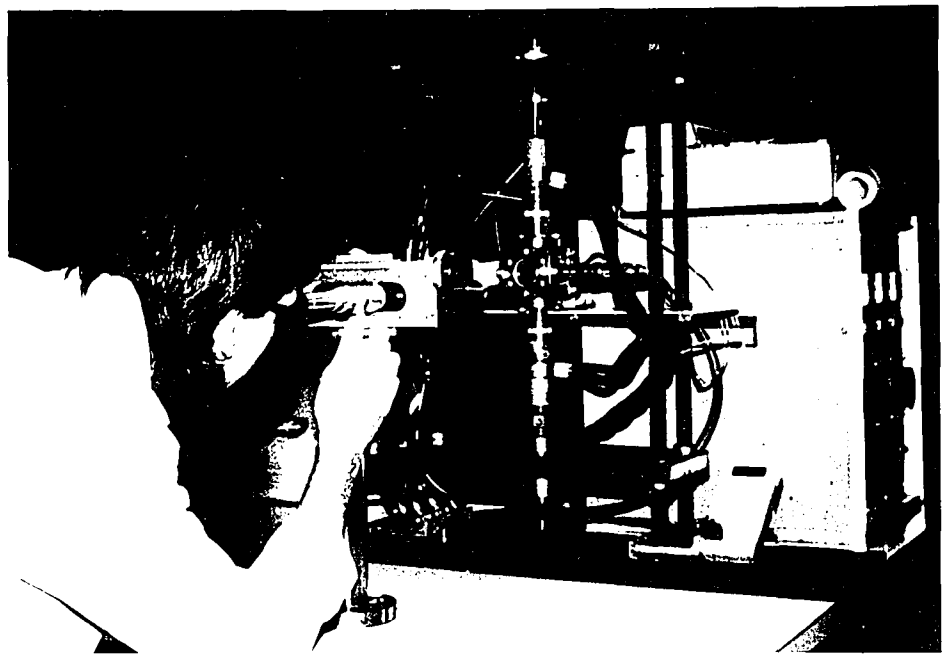

(a)

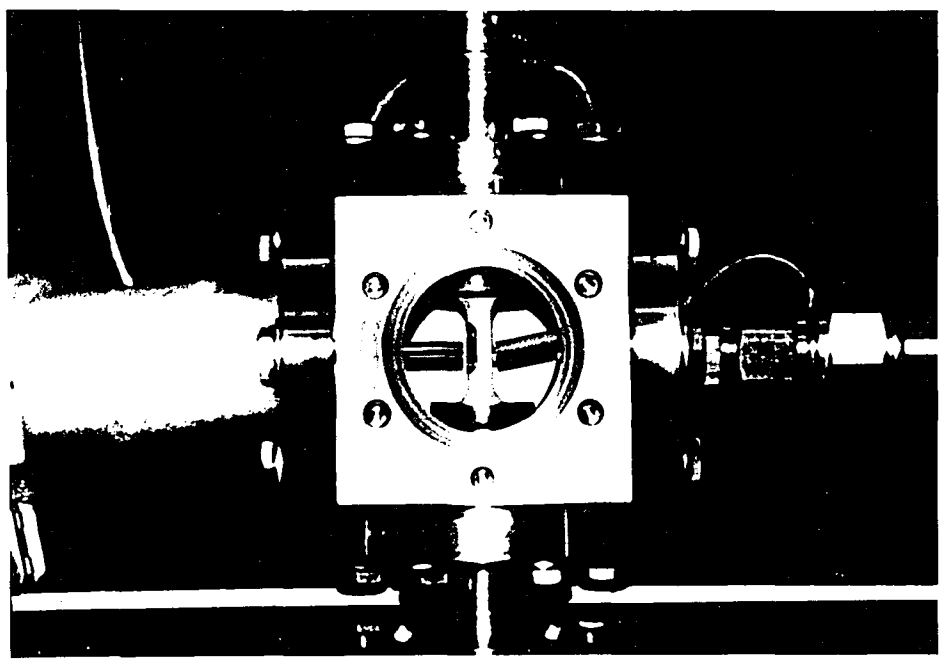

(b)

Figure 2.4: Photographs of the (a) thermal fatigue test apparatus and (b) test chamber with front window flange removed.

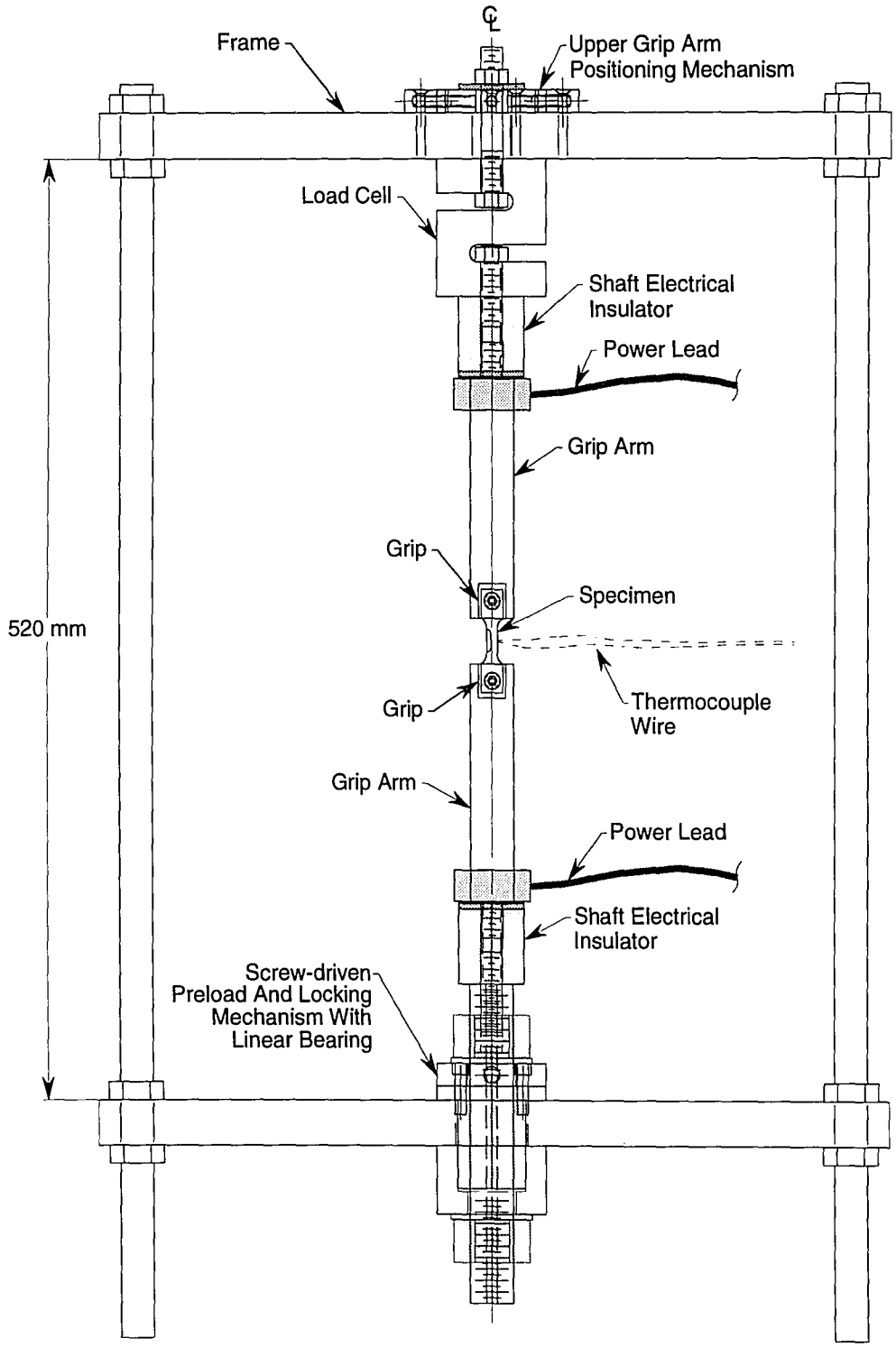

Figure 2.5: Assembly drawing of the thermal fatigue test fixture detailing the load train.

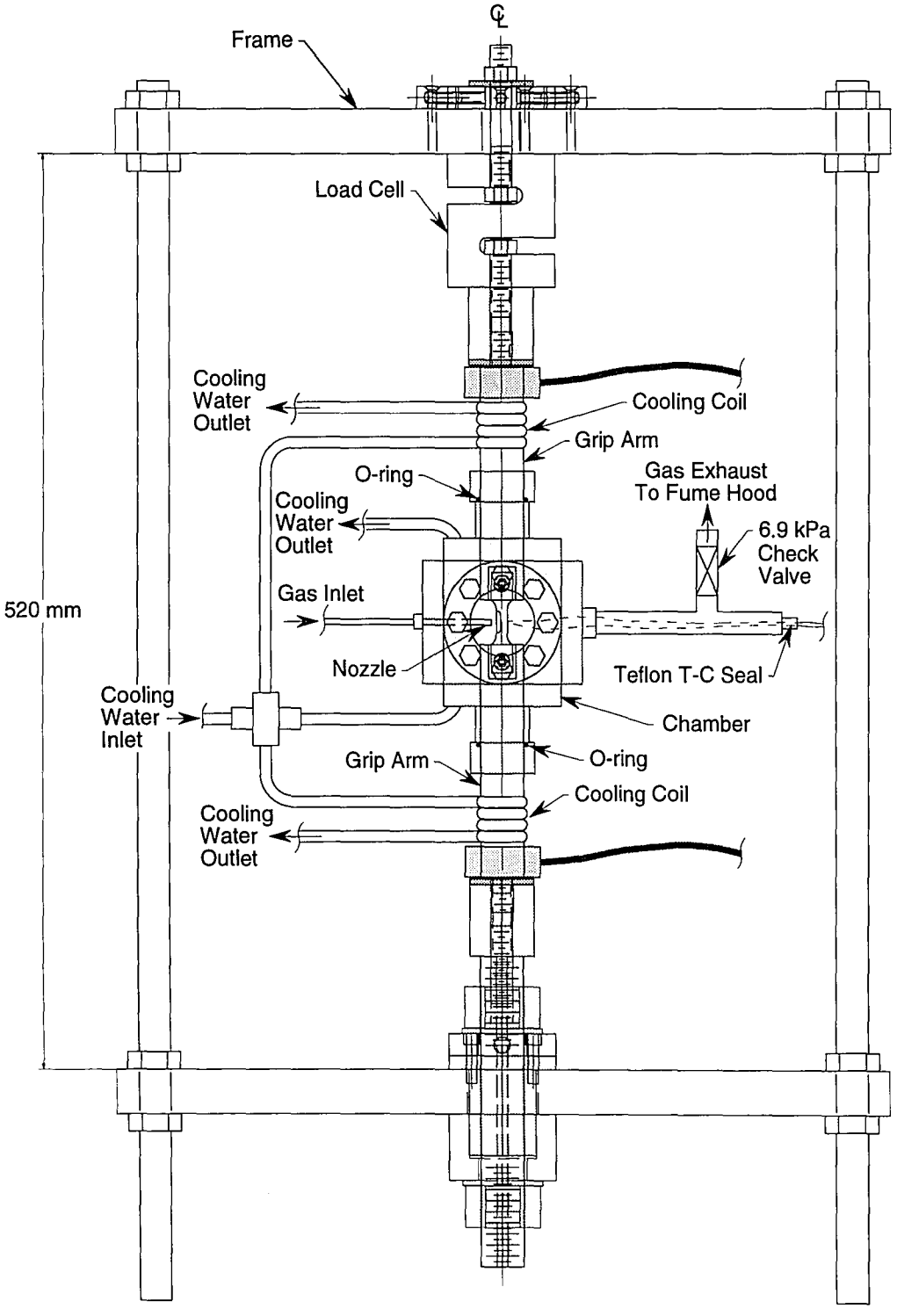

Figure 2.6: Assembly drawing of the thermal fatigue test fixture showing the environmental chamber, cooling system, and gas attachments.

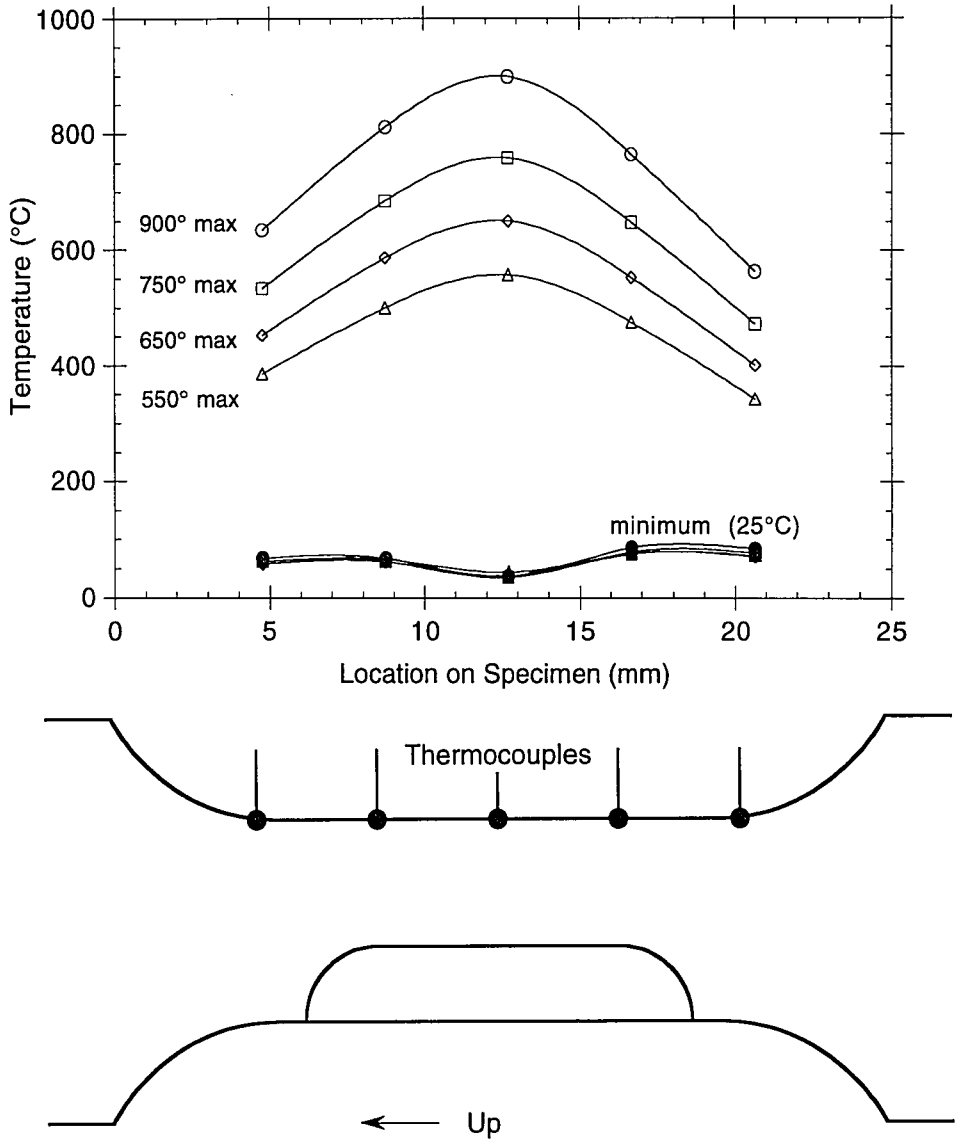

Figure 2.7: Thermal profiles along the thermal fatigue specimen gauge length at maximum and minimum temperatures for thermal cycling ranges between 25 °C and 900, 750, 650, and 550°C. Accuracy: ± 2.2°C or 0.75%, whichever is greater.

Figure 3.1: Cast structure of the Ti-48Al-2Cr ingot, showing a thin layer of chill zone and well-developed columnar zone.

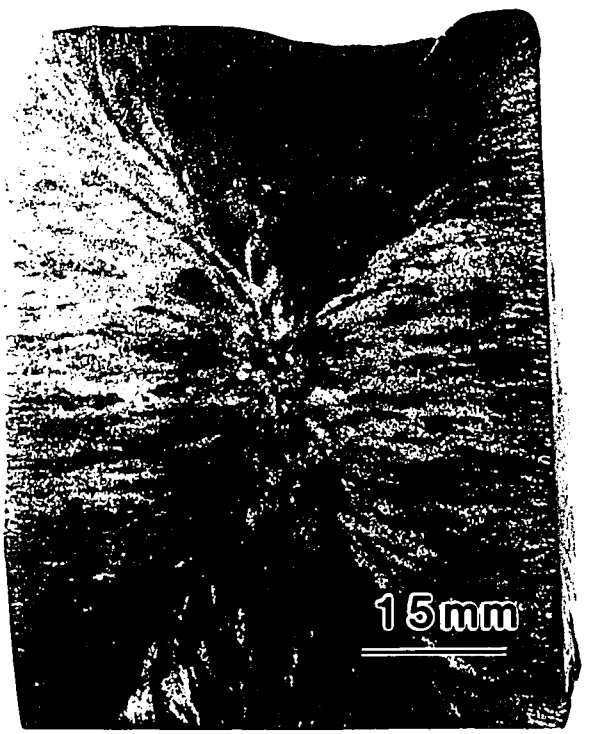

Figure 3.1: Cast structure of the Ti-48Al-2Cr ingot, showing a thin layer of chill zone and well-developed columnar zone.

(a)

(b)

Figure 3.2: Optical micrographs of columnar zone, showing deformed lamellar structure and gamma grains.

(a) low magnification

(b) higher magnification

(a)

(b)

Figure 3.2: Optical micrographs of columnar zone, showing deformed lamellar structure and gamma grains.

(a) low magnification

(b) higher magnification

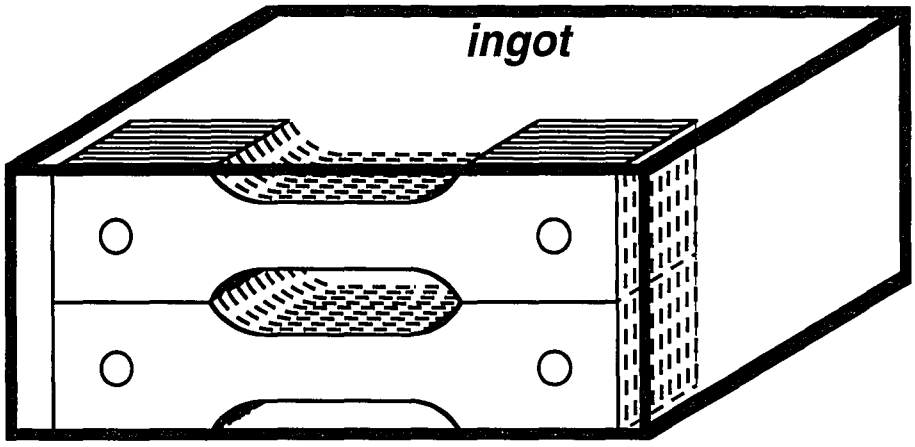

Figure 3.3: Specimen orientation in the ingot.

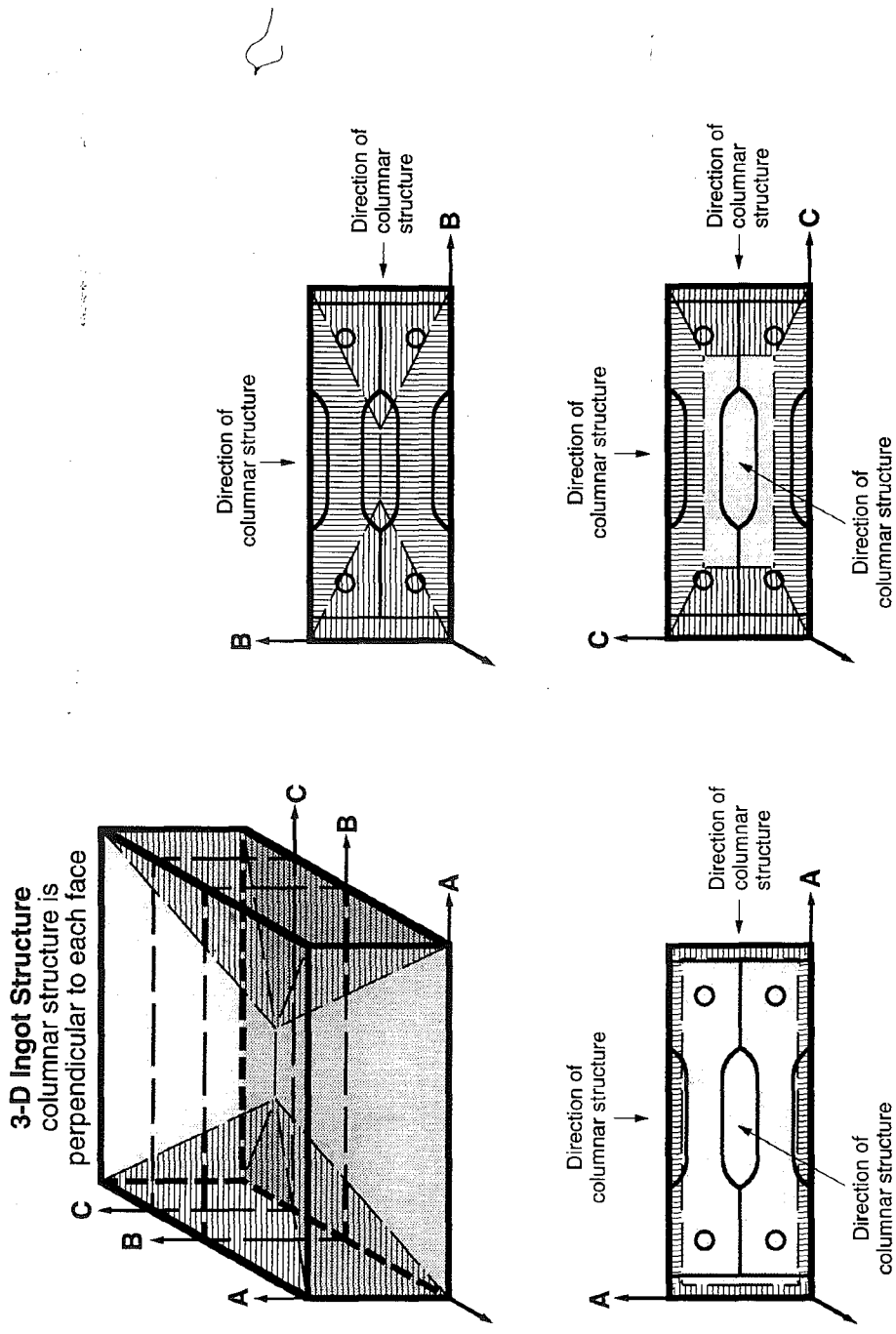

Figure 3.4: Specimen gauge length is oriented with the loading axis always perpendicular to columnar zone.

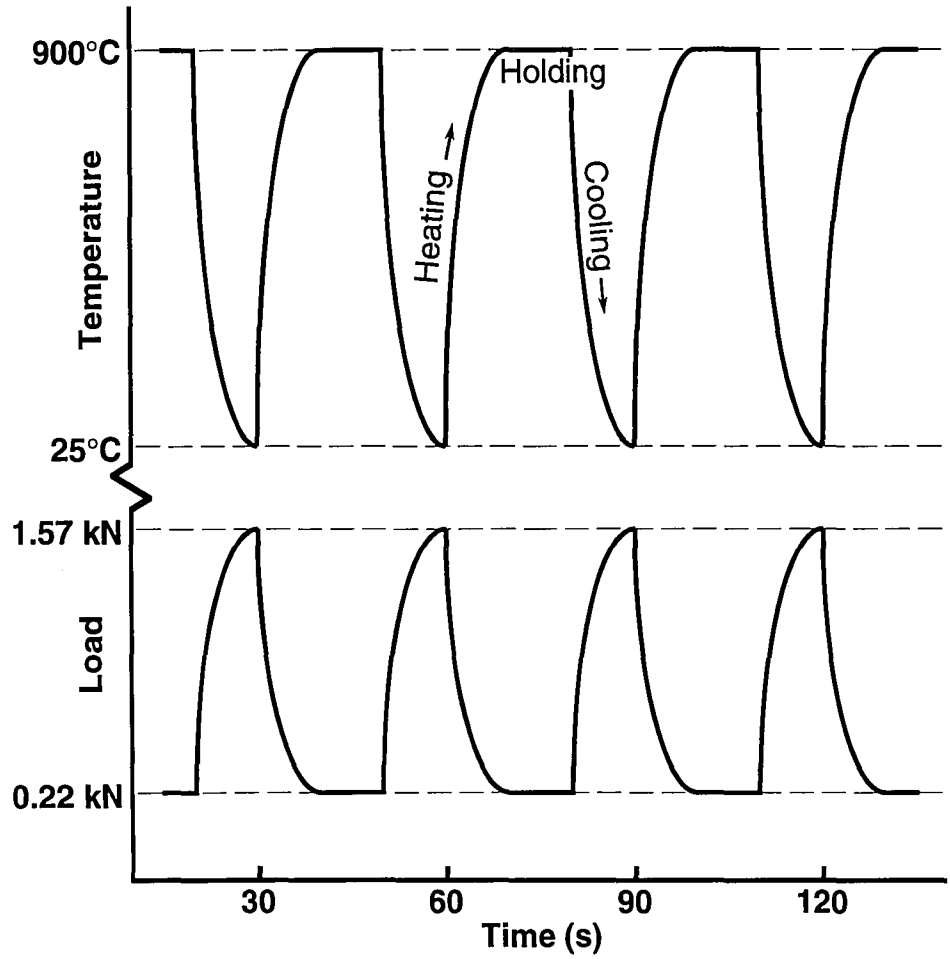

Figure 3.5: Typical thermal and loading cycling profiles.

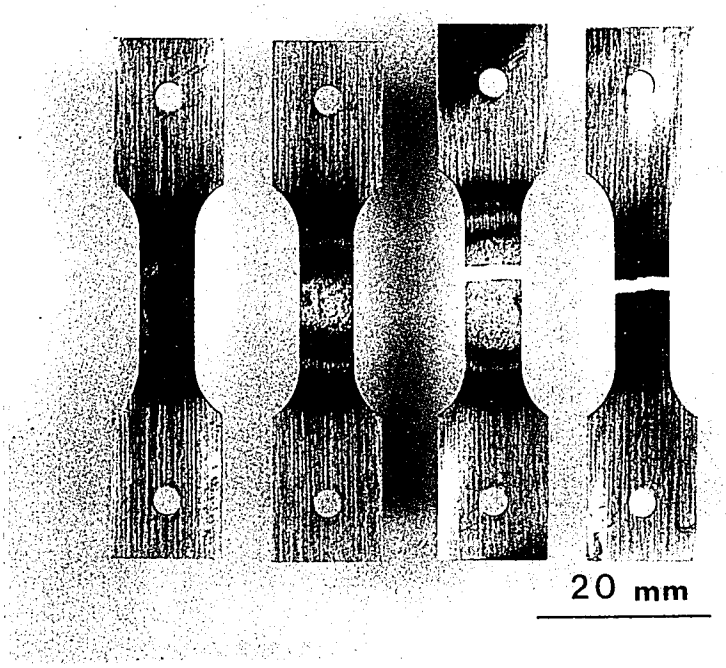

	He	Air	Air*	H_2*
cycles:	4626	4100	2647	10

* fractured

Figure 3.6: Specimen morphology after thermal cycling to 900°C in various environments.

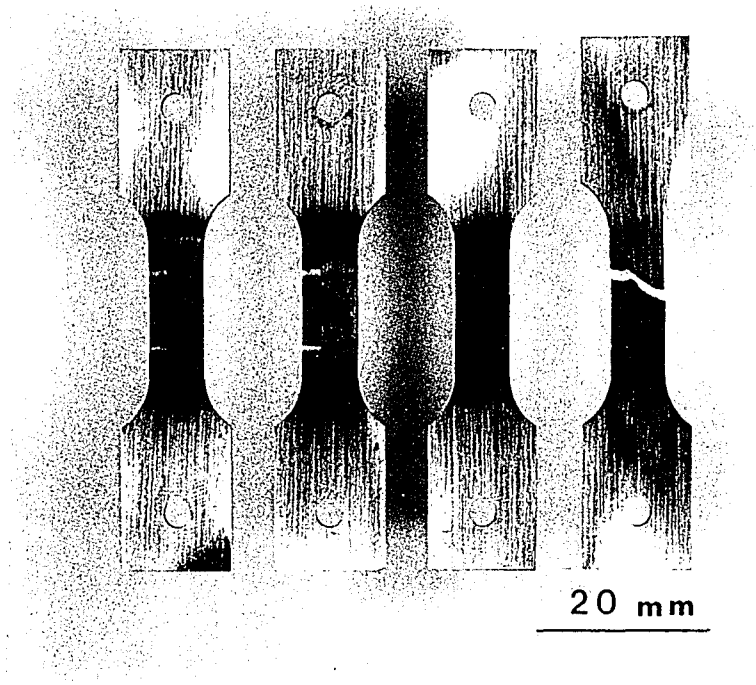

	He	Air	H_2	H_2*
cycles:	4108	6033	1430	36

* fractured

Figure 3.7: Specimen morphology after thermal cycling to 750°C in various environments.

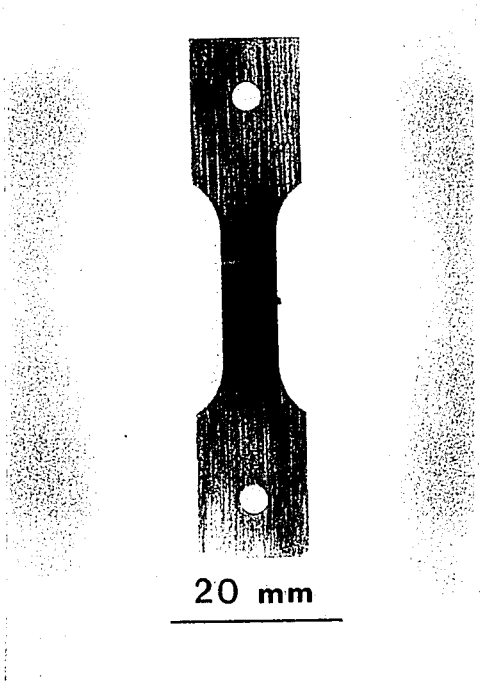

Figure 3.8: Specimen morphology after thermal cycling to 550°C in hydrogen.

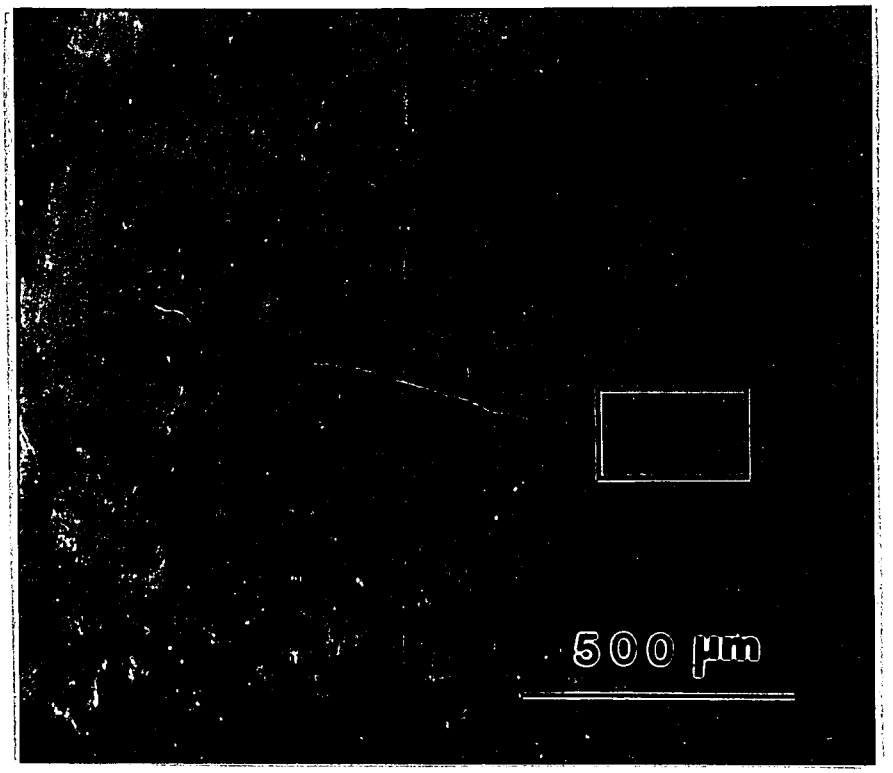

(a)

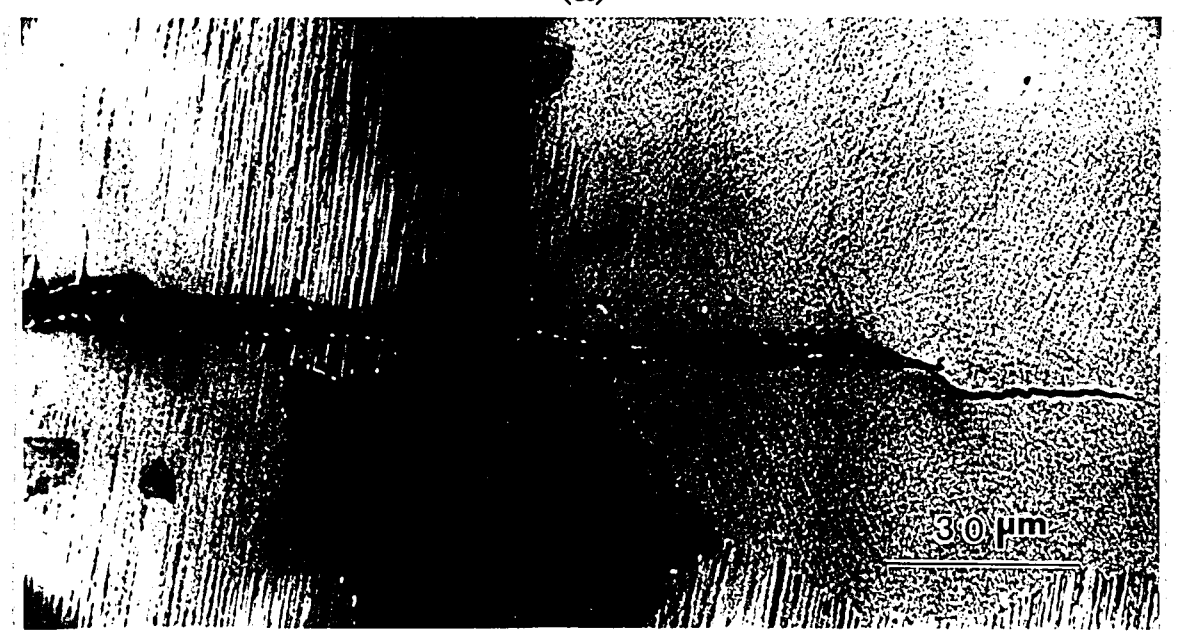

(b)

Figure 3.9: Backscattered electron image of a portion of a specimen tested in helium for 4,100 cycles, showing (a) a small surface crack about 1 mm long, and (b) an enlarged portion of that crack.

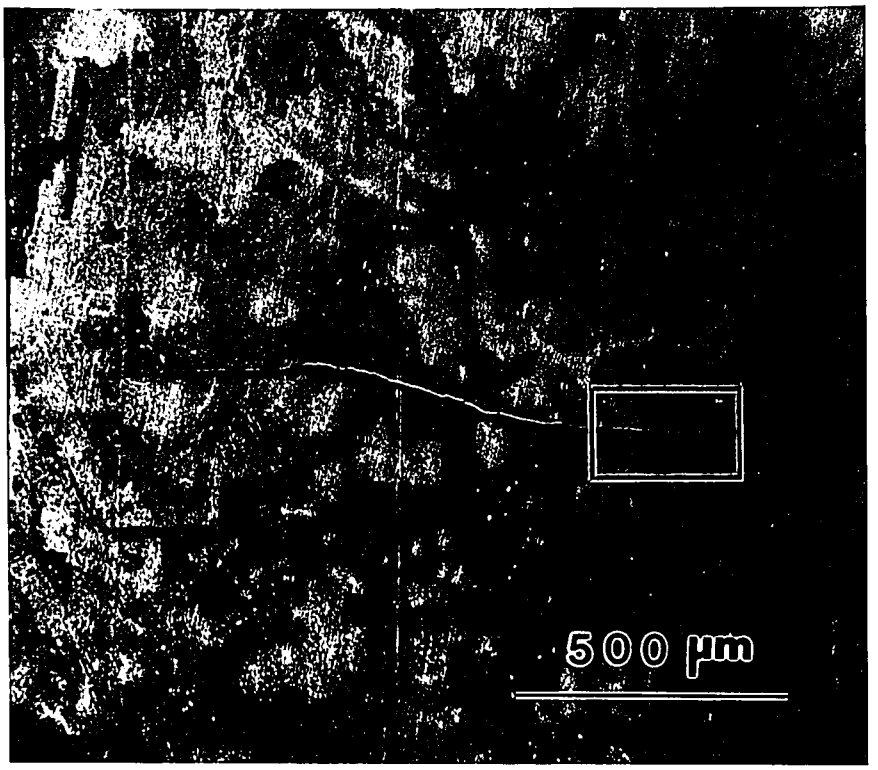

(a)

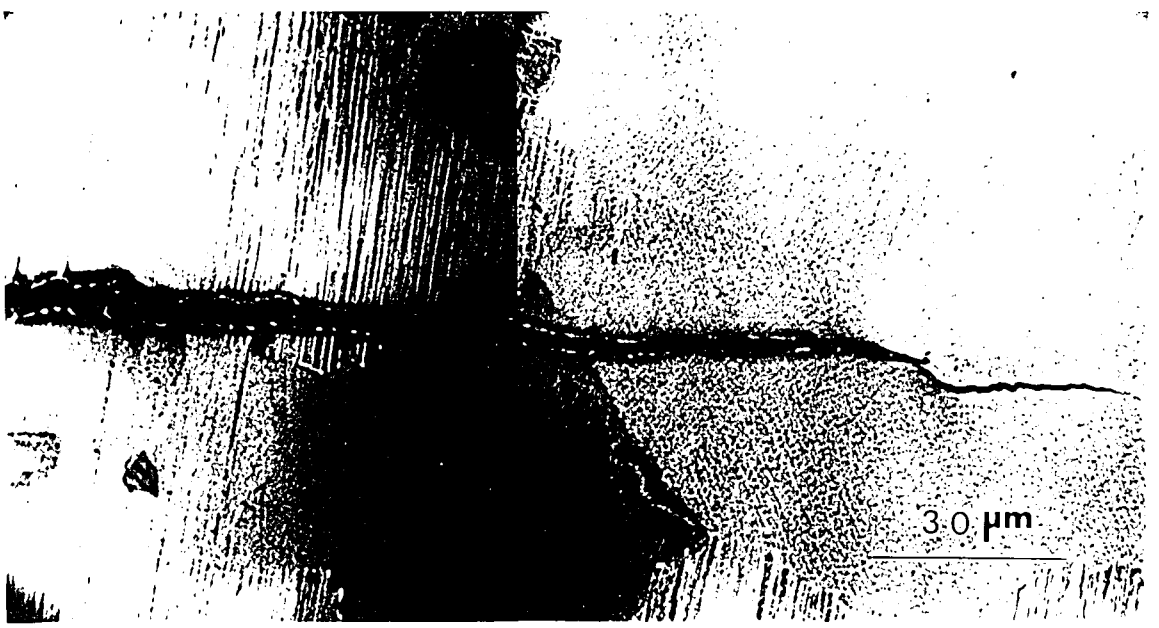

(b)

Figure 3.9: Backscattered electron image of a portion of a specimen tested in helium for 4,100 cycles, showing (a) a small surface crack about 1 mm long, and (b) an enlarged portion of that crack.

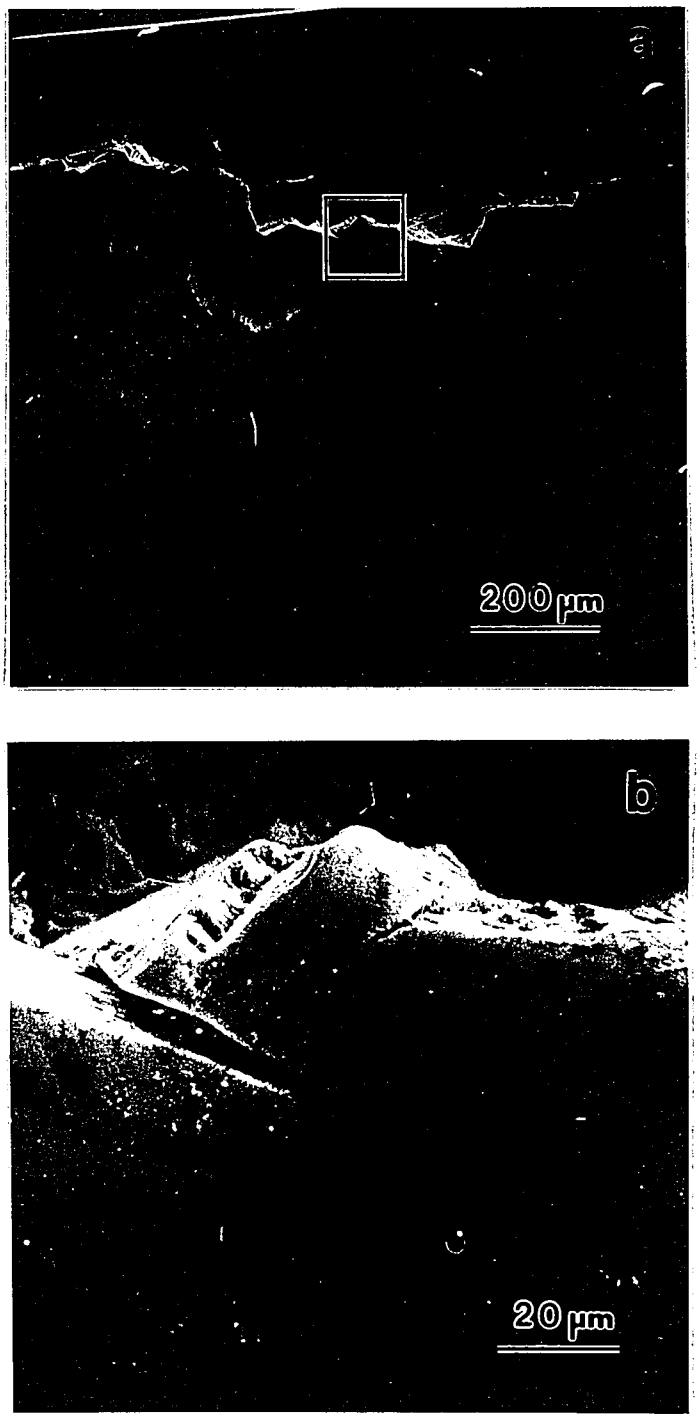

Figure 3.10: Backscattered electron image of a specimen (polished) thermally cycled in air between 25 and 900 °C. (a) Region near the primary crack and (b) secondary cracks. Lifetime: 4,786 cycles.

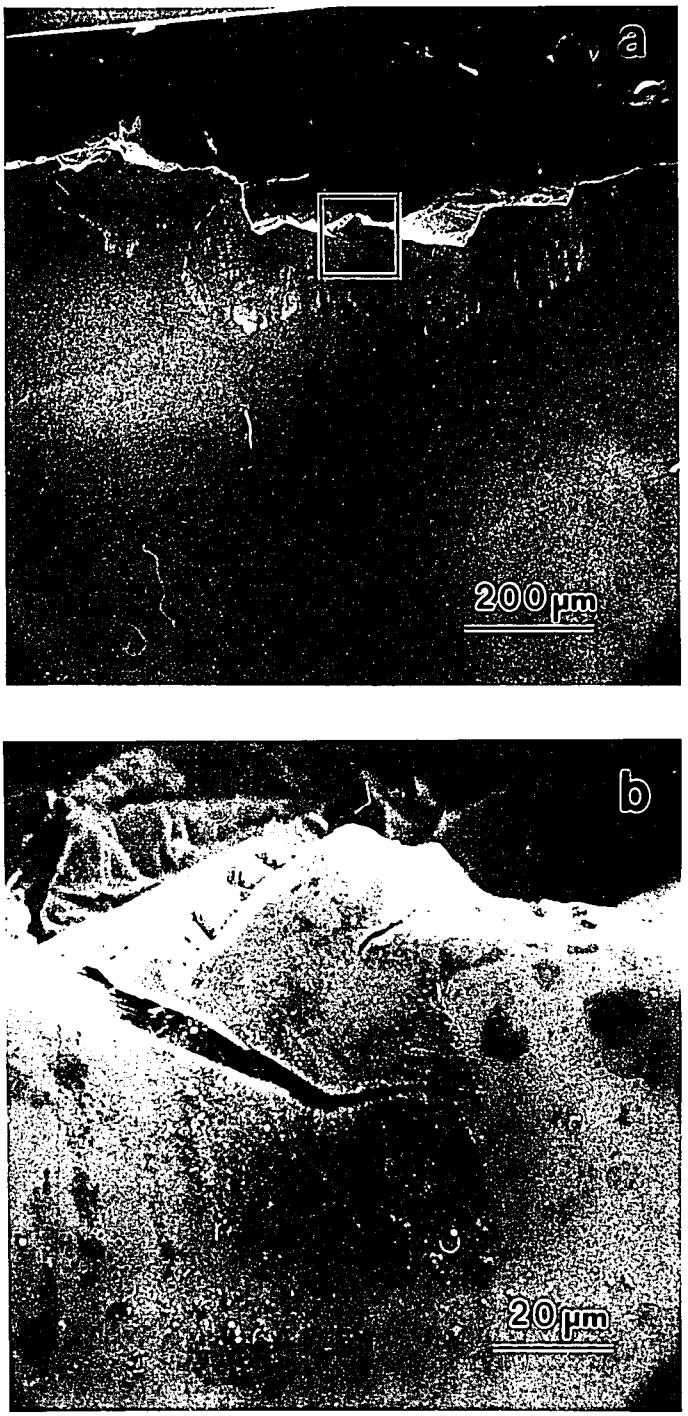

Figure 3.10: Backscattered electron image of a specimen (polished) thermally cycled in air between 25 and 900 °C. (a) Region near the primary crack and (b) secondary cracks. Lifetime: 4,786 cycles.

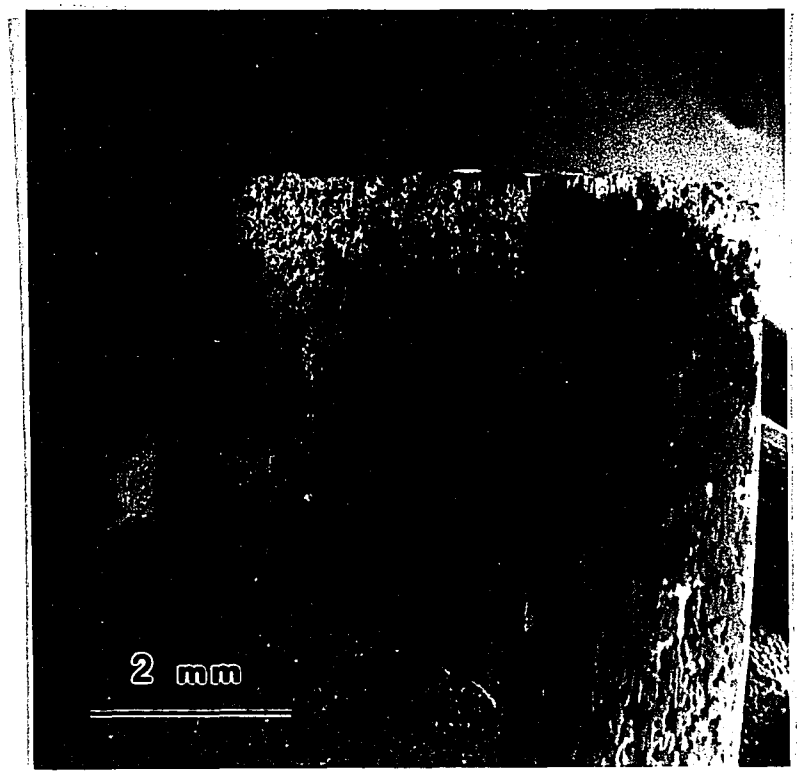

Figure 3.11: SEM image of a specimen thermally cycled in air between 25 and 900°C showing severe oxidation. Lifetime: 2,106 cycles.

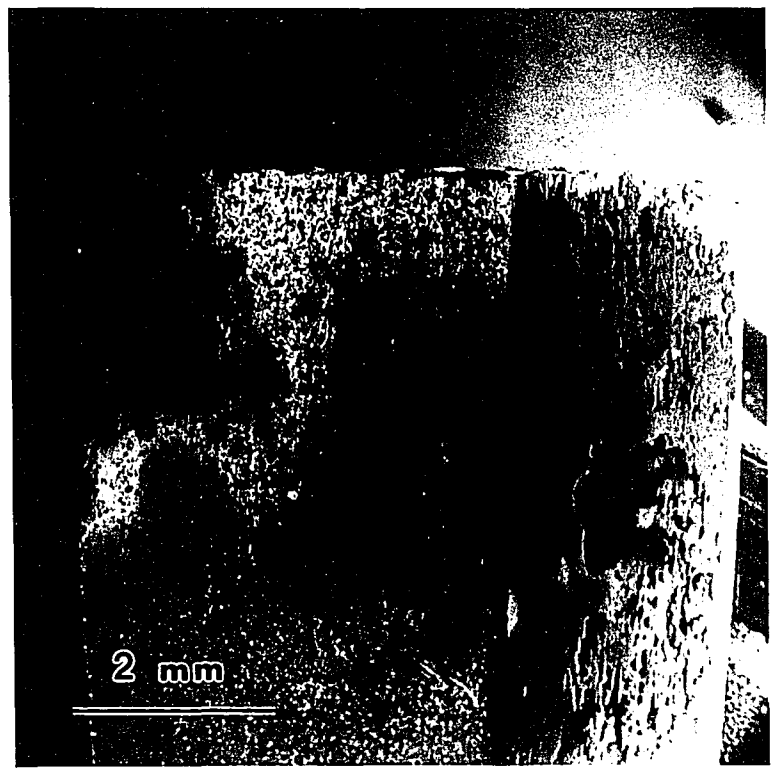

Figure 3.11: SEM image of a specimen thermally cycled in air between 25 and 900°C showing severe oxidation. Lifetime: 2,106 cycles.

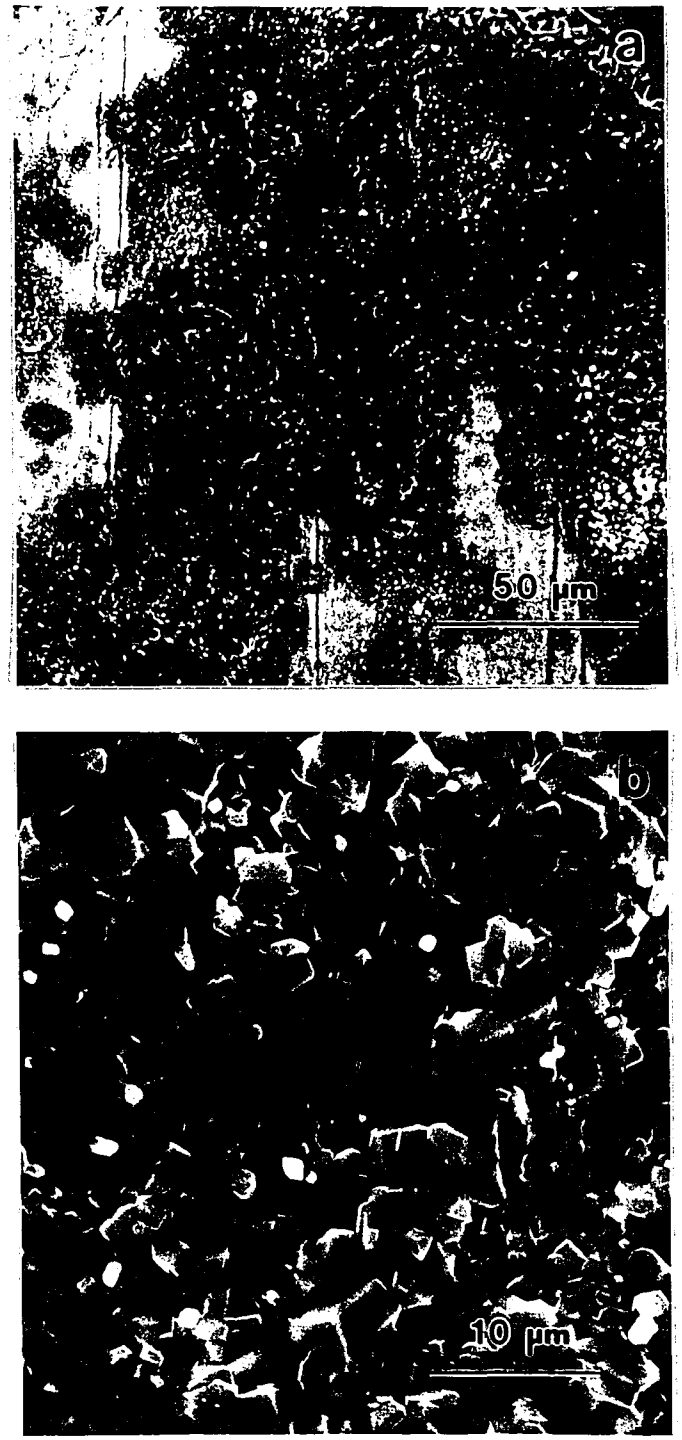

Figure 3.12: Backscattered electron image of a specimen thermally cycled in air between 25 and 900°C showing structure of titanium oxide. Lifetime: 2,106 cycles.

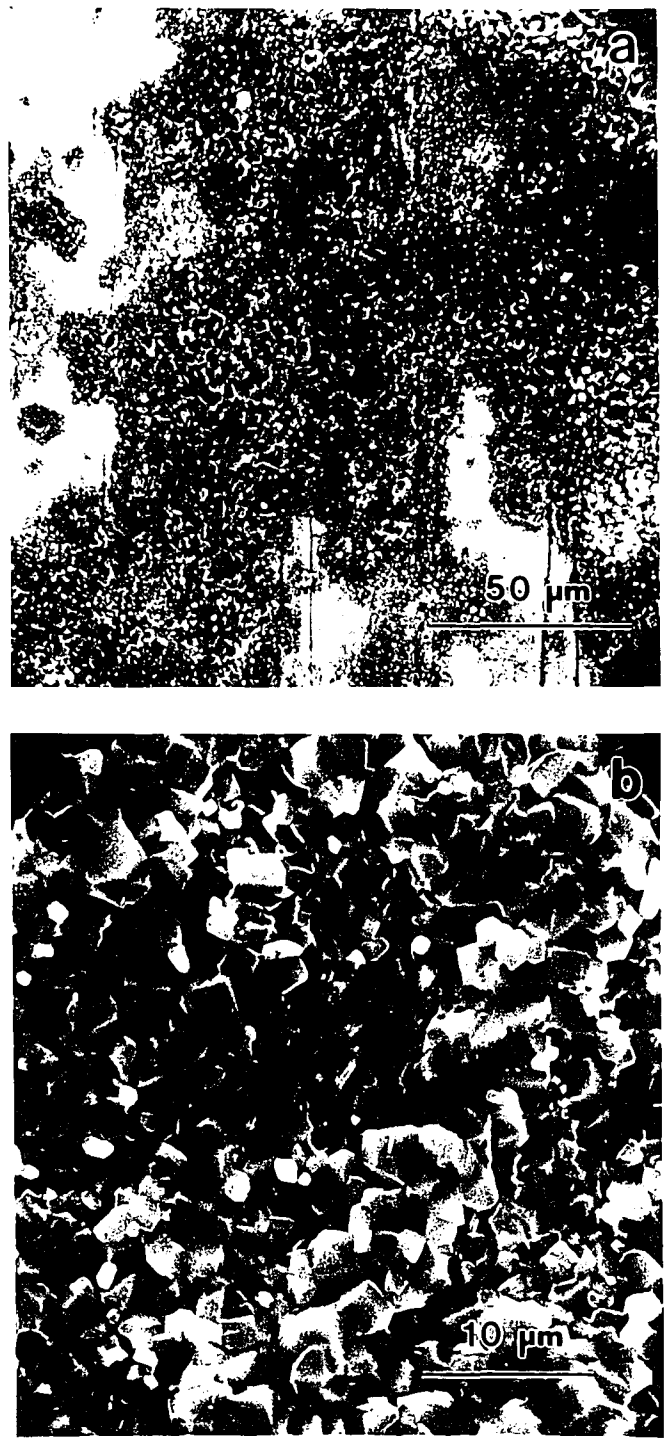

Figure 3.12: Backscattered electron image of a specimen thermally cycled in air between 25 and 900°C showing structure of titanium oxide. Lifetime: 2,106 cycles.

(a)

(b)

Figure 3.13: Surface cracks on a specimen cycled in hydrogen from 25 to 900°C, with a resulting lifetime of 3 cycles.

(a) SEM image

(b) Polarized light microscope image

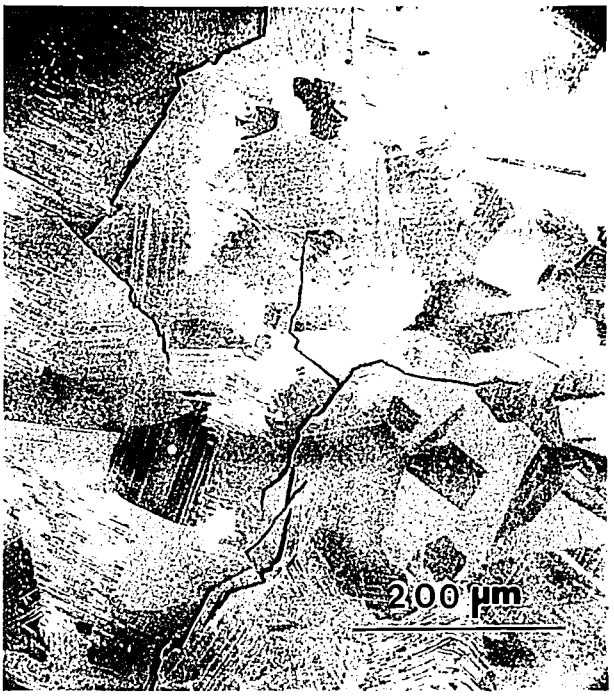

(a)

(b)

Figure 3.13: Surface cracks on a specimen cycled in hydrogen from 25 to 900°C, with a resulting lifetime of 3 cycles.

(a) SEM image

(b) Polarized light microscope image

Figure 3.14: SEM micrographs of the surface of a specimen tested in hydrogen at 900°C, showing extensive surface cracking and grain attack by hydrogen. Lifetime: 3 cycles.

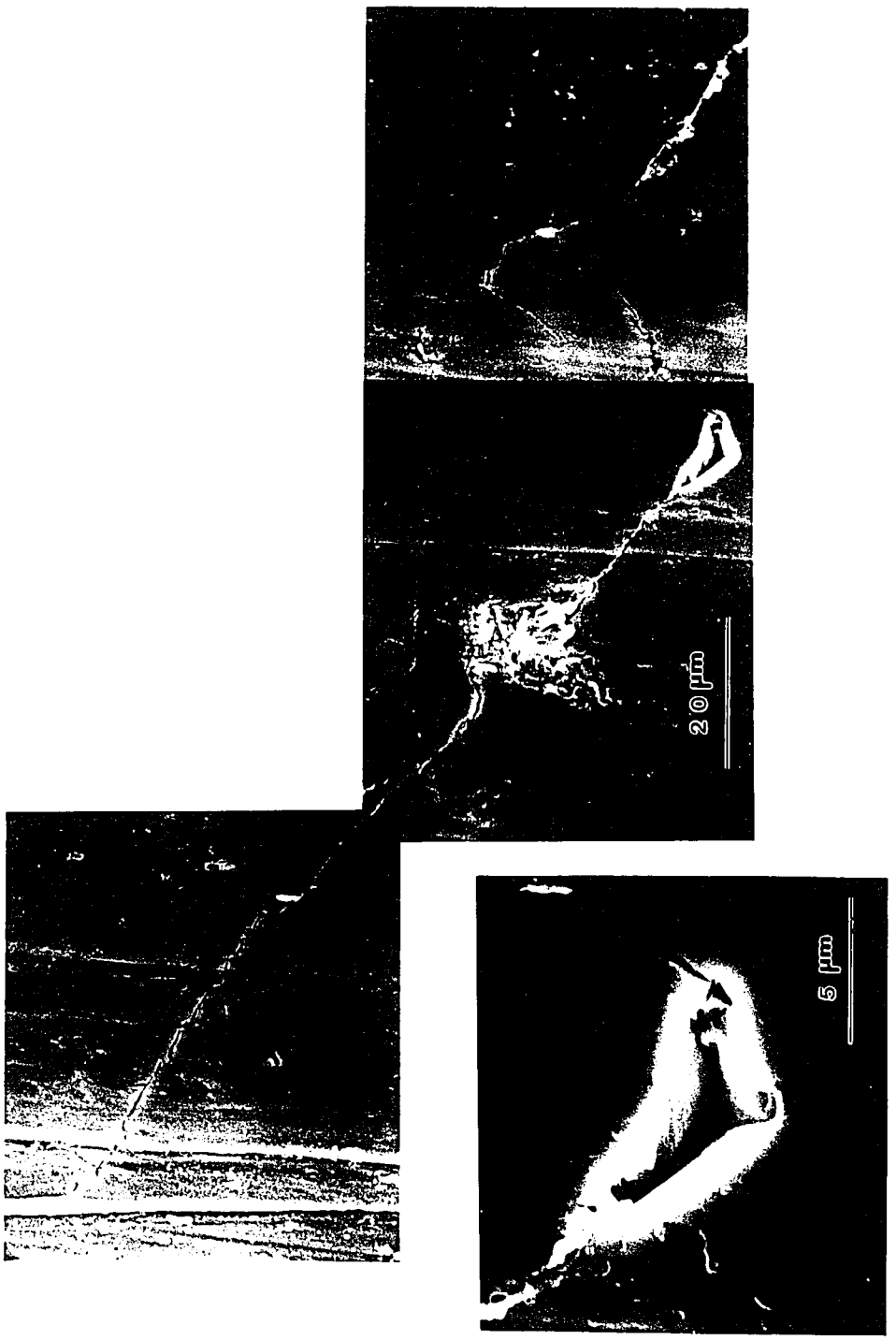

Figure 3.14: SEM micrographs of the surface of a specimen tested in hydrogen at 900°C, showing extensive surface cracking and grain attack by hydrogen. Lifetime: 3 cycles.

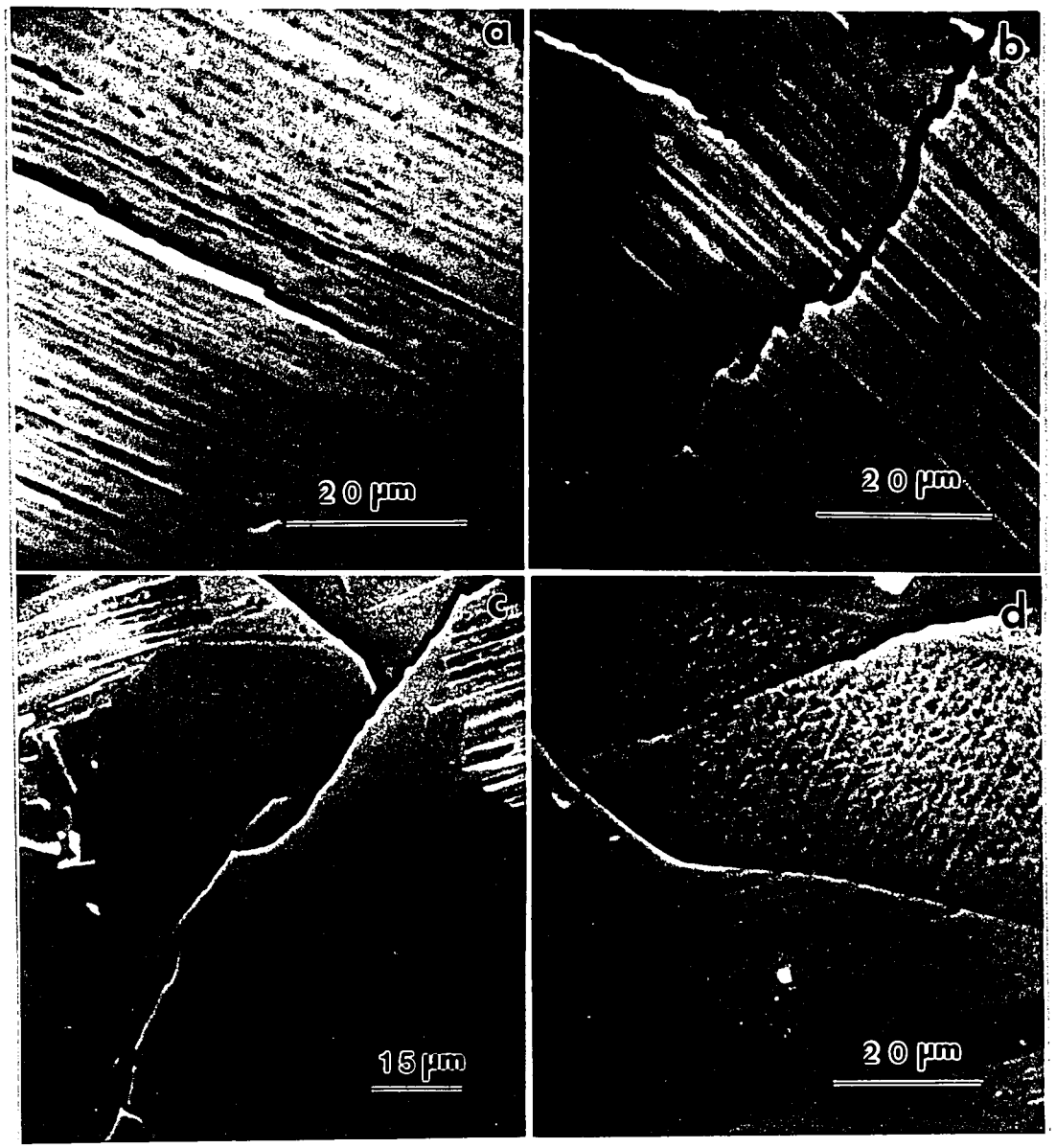

Figure 3.15: Surface cracks produced in hydrogen during thermal cycling between 25 and 900°C.

(a) delamination along α_2/γ interfaces in $(\alpha_2 + \gamma)$ lamellar structure

(b) translamellar cracking

(c) crack through gamma grain

(d) grain boundary separation

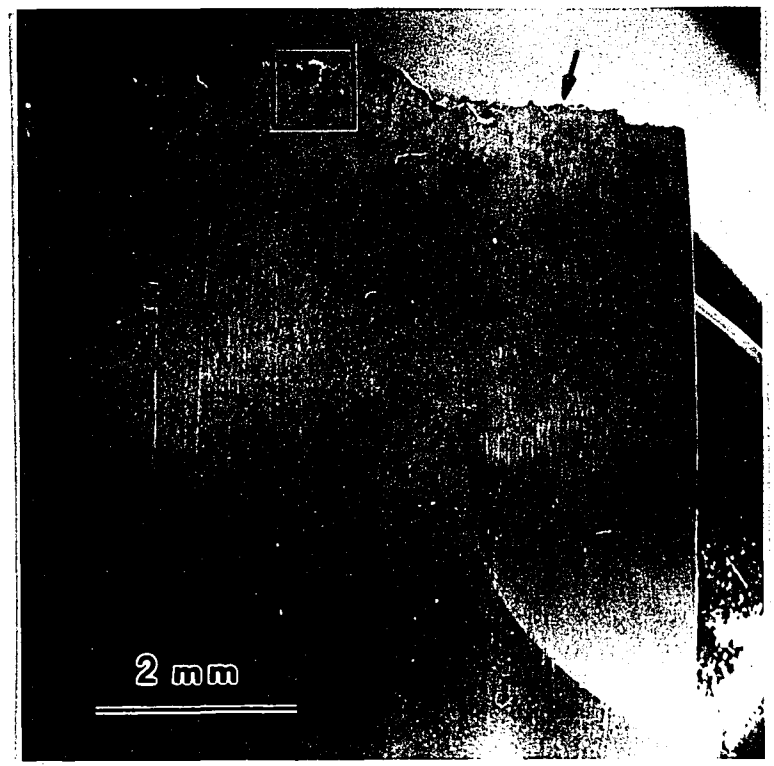

Figure 3.16: Specimen thermally cycled in hydrogen between 25 and 750°C. Highlighted portions detailed in Fig. 3.17. Lifetime: 46 cycles.

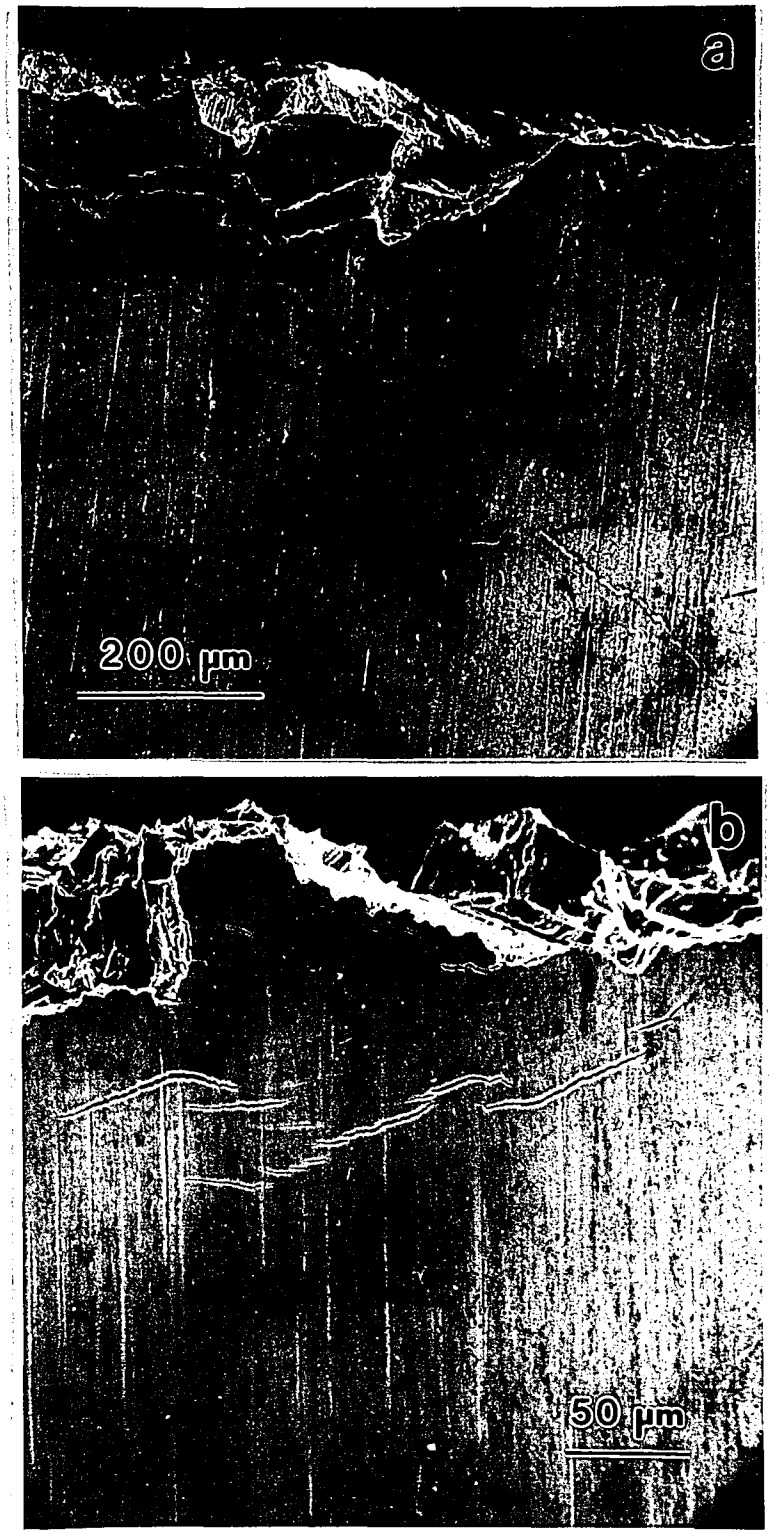

Figure 3.17: SEM image of secondary cracks formed near the primary crack of specimen in Fig. 3.16 during thermal cycling between 25 and 750°C. Lifetime: 46 cycles.

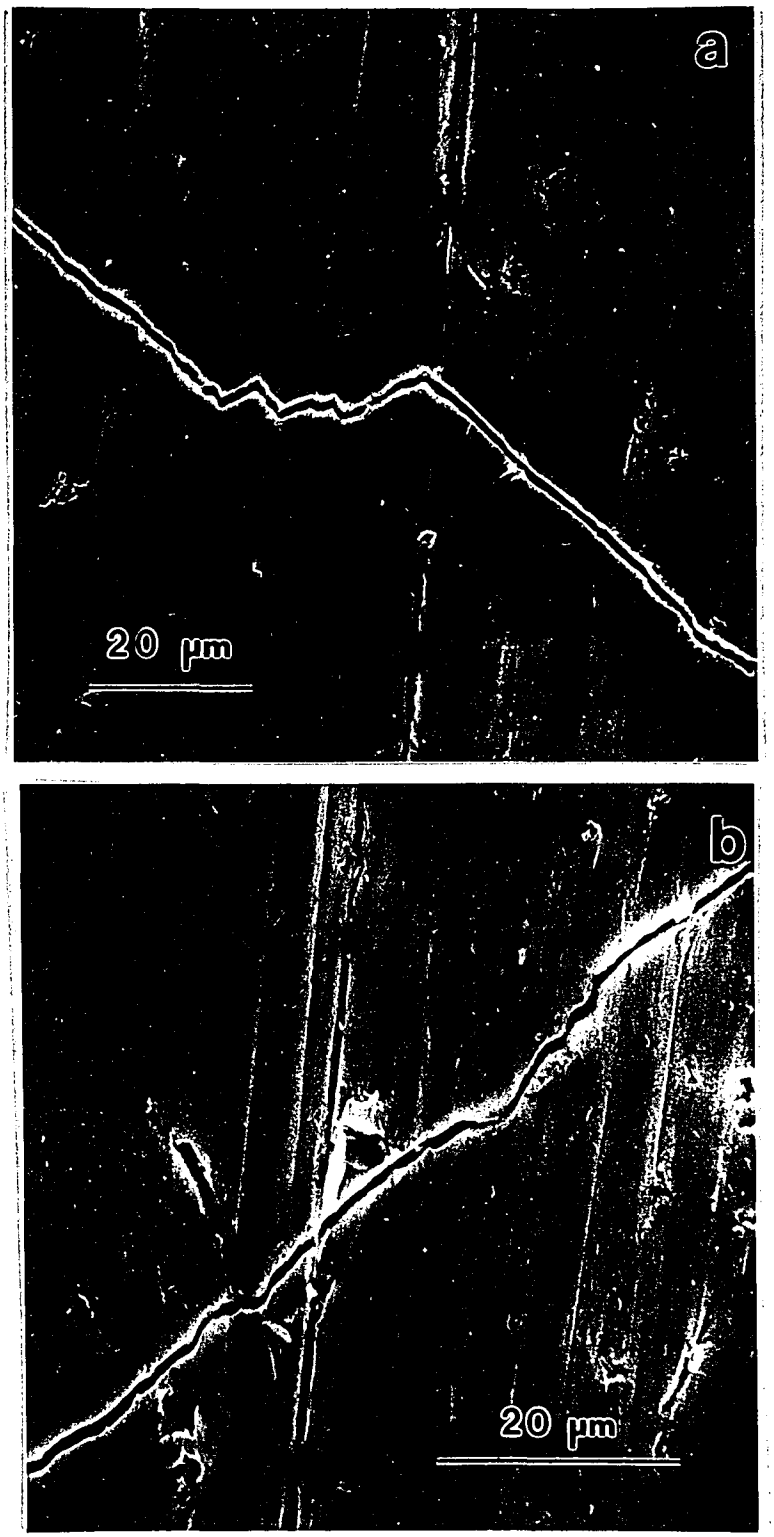

Figure 3.18: Extensive surface cracks and grain attack on specimen thermally cycled in hydrogen from 25 to 750°C. Lifetime: 46 cycles.

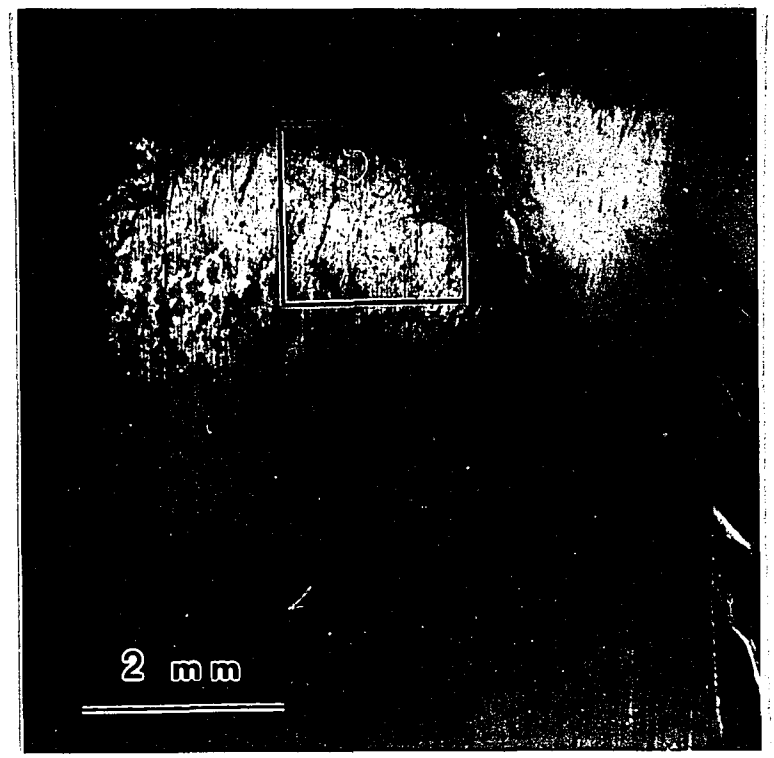

Figure 3.19: SEM image of a specimen with primary and secondary cracks thermally cycled in hydrogen between 25 and 750°C. Lifetime: 1,828 cycles.

Figure 3.19: SEM image of a specimen with primary and secondary cracks thermally cycled in hydrogen between 25 and 750°C. Lifetime: 1,828 cycles.

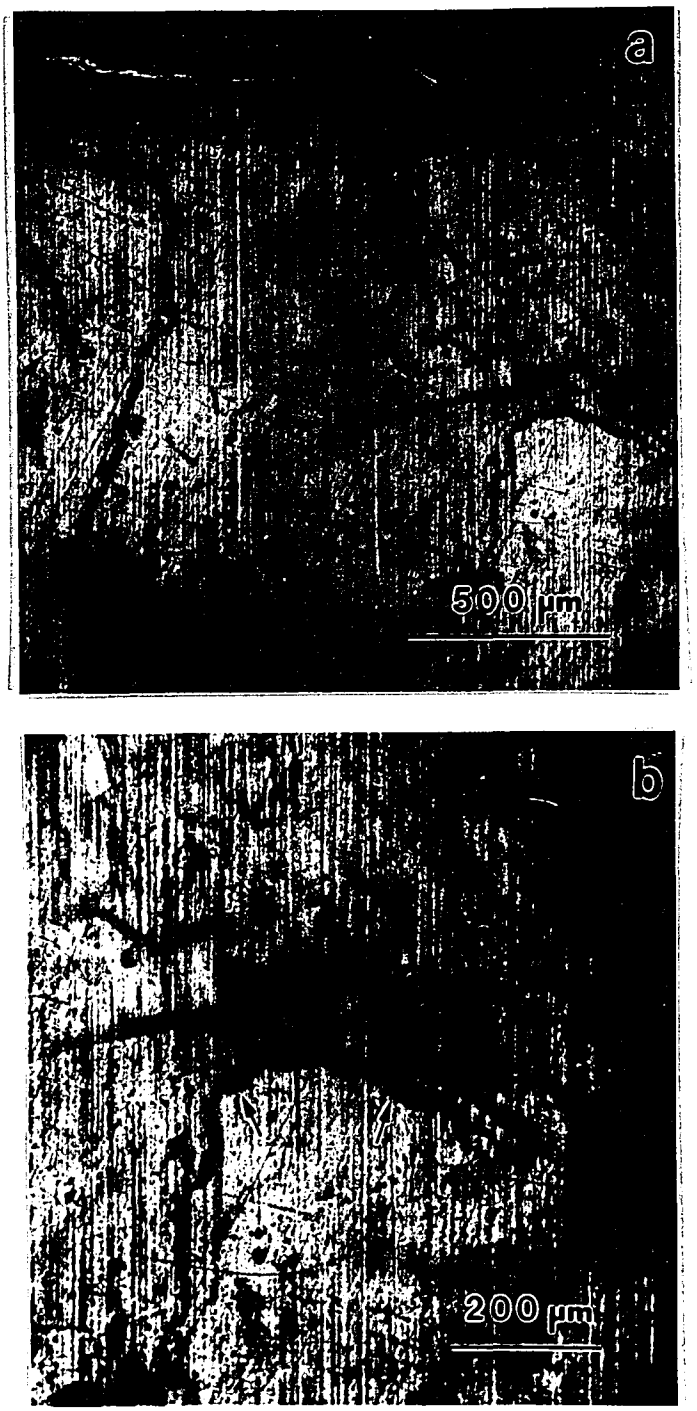

Figure 3.20: SEM image of secondary cracks formed on specimen in Fig. 3.16 during thermal cycling between 25 and 750°C. Lifetime: 1,828 cycles.

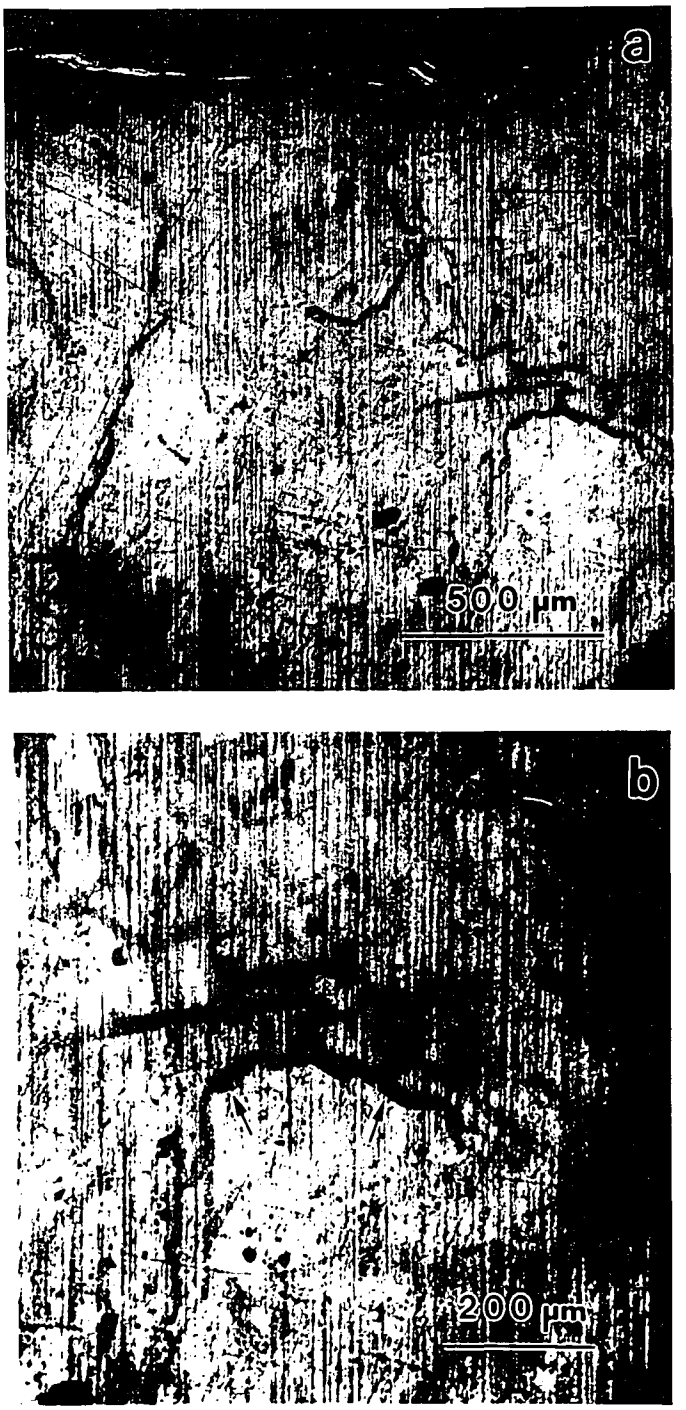

Figure 3.20: SEM image of secondary cracks formed on specimen in Fig. 3.16 during thermal cycling between 25 and 750°C. Lifetime: 1,828 cycles.

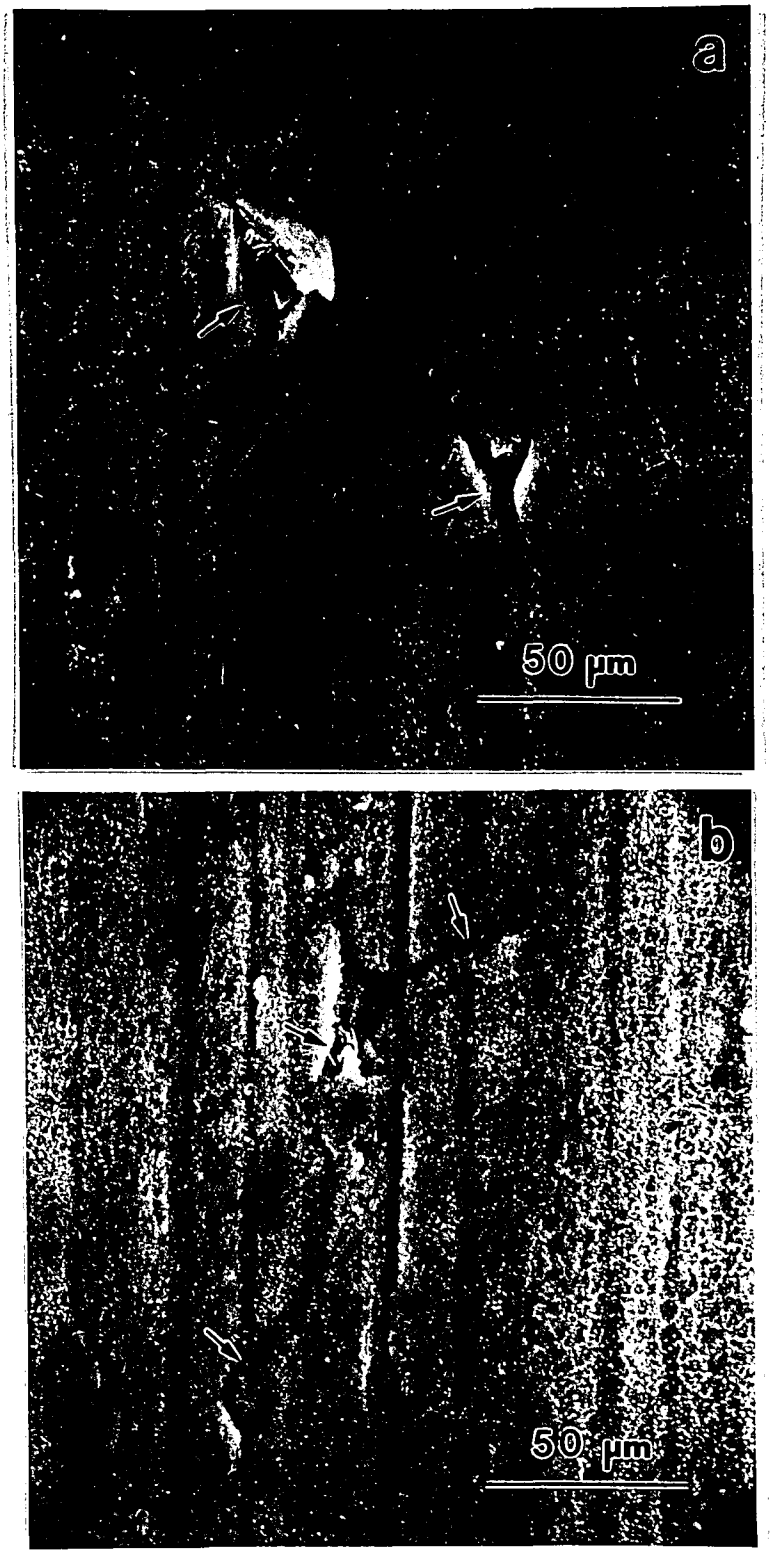

Figure 3.21: SEM image of extensive (a) grain attack and (b) surface cracks on a specimen thermally cycled in hydrogen from 25 to 750°C. Test duration: 200 cycles with no failure.

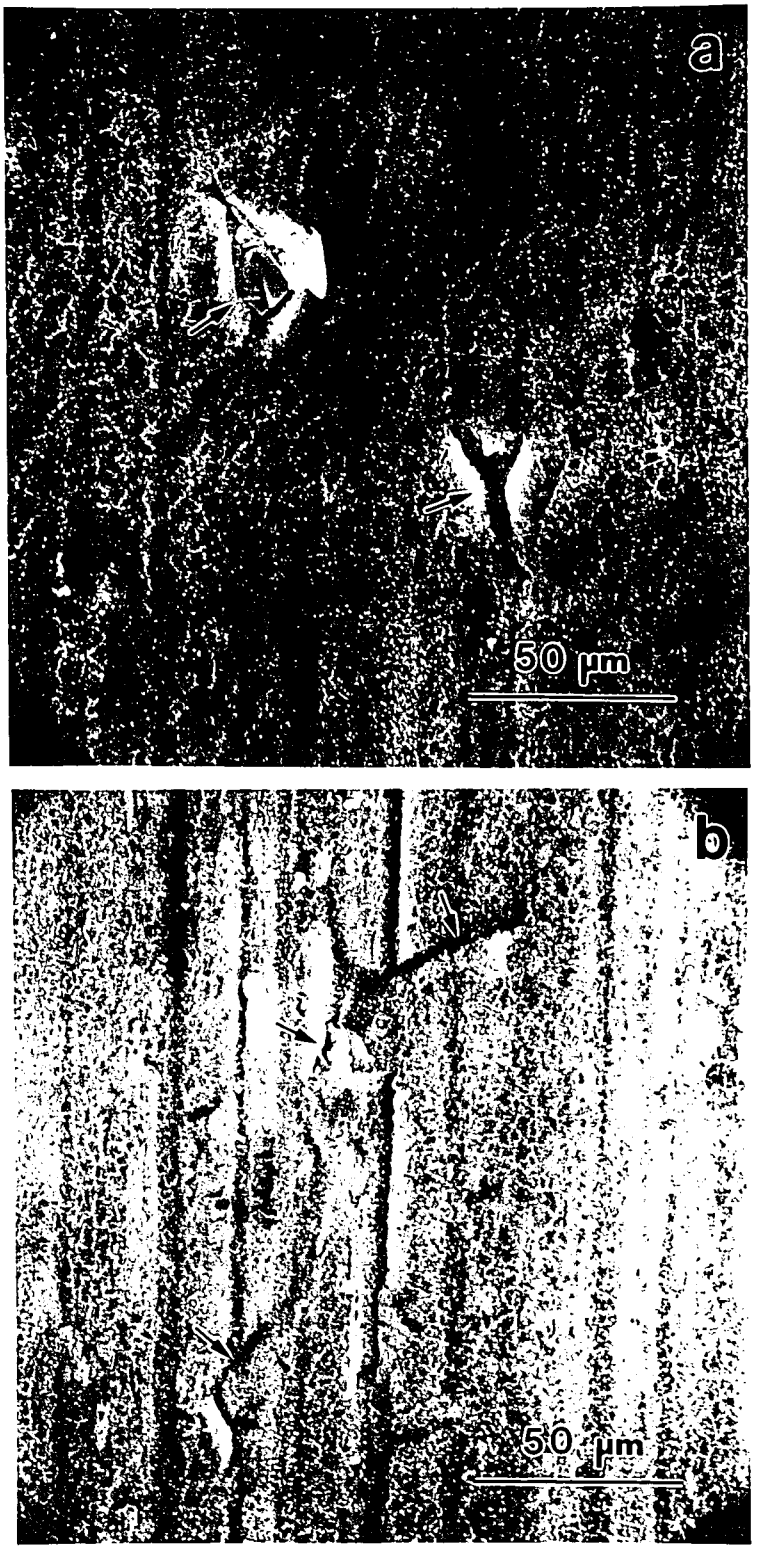

Figure 3.21: SEM image of extensive (a) grain attack and (b) surface cracks on a specimen thermally cycled in hydrogen from 25 to 750°C. Test duration: 200 cycles with no failure.

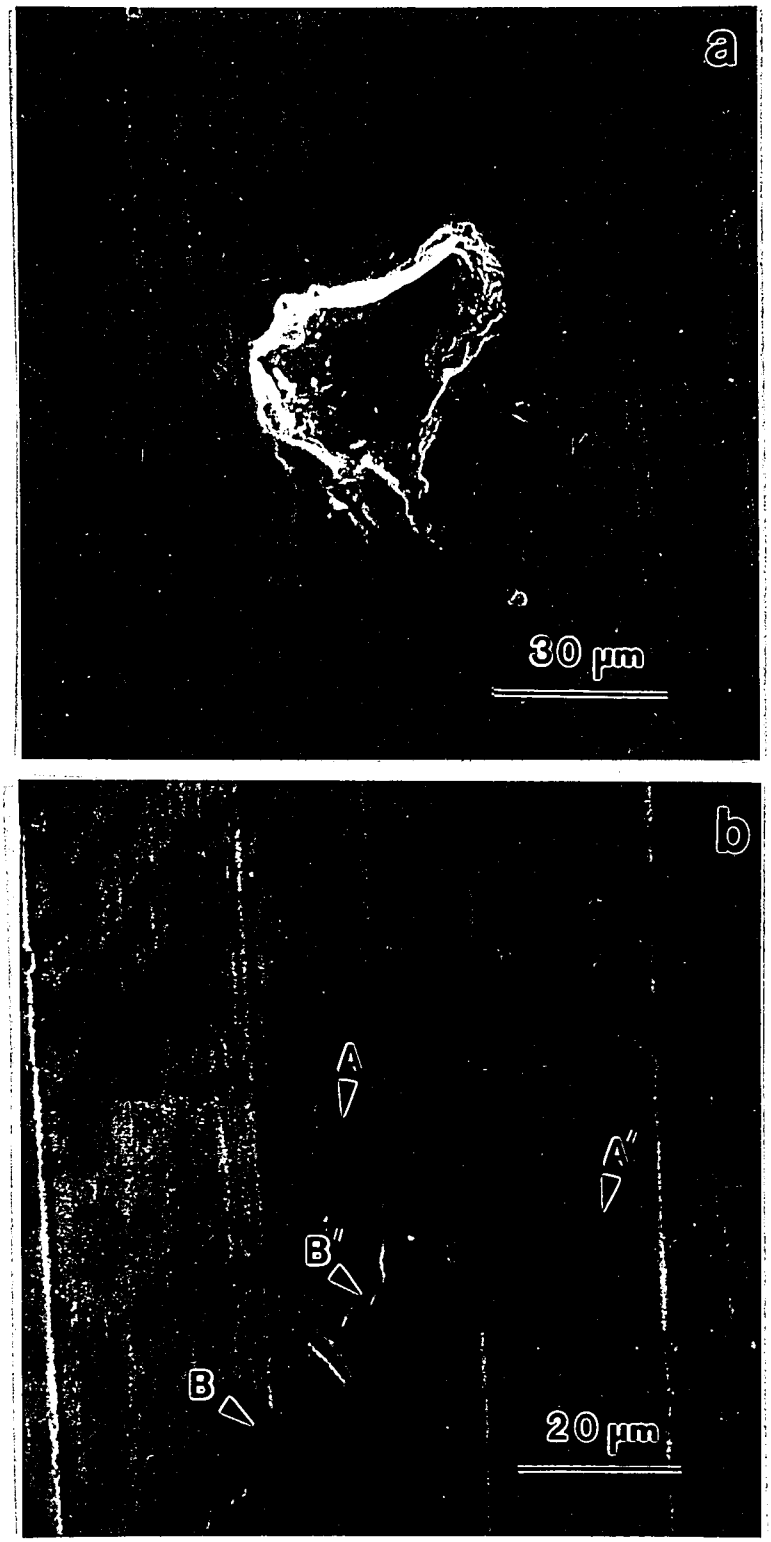

Figure 3.22: SEM image of (a) grain attack and (b) surface cracks on a specimen thermally cycled between 25 and 550°C. Test duration: 3,000 cycles with no failure.

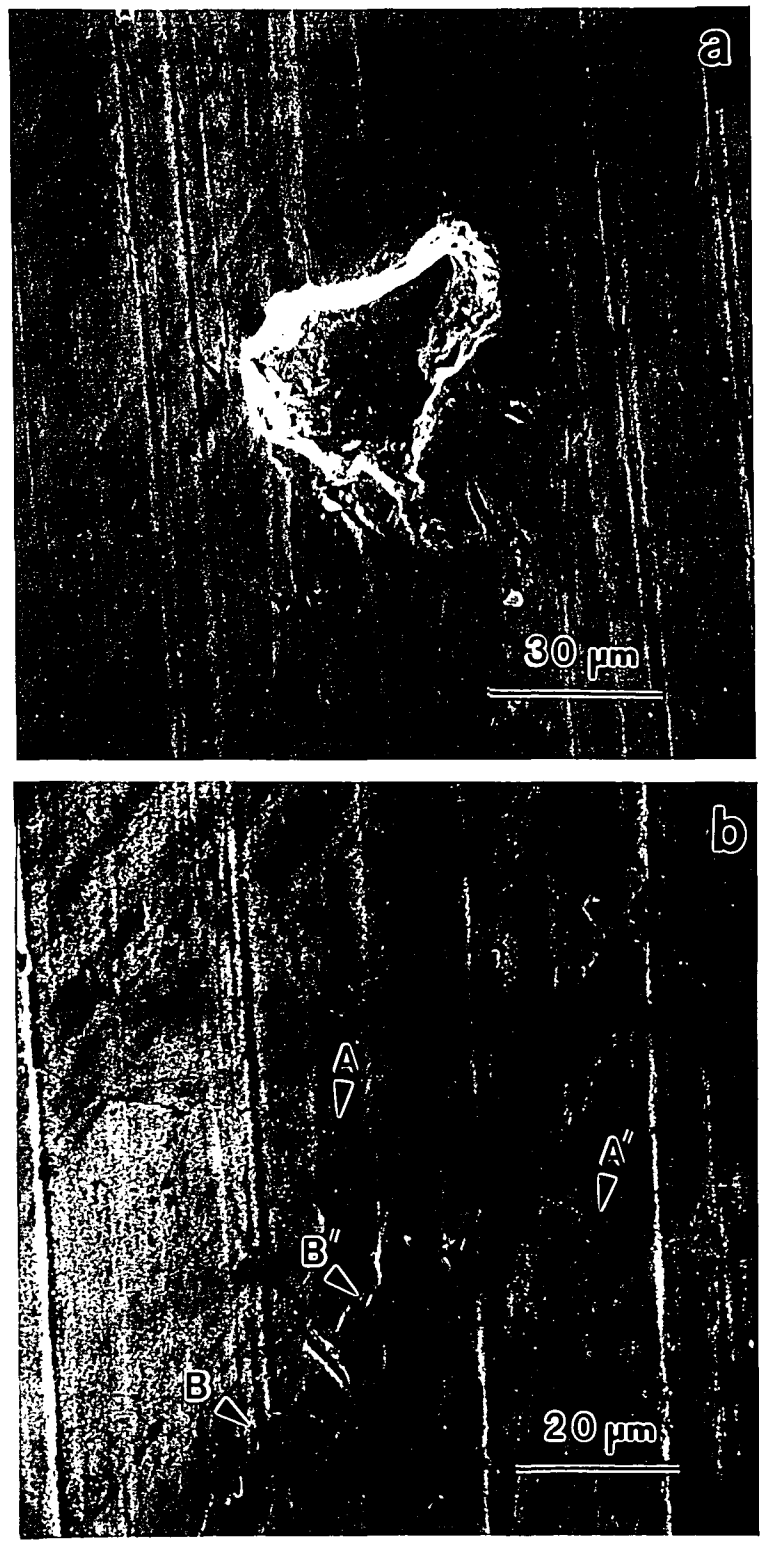

Figure 3.22: SEM image of (a) grain attack and (b) surface cracks on a specimen thermally cycled between 25 and 550°C. Test duration: 3,000 cycles with no failure.

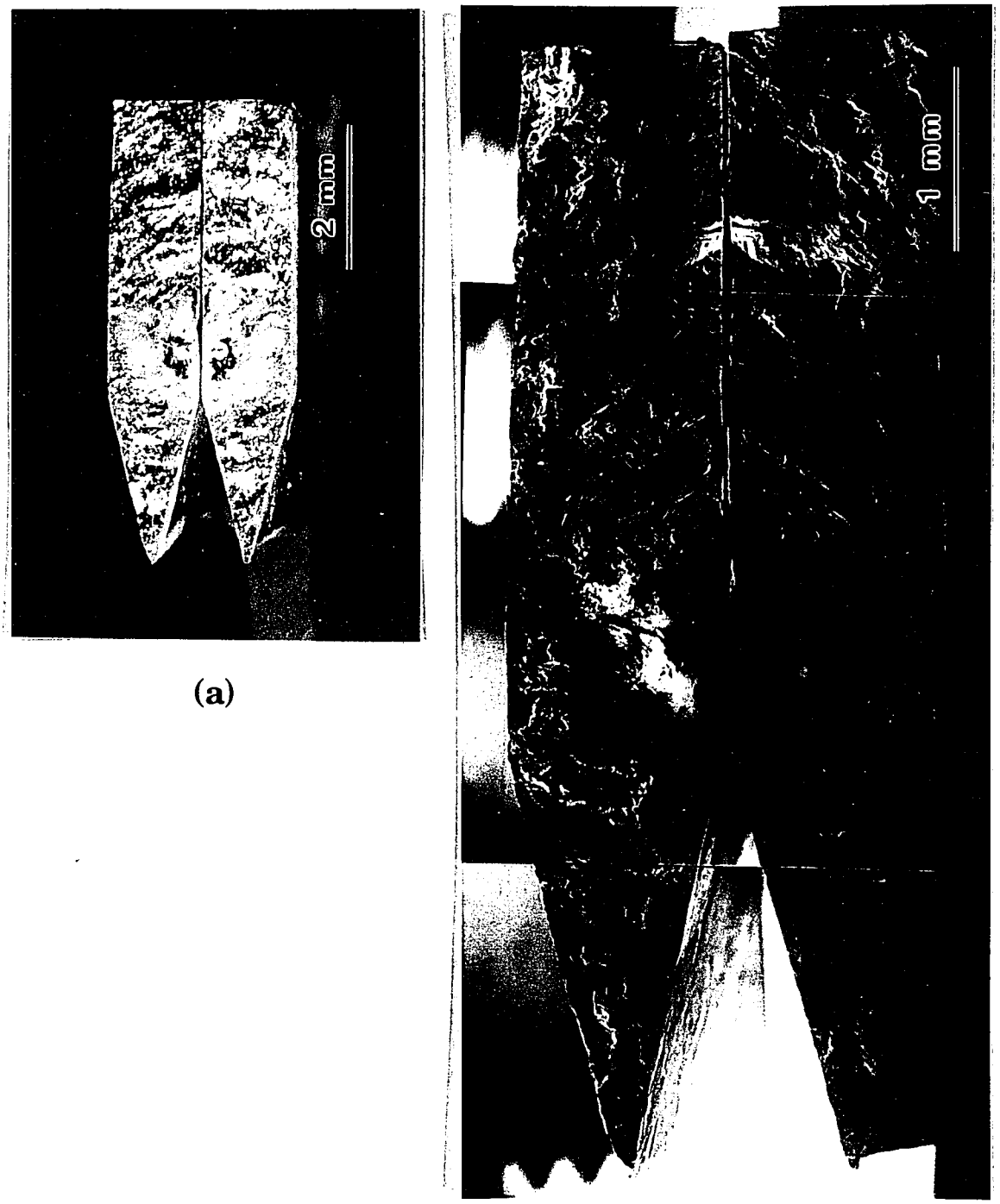

Figure 3.23: (a) Optical and (b) SEM micrographs of mating fracture surfaces of a specimen thermally cycled in air from 25 to 900°C. Lifetime: 2,782 cycles.

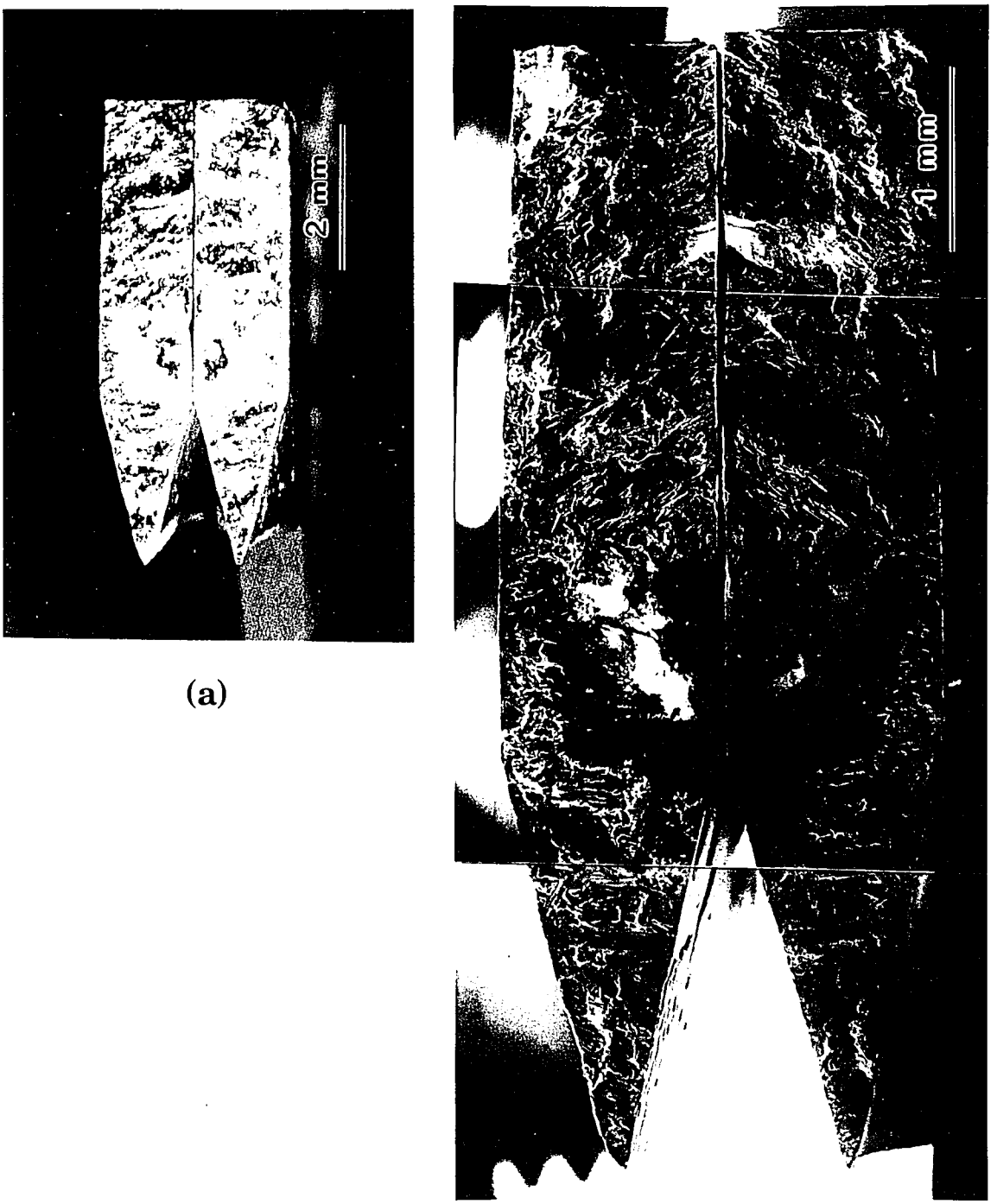

Figure 3.23: (a) Optical and (b) SEM micrographs of mating fracture surfaces of a specimen thermally cycled in air from 25 to 900°C. Lifetime: 2,782 cycles.

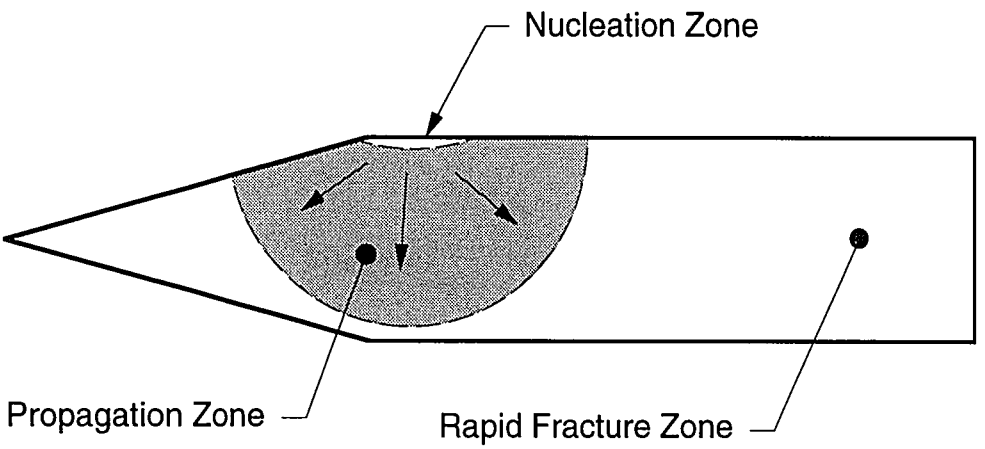

Figure 3.24: Diagram illustrating the three-zone fracture surface morphology of specimens thermally cycled in air to 900°C.

Figure 3.25: SEM image of mating fracture surfaces of a specimen thermally cycled in air from 25 to 900°C showing the nucleation and propagation zone. Lifetime: 2,782 cycles.

Figure 3.25: SEM image of mating fracture surfaces of a specimen thermally cycled in air from 25 to 900°C showing the nucleation and propagation zone. Lifetime: 2,782 cycles.

Figure 3.26: SEM image of the nucleation and propagation zone of a specimen thermally cycled in air from 25 to 900°C. Lifetime: 2,782 cycles.

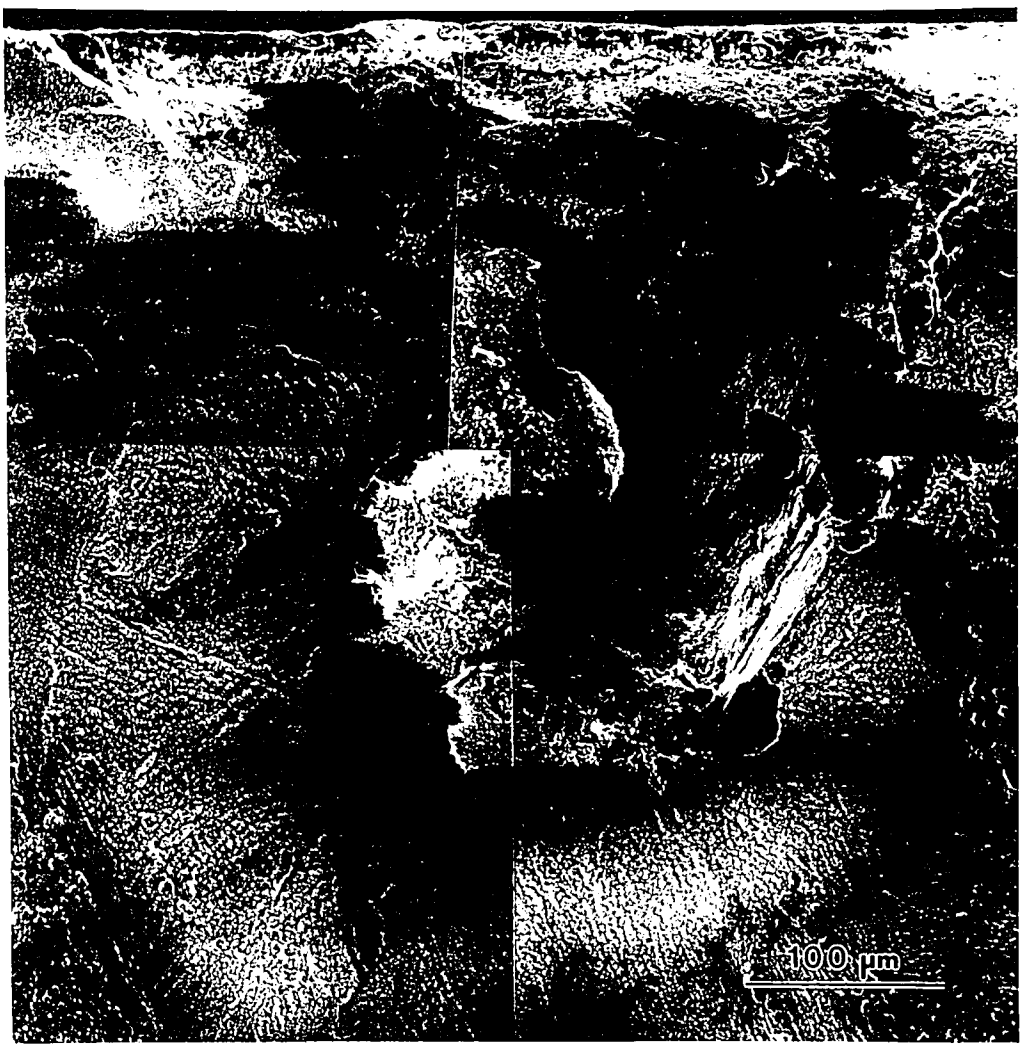

Figure 3.26: SEM image of the nucleation and propagation zone of a specimen thermally cycled in air from 25 to 900°C. Lifetime: 2,782 cycles.

Figure 3.27: SEM image of mating fracture surfaces of a specimen thermally cycled in hydrogen from 25 to 900°C. Lifetime: 10 cycles.

Figure 3.27: SEM image of mating fracture surfaces of a specimen thermally cycled in hydrogen from 25 to 900°C. Lifetime: 10 cycles.

Figure 3.28: SEM fractographs of fracture surfaces produced in hydrogen, showing (a) interlamellar facets and translamellar cracking markings, and (b) cleavage facets and grain boundary separation markings.

Figure 3.28: SEM fractographs of fracture surfaces produced in hydrogen, showing (a) interlamellar facets and translamellar cracking markings, and (b) cleavage facets and grain boundary separation markings.

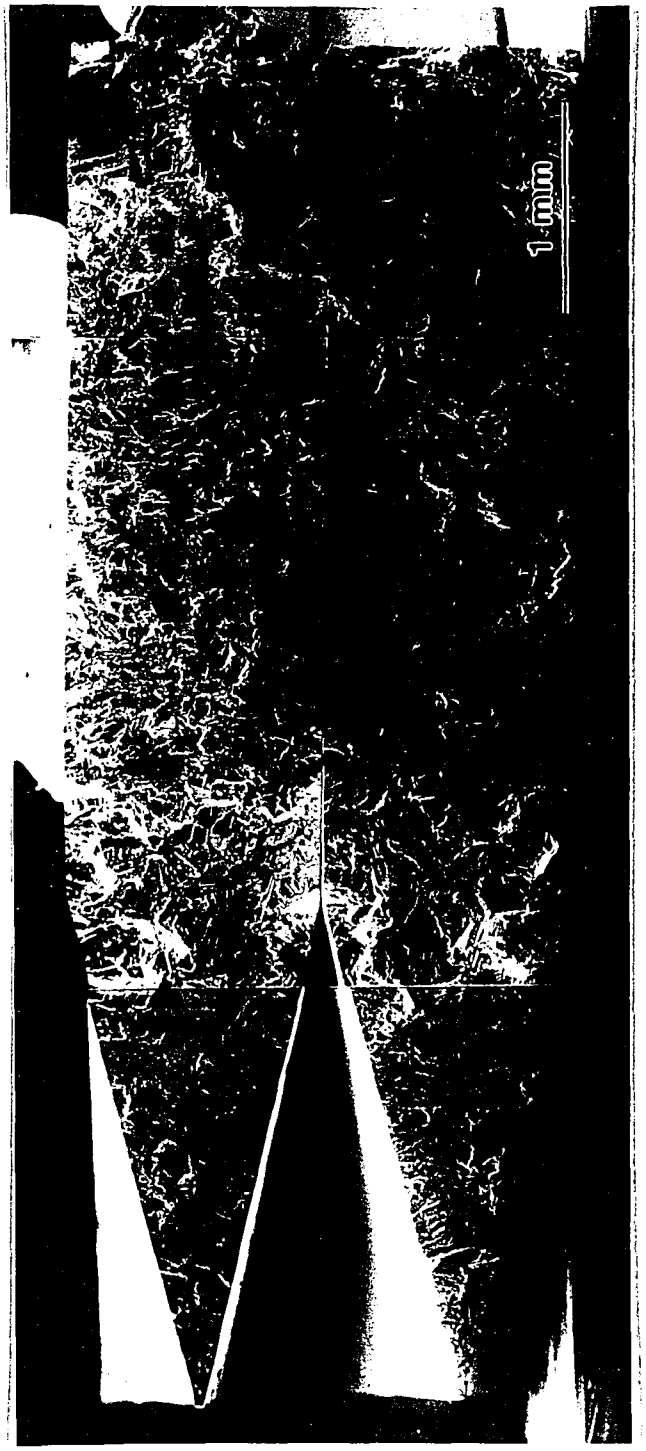

Figure 3.29: SEM image of mating fracture surfaces of a specimen thermally cycled in hydrogen from 25 to 750°C. Lifetime: 46 cycles.

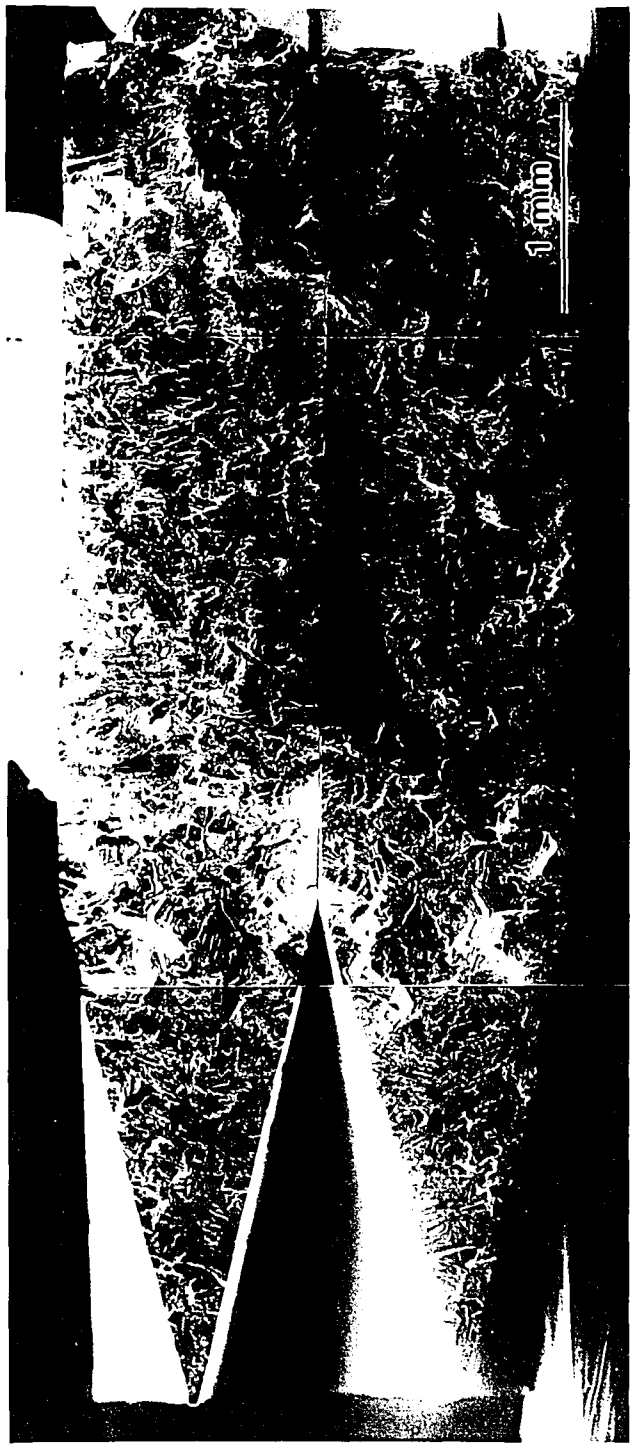

Figure 3.29: SEM image of mating fracture surfaces of a specimen thermally cycled in hydrogen from 25 to 750°C. Lifetime: 46 cycles.

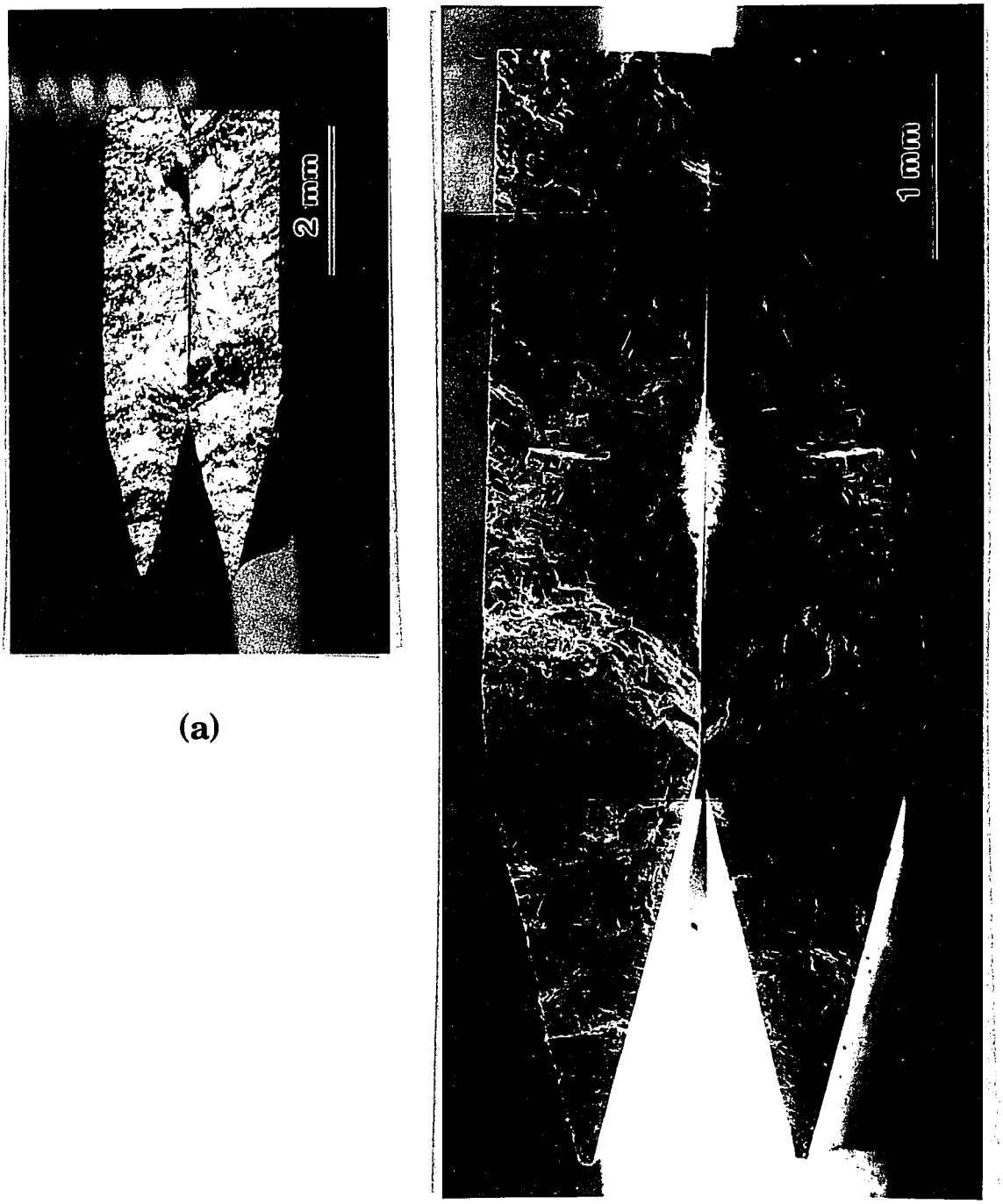

Figure 3.30: (a) Optical and (b) SEM micrographs of mating fracture surfaces of a specimen thermally cycled in hydrogen from 25 to 750°C. Lifetime: 1,828 cycles.

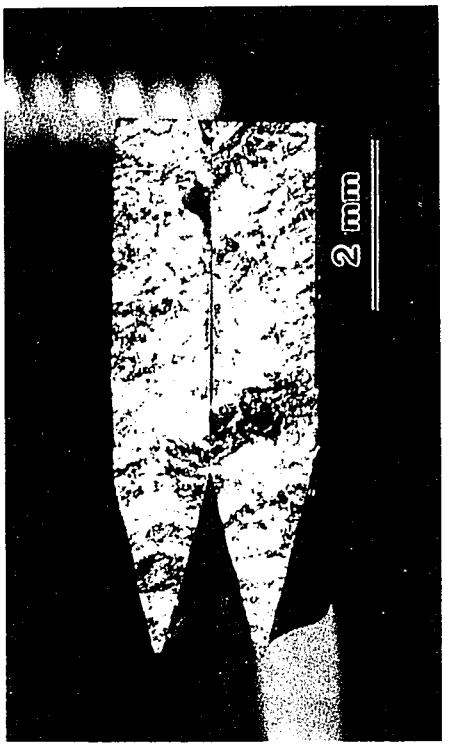

(a)

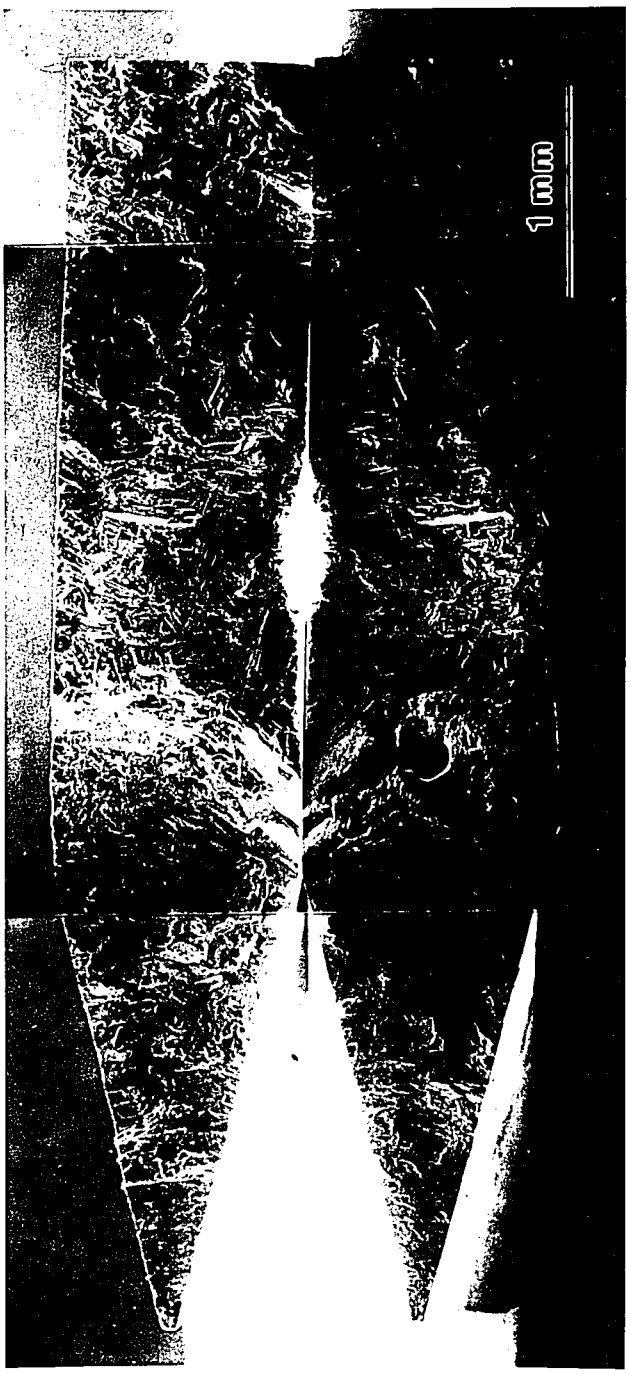

(b)

Figure 3.30: (a) Optical and (b) SEM micrographs of mating fracture surfaces of a specimen thermally cycled in hydrogen from 25 to 750°C. Lifetime: 1,828 cycles.

Figure 3.31: SEM image of a portion of the propagation zone on the fracture surface produced during thermal cycling in hydrogen from 25 to 750°C. (A) Nucleation zone near the specimen surface. (B) Oxidation on the propagation zone surface. Lifetime: 1,828 cycles.

REFERENCES

1. H. A. Lipsitt, "Titanium Aluminides - An Overview", Proceedings of Materials Research Society Symposium on High Temperature Ordered Intermetallic Alloys, 39 (1985), 351-364.

2. F. H. Froes et al., "Review of Synthesis, Properties, and Applications of Titanium Aluminides", Journal of Materials Science, 27 (19) (1992), 5113-5134.

3. Y-W. Kim, "Intermetallic Alloys Based on Gamma Titanium Aluminide", Journal of Metals, 41.7 (1989), 24-30.

4. K. S. Chan and Y-W. Kim, "Influence of Microstructure on Crack Tip Micromechanisms and Fracture Behavior of a Two-Phase TiAl Alloy", Metallurgical Transactions, 23A (1992), 1663-1677.

5. M. Nakamura, K. Hashimoto, and T. Tsujimoto, "Environmental Effect on Mechanical Properties on TiAl base Alloys", Journal of Materials Research, 8 (1) (1993), 68-77.

6. K. S. Chan and Y-W. Kim, "Rate and Environmental Effects on Fracture of a Two-Phase TiAl Alloy", Metallurgical Transactions, 24A (1993), 113-125.

7. C. T. Liu and Y-W. Kim, "Room-Temperature Environmental Embrittlement in a TiAl Alloy", Scripta Metallurgica et Materialia, 27 (1992), 599-603.

8. T. Takasugi et al., "Environmental Embrittlement of Gamma Titanium Aluminide", Journal of Materials Research, 7 (1992), 2739-2745.

9. M. Gao, J. Boodey, R. P. Wei, W. Wei, "Hydrogen Solubility and Microstructure of Gamma Based Titanium Aluminides", Scripta Metallurgica et Materialia, 27 (1992), 1419-1423.

10. D. A. Spera, "What is Thermal Fatigue?", Thermal Fatigue of Materials and Components, ASTM STP 612, 1976, 3-9.

11. M. J. Blackburn, M. P. Smith, and J. T. Hill, "R&D on Composition and Processing of Titanium Aluminide Alloys for Turbine Engines", Final Technical Report AFWAL-TR-84-4078, AFWAL/MLLM, WPAFB, OH 45433, 1984.

12. S. Venkatataman, "Elevated Temperature Crack Growth Studies of Advanced Titanium Aluminides", Final Report AFWAL-TR-87-4103, AFWAL/MLLM, WPAFB, OH 45433, 1987.

13. J. J. Pernot, "Thermal-Mechanical Fatigue Testing of a Titanium-Aluminide Alloy", Master of Science Thesis, Air University, 1987.

14. A. Weronski and T. Hejwowski, Thermal Fatigue of Metals, New York: Marcel Dekker, Inc., 1991.

15. N. Stoloff, M. Shea, and A. Castagna, "Hydrogen Embrittlement of Intermetallic Compounds and Their Composites", Environmental Effects on Advanced Materials, Warrendale, PA: TMS, 1991, 3-19.

16. Y-W. Kim, "Microstructural Evolution and Mechanical Properties of a Forged Gamma Titanium Aluminide Alloy", Acta Metallurgica et Materialia, 40.6 (1992) 1121-1134.

17. T. Hino, H. Okada, and M. Kanno, "Analysis of Hydrogen Evolved form Fracture Surfaces of a TiAl Alloy", Scripta Metallurgica et Materialia, 29 (1993), 1029-1033.

18. W. O. Soboyejo and K. Lou, "Grain Boundary Segregation and Intergranular Fracture in a Gamma-Based Titanium Aluminide Intermetallic", Scripta Metallurgica et Materialia, 29 (1993), 1335-1339.

19. Y. Umakoshi et. al., "Oxidation Resistance of Intermetallic Compounds Al_3Ti and TiAl", Journal of Materials Science, 24 (1989), 1599-1603.

20. R. P. Wei and M. Gao. "Hydrogen Embrittlement and Environmentally Assisted Crack Growth", Hydrogen Effects on Material Behavior, Warrendale, PA: The Metallurgical Society, 1990, 789-815.

21. F. P. Incropera and D. P. DeWitt, Fundamentals of Heat and Mass Transfer, 3rd ed., New York: John Wiley & Sons, 1981.

22. J. E. Shigley and C. R. Mischke, Mechanical Engineering Design, 5th ed., New York: McGraw-Hill, 1989.

23. R. Weast, et al., eds. CRC Handbook of Chemistry and Physics, 66th ed., Boca Raton: CRC Press, 1985.

24. D. S. Shih, G. K. Scarr, and G. E. Wasielewski, "On Hydrogen Behavior in Ti_3Al", Scripta Metallurgica et Materialia, 23 (1989), 973-978.

25. D. Legzdina et. al., "Hydride Structure in Titanium Aluminides Subject to High Temperature and Hydrogen Pressure Charging Conditions", Journal of Materials Research, 6 (1991), 1230-1237.

26. J. B. Boodey, M. Gao and R. P. Wei, "Hydrogen Solubility and Hydride Formation in a Thermally Charged Gamma-Based Titanium Aluminide", Environmental Effects on Advanced Materials, Warrendale, PA: TMS, 1991, 57-65.

APPENDIX A

PROCEDURES

A-1.1 ASSEMBLY PROCEDURE

A-1.1.1 Specimen Preparation

1. Polish specimen knife edge with 6 μm diamond paste to remove defects and smooth machining marks.

2. Polish specimen surface with 600 grade SiC emery paper. Place all scratches in the long direction by only polishing lengthwise.

3. Remove EDM residue at T-C weld location with emery paper.

4. Measure specimen dimensions and record on specimen report form.

5. Examine specimen surface and knife edge for defects with 50x microscope. Record any defects (scratches not aligned with long axis, pits, etc.) on report form. Specimen must be discarded if any extremely large defects or cracks are found.

6. Clean specimen ultrasonically in acetone and methanol, 15 min. each. Handle specimen only with rubber gloves from this point on.

A-1.1.2 Spot Welding The Thermocouple

7. Clean the inside of the three unassembled chamber flanges (front and side flanges) with acetone.

8. Inspect K thermocouple wires. They should be fed through swage-lock nut and Teflon plug on the exhaust flange. Teflon tubing should cover the wires from the fitting to the inside of the flange, where a 25 mm long ceramic sheath should cover them.

9. Twist ends of thermocouple wires together (no more than two twists), and bend the twist 90°.

10. Spot weld the thermocouple wire to the center of the rear edge of the specimen (opposite the knife edge), with wires leading away from the knife edge. Bend should be to rear of specimen so T-C does not interfere with insertion of grip plate.

Spot Welder Settings: 20 lb (90 N), 0.30 A

A-1.1.3 Mounting the Specimen

11. Check grip/chamber alignment using inspection mirror, feeler gauges, continuity tester.

12. Lower the bottom grip.

13. Raise chamber.

14. Check that the lower grip plate is in place.

15. Put new copper seal on exhaust side flange.

16. Carefully tilt specimen/flange assembly and insert the specimen into the bottom grip slot. Avoid bending, jarring, or twisting the thermocouple wire. Once the specimen is in the lower grip, tilt it upwards until it is completely within the chamber. Be sure the exhaust pipe is behind the power lines, i.e., outside the loop, to avoid induction effects.

17. Raise lower grip back to the approximate operating height.

18. Lower chamber to insert lower pin and set screw. Only tighten enough to keep specimen from falling freely.

19. Raise chamber to insert upper pin and set screw (Do not insert yet). Align pin holes of specimen and grip.

20. Backside of specimen should just rest against backside of grip. Make adjustments to upper grip position, rotation, chamber tilt, etc. as necessary. Reflect a light through the slot from the other side to improve visibility.

21. Insert upper grip plate, set screw and pin. Make adjustments to lower grip height as necessary.

22. Tighten upper grip. Specimen should not move as screw is tightened. If it does, go back to step 20.

23. Lower chamber and tighten lower grip.

24. Return chamber to center position and tighten chamber mounting plate nuts. Use the bubble level to verify that the mounting plate is level.

25. Tighten thermocouple seal on exhaust.

26. Tighten exhaust flange bolts.

27. Attach flange with inlet gas line. Be sure to use a new copper gasket.

28. Attach front window flange. Be sure to use a new copper gasket.

29. Check chamber alignment again continuity tester. There should be no continuity between chamber and the grips. If there is, loosen chamber mounts and tilt chamber until continuity is lost.

30. Tighten o-ring clamps at the top and the bottom of the chamber around the grips.

31. Repeat continuity check (step 29).

32. Tighten chamber mounting bolts.

33. Repeat continuity check (step 29). If continuity exists, loosen bolts and O-rings and return to step 29.

34. Attach exhaust line.

35. Repeat continuity check (step 29). If continuity exists, loosen bolts and O-rings and return to step 29.

A-1.2 Test Procedure

1. Post the 'Test in Progress' and 'Cooling Water in Use' signs. Place barriers and warning tape if H_2 is in use. Also remove all items from hood if H_2 is in use.

2. Verify water cooling lines are in place.

3. **Air:** Fill dewar with ethyl alcohol/dry ice mixture (-83° C, for Air testing)

4. **Air:** Insert cooling coil into dewar

A-1.2.1 H_2: Leak Test / Argon Flush (Hydrogen Testing Only)

5. Plug end of 1/4" (12 mm) gas line for leak test.

6. Open valve to argon cylinder and adjoining valves to system gas lines. Pressurize to 15 psig (100 kPa).

7. Using soap solution, check all joints for leaks.

8. Close valve to cylinder, unplug gas line and connect to chamber inlet line.

9. Open valve to argon cylinder and adjoining valves to system gas lines.

10. Unplug solenoid valve from controller and plug into wall outlet.

11. Set inlet pressure to 15 psig (100 kPa) when gas is flowing.

12. Leak test remaining portion of system with soap solution.

13. Argon flush can be stopped after 10 minutes of continuous flow with system sealed and leak-tight. To stop, close argon cylinder valve, and with remaining valves open, allow manifold pressure to fall to 200-300 psig (140-210 kPa). Close solenoid by unplugging it.

A-1.2.2 Prepare System

14. Turn on cooling water to flow rate of 3L/min (500 mL/ 10 sec) to allow grips to begin to cool.

15. Cover fittings with insulation on chamber inlet side.

16. Plug thermocouple into compensator, which is plugged into the black pen on the chart recorder.

17. Plug load cell into red pen of chart recorder and to DVM set to 20 VDC range.

18. Switch on constant voltage transformer, controller, amplifier, chart recorder, and T-C compensator.

19. Set chart recorder black pen (temperature) to 50 mV range (0.5mV per division) and red pen (load) to 5V range (5 lbs per division).

20. Set chart speed to 10 mm per minute.

21. Zero pens on chart recorder.

22. Record scale (Load, max temp) on chart along with date/time, specimen #, atmosphere, max temp.

23. Adjust telescope and light to bring specimen knife edge into focus.

A-1.2.3 Test Gas Flush

24. Open cylinder #1 valve until maximum pressure is reached in the manifold, then close cylinder.

25. Plug solenoid into wall outlet.

26. Set output pressure to 15 psig (100 kPa) for Air, 4 psig (27 kPa) for Helium, and 3 psig (20 kPa) for Hydrogen.

27. When inlet pressure to regulator drops to zero, open cylinder again until maximum pressure is reached in the manifold.

    H_2: For hydrogen, only allow the gas to flow for approximately 10 seconds. Then unplug solenoid, wait 10 seconds, and plug solenoid back in. This reduces the amount of a hydrogen in the hood exhaust system over time.

28. Stop flushing when 5 cycles of opening and closing the cylinder valve are complete.

29. **H_2/He:** Lift dewar from floor so that cooling coil slides inside, and then slide table support underneath.

30. **H_2/He:** Fill dewar with LN_2 (-190°C, for H_2 or He testing) so that coil is completely immersed

31. Perform five more flushes now that coil is immersed in dewar.

A-1.2.4 Start Test

32. Post IN USE sign on cylinder #1.

33. Open valve to cylinder #1.

34. Plug solenoid back into controller.

35. Reset counter.

36. Set *Heat High* and *Heat Low* variable transformers to about 21.5 % for 900°C, and to about 20% for 750°C.

37. Set all timers to 10 seconds.

38. Apply Preload of 350 lbs (1560 N). Be sure to lock the nuts (top and bottom).

39. Start chart recorder.

40. Switch controller to *system on*.

41. Switch controller to *operate*.

42. Adjust max. temp as required.

43. Adjust load back to 350 lbs (1560 N) as required during first ten minutes of testing (first 20 cycles)

A-1.2.5 Monitor Test

44. During duration of test, adjust max. temp if outside ± 10°C (± 1.5 divisions).

45. Periodically check water flow rate and adjust if necessary.

46. Monitor coolant. Add dry ice or LN_2 when necessary.

47. Switch gas cylinders when cylinder #1 runs low. Be sure to close valve on cylinder #1 before opening cylinder #2. Move IN USE sign to cylinder #2.

48. If chart recorder paper runs low, switch paper. Be sure to re-zero the pens. Replace pens when necessary.

49. Monitor specimen surface with telescope for crack initiation and growth. Record location, time of initiation (detection), and length in log book and on strip chart. Record growth rate over specific intervals.

A-1.2.6 EMERGENCY HYDROGEN SHUTDOWN PROCEDURE

Perform as much or as little of this procedure as deemed safe — However, step 1 is absolutely necessary!!!

1. Close cylinder valve on hydrogen cylinder which is IN USE.

2. Press *Operate* to stop test.

OR

Turn off variable transformer to cut all power to controller.

3. Flush with argon:
    - lower dewar to remove cooling coil.
    - open argon cylinder valve
    - plug solenoid into wall outlet
4. Evacuate the lab.

A-1.3 SHUTDOWN / DISASSEMBLY PROCEDURE

A-1.3.1 Shutdown

1. When specimen fracture or the predetermined number of cycles is reached and the specimen is at the end of the cool down phase, press the *operate* button. Then press *system off*. (*system off* must be depressed for about 1 second).
2. Release the load on test specimen by loosening lower grip nuts.
3. Close cylinder valves.
4. Stop chart recorder paper.
5. Turn off cooling water.
6. **Air**: Disconnect gas cooling coil from gas lines and remove coil from dewar.
7. **H_2/He:** Remove coil from dewar (lower dewar while supporting piping).
8. **H_2**: Unplug the solenoid valve from the controller and plug into the wall outlet. Allow manifold pressure to drop to 200-300 psig (140-210 kPa). Unplug valve to close valve.
9. **H_2**: Open valve to argon cylinder and pressurize manifold to the maximum pressure. Close valve.
10. **H_2**: Plug solenoid back into wall outlet. Set pressure to 15 psig (100 kPa). When argon manifold pressure drops to near zero,

repressurize to the maximum pressure. Repeat 5 times, and then leave argon valve open and flush for 10 minutes.

11. **H_2**: When argon flush is complete, close argon cylinder valve, and allow manifold pressure to drop to zero.

12. Turn off controller, load cell amplifier, constant voltage transformer, and chart recorder and T-C compensator.

13. Put caps on recorder pens and cover chart recorder.

A-1.3.2 Disassembly

14. Remove front and gas inlet flanges from chamber. Wrap in foil.

15. Disconnect exhaust pipe.

16. Loosen O-ring seals.

17. Unplug thermocouple from compensator.

18. Raise and lower chamber to remove set screws and pins from specimen. If specimen is fractured, be sure not to drop or damage the fracture surface.

19. Remove gas exhaust flange, being careful not to tug hard on specimen. If specimen is still attached to thermocouple, carefully tilt and remove specimen. Lower bottom grip if necessary. Use gloves to handle specimen.

20 Remove thermocouple from specimen (if necessary).

21. Put specimen in marked container.

22. Wrap exhaust flange and open chamber in foil.

23. Remove empty gas cylinders.

APPENDIX B

TEST SYSTEM CHARACTERISTICS

The following section describes the characteristics of the thermal fatigue test system developed here as determined by proof testing and observations during thermal fatigue testing.

B.1 THERMAL PROFILE

A proof test was conducted to determine the thermal profiles of the specimen during the heating, holding and cooling phases of the cycle. Naturally, since the specimen was heated by internal resistance and the grips were cooled, the temperature profile along the gauge length was not constant. Five K-type thermocouples (0.381 mm gauge chromel and alumel wire) were spot welded along the gauge length of the specimen on the edge opposite the knife edge. Thermocouple #3 was mounted in the center (comparable with a standard test), with two thermocouples spaced at 4 mm intervals on either side. The center thermocouple was used to set the temperature, again as is the case during standard testing. The test was conducted using helium as a test gas, although the specimen was also exposed to air since the front of the chamber had to be removed to allow access for all five thermocouples. An ice bath was used for the thermocouples' cold junction reference. The output of each thermocouple was recorded on one of three calibrated chart recorders set in the 50 mV range at a chart speed of 15 cm/min.

The cycling parameters chosen for the proof test were the same as those to be used later in actual testing, that is, a thirty second cycle period

with ten seconds for heating, ten for holding, and ten for cooling. The lower temperature in the cycle was always 25°C ± 10°C. Several different high temperatures were used, again those which would be used in later tests. These were 900°C, 750°C, 650°C, and 550°C.

The test system ran for over 150 cycles prior to recording any data to allow the grips and chamber to warm up to operating temperatures and the output to become stabilized.

Figure 2.7 shows the thermal profile along the gauge length of the specimen at both maximum and minimum temperatures for all four temperature ranges. Although the specimen is symmetrical, the temperatures on the upper portion are about 20 - 50°C hotter than the lower portion due to convection inside the chamber.

Figures B.1 - B.16 show the thermal profiles and respective heating and cooling rates of the upper half of the specimen during the entire cycle for the four temperature ranges. It should be noted that the cooling rates at the knife edge are significantly higher than those measured by the thermocouples at the rear of the specimen.

B.2 TEMPERATURE AND LOAD DRIFT

As stated earlier, the specimen maximum and minimum temperatures were adjusted whenever they drifted out of a ±10°C range. The load was not adjusted after twenty cycles.

Cycle to cycle temperature repeatability was excellent with any deviations usually below the resolution limits of the thermocouples. However, the temperature had a tendency to drift over the course of hours, especially during the first 1,000 cycles. During the first 1,000 cycles (and

after the initial 50 cycle stabilization phase), the drift rate during cycling to 900°C was typically up to 3°C/hr downwards. This drift was most likely caused by an increase in the resistance of the specimen. Later, typical drift rates were no more than 2°C/hr, and could be in either direction. Drift rates were lower at lower temperatures, but followed the same patterns.

The load on the specimen also tended to drift downward during testing, while the load range remained constant. Since all specimens were tested in a tension-tension condition, this load drift is probably due to relaxation and creep of the test specimens. A typical example of this load drift is shown in Figure B.17. Note that most of the drift occurs during the first 500 to 1000 cycles, reducing the maximum load from 1.57 kN to 1.37 kN by the $1{,}000^{th}$ cycle, with further reduction to 1.35 kN by the $4{,}500^{th}$ cycle. The minimum load follows the same pattern; however, the load range (i.e., maximum minus minimum) remains constant.

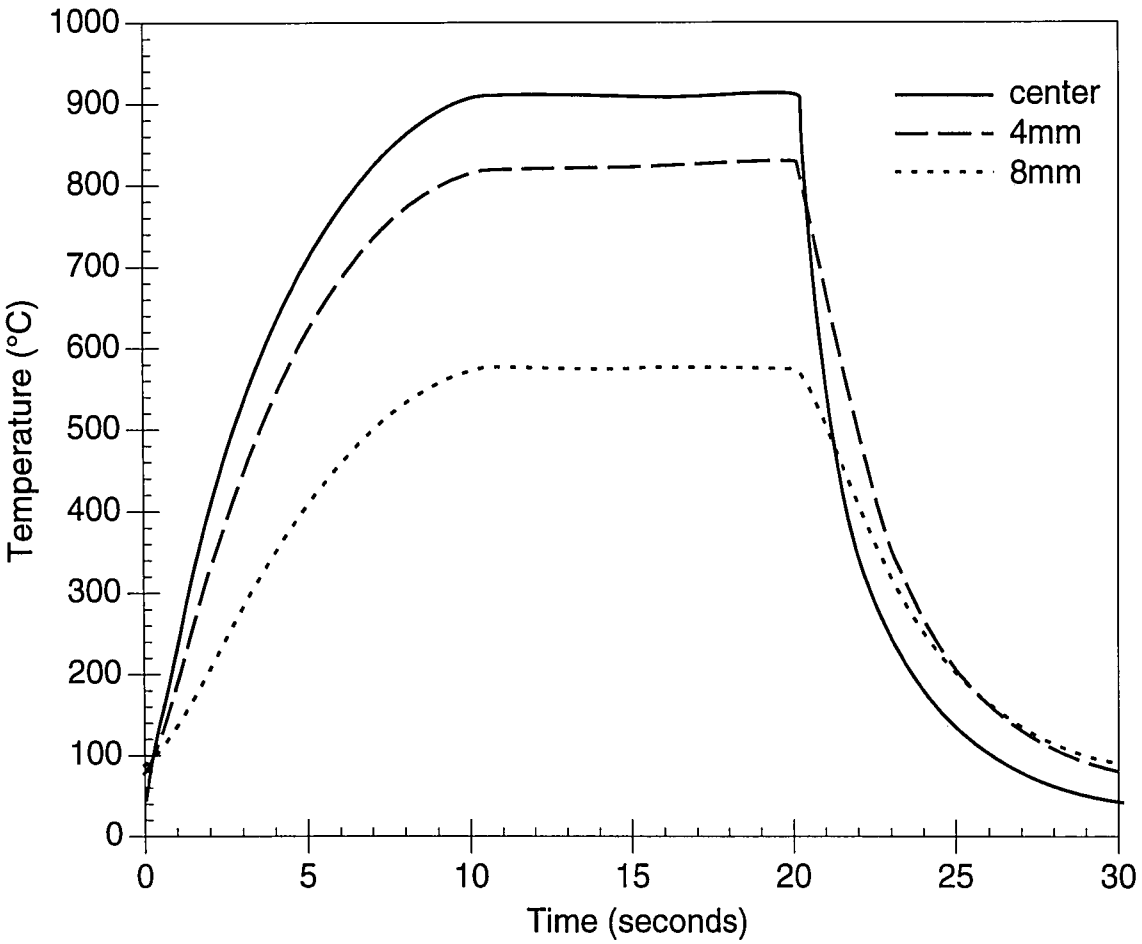

Figure B.1: Thermal cycle temperature profile during cycling between 25 and 900°C as measured by thermocouples located at 4 mm intervals above the center of the specimen (see Fig. 2.7). Accuracy: ± 2.2°C or 0.75%, whichever is greater.

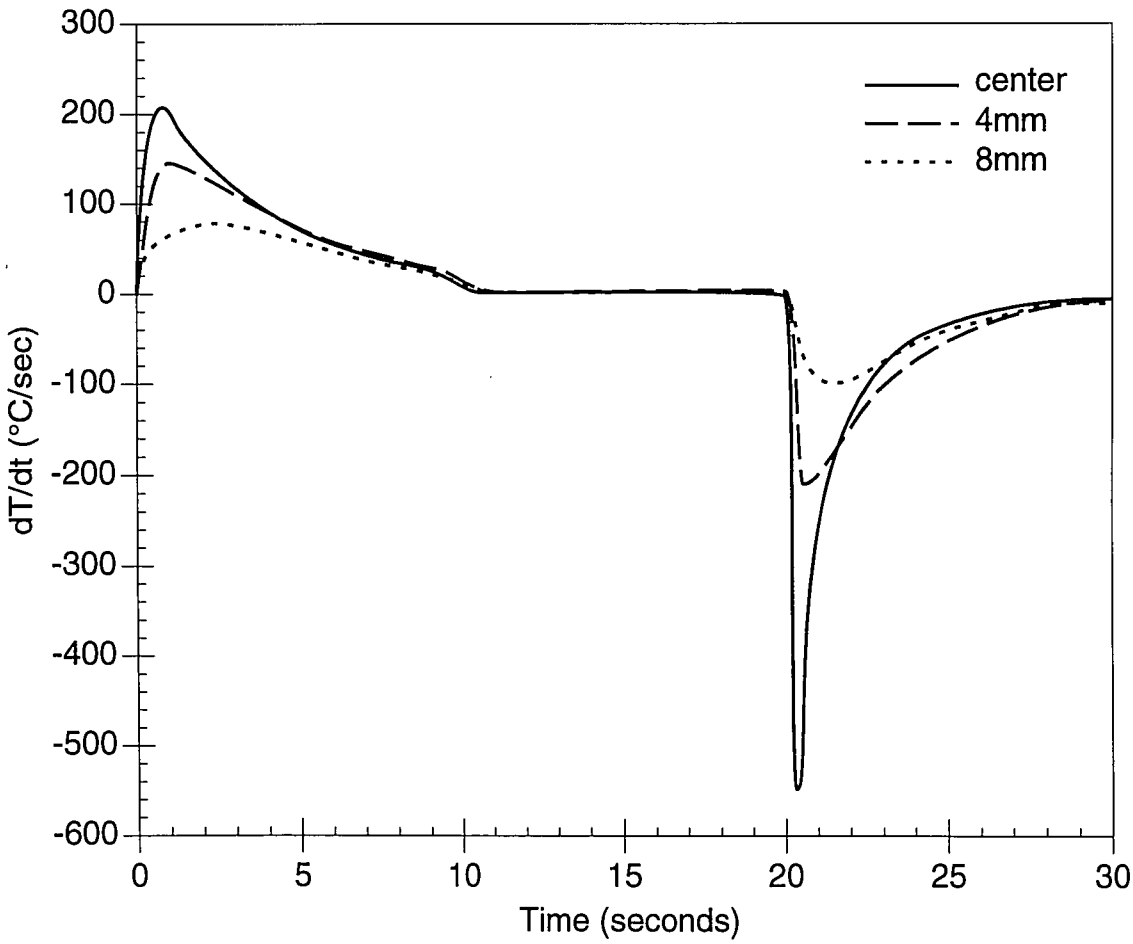

Figure B.2: Thermal cycle heating and cooling rates during cycling between 25 and 900°C as measured by thermocouples located at 4 mm intervals above the center of the specimen (see Fig. 2.7). Accuracy: ± 10°C/sec or 17%, whichever is greater.

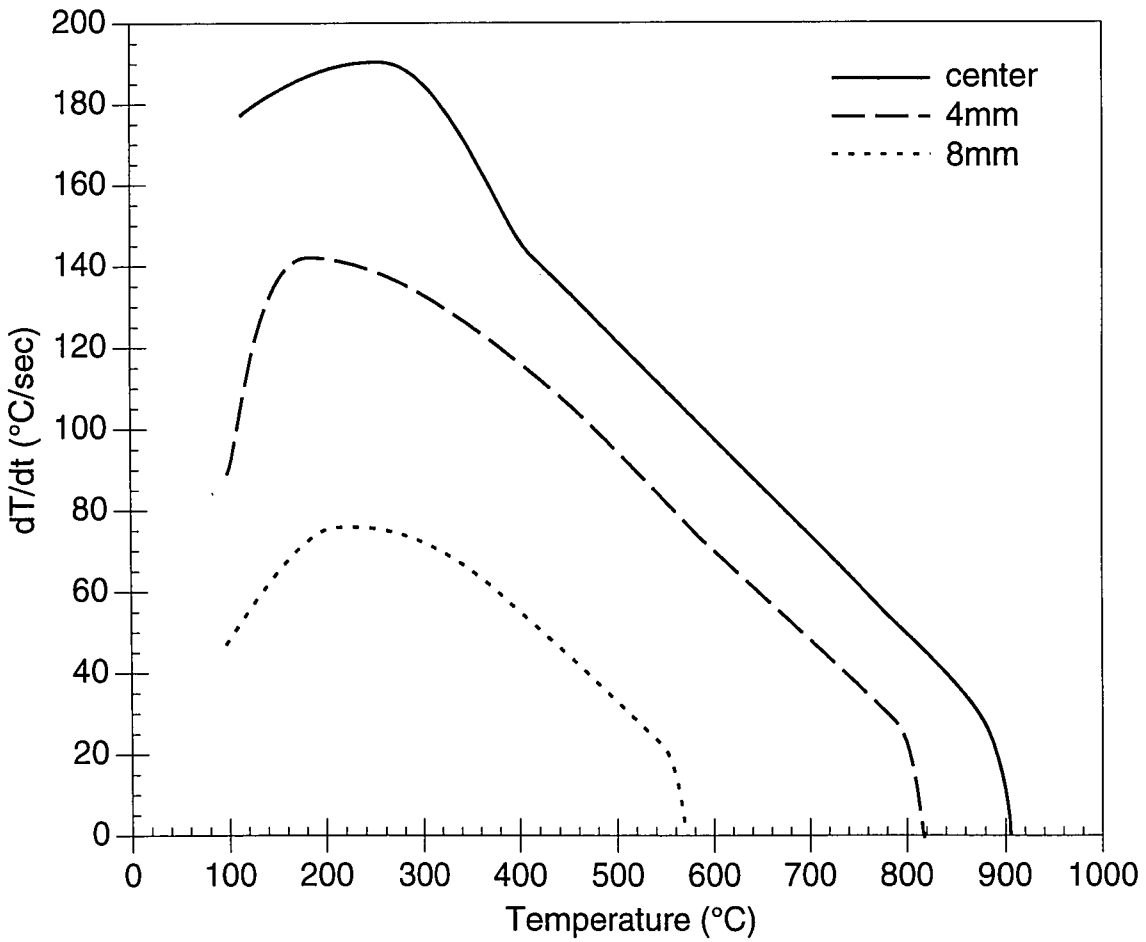

Figure B.3: Thermal cycle heating rate vs. temperature during heating from 25 to 900°C as measured by thermocouples located at 4 mm intervals above the center of the specimen (see Fig. 2.7). Accuracy: ± 10°C/sec or 17%, whichever is greater.

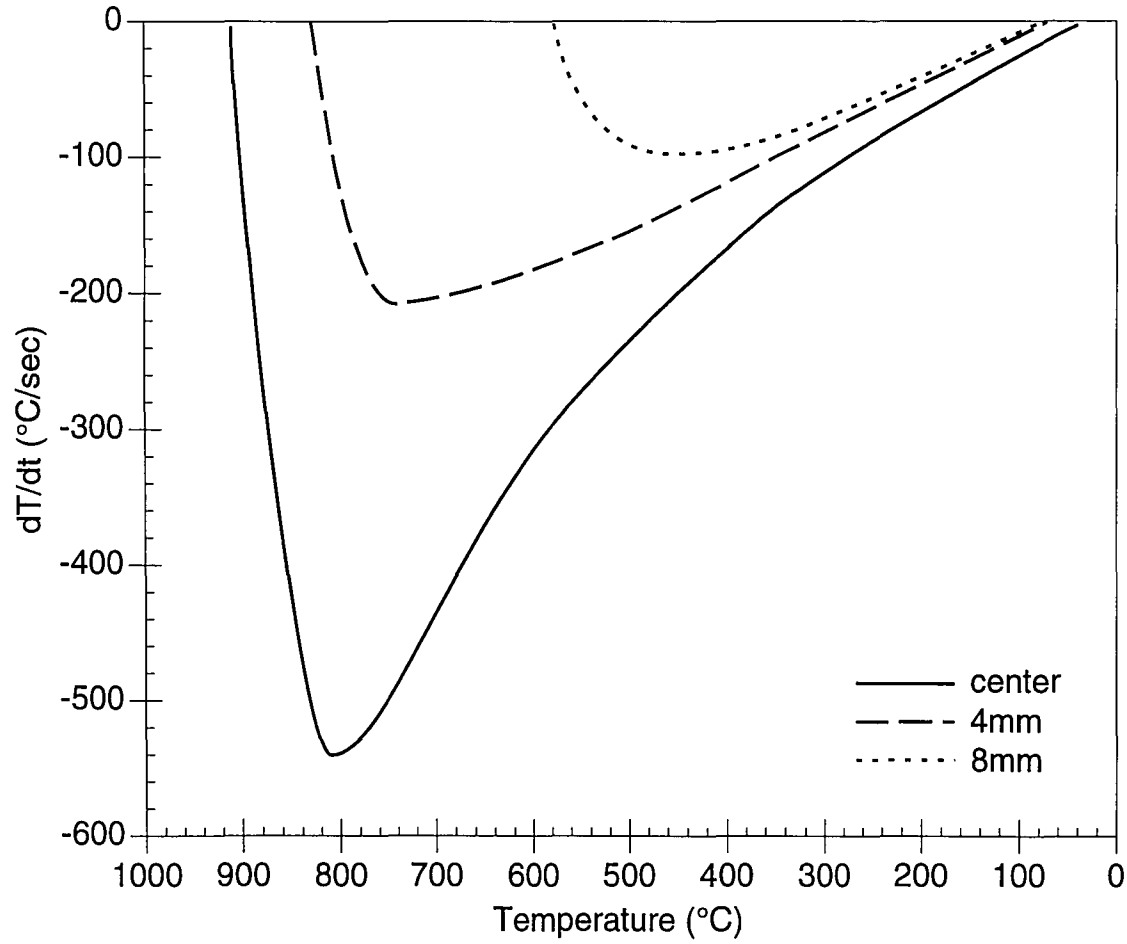

Figure B.4: Thermal cycle cooling rate vs. temperature during cooling from 900 to 25°C as measured by thermocouples located at 4 mm intervals above the center of the specimen (see Fig. 2.7). Accuracy: ± 10°C/sec or 17%, whichever is greater.

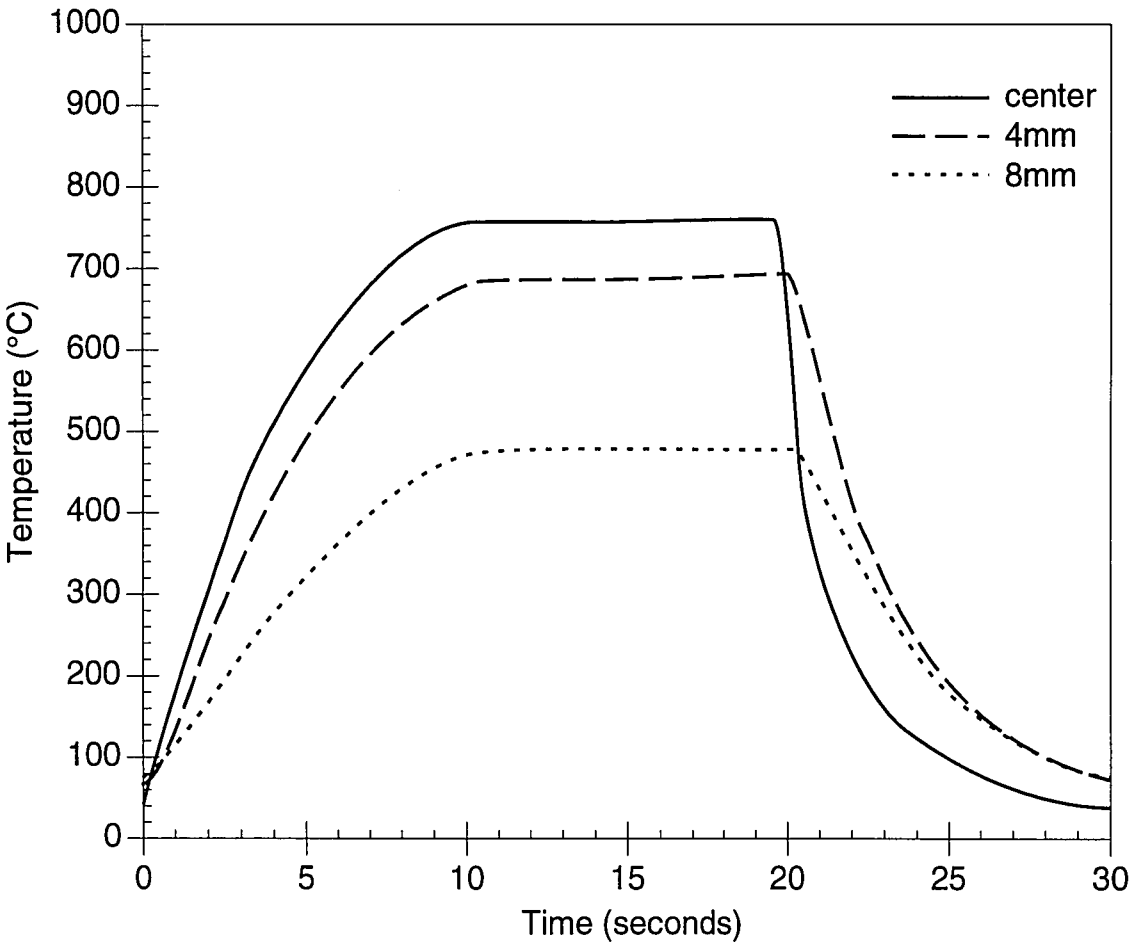

Figure B.5: Thermal cycle temperature profile during cycling between 25 and 750°C as measured by thermocouples located at 4 mm intervals above the center of the specimen (see Fig. 2.7). Accuracy: ± 2.2°C or 0.75%, whichever is greater.

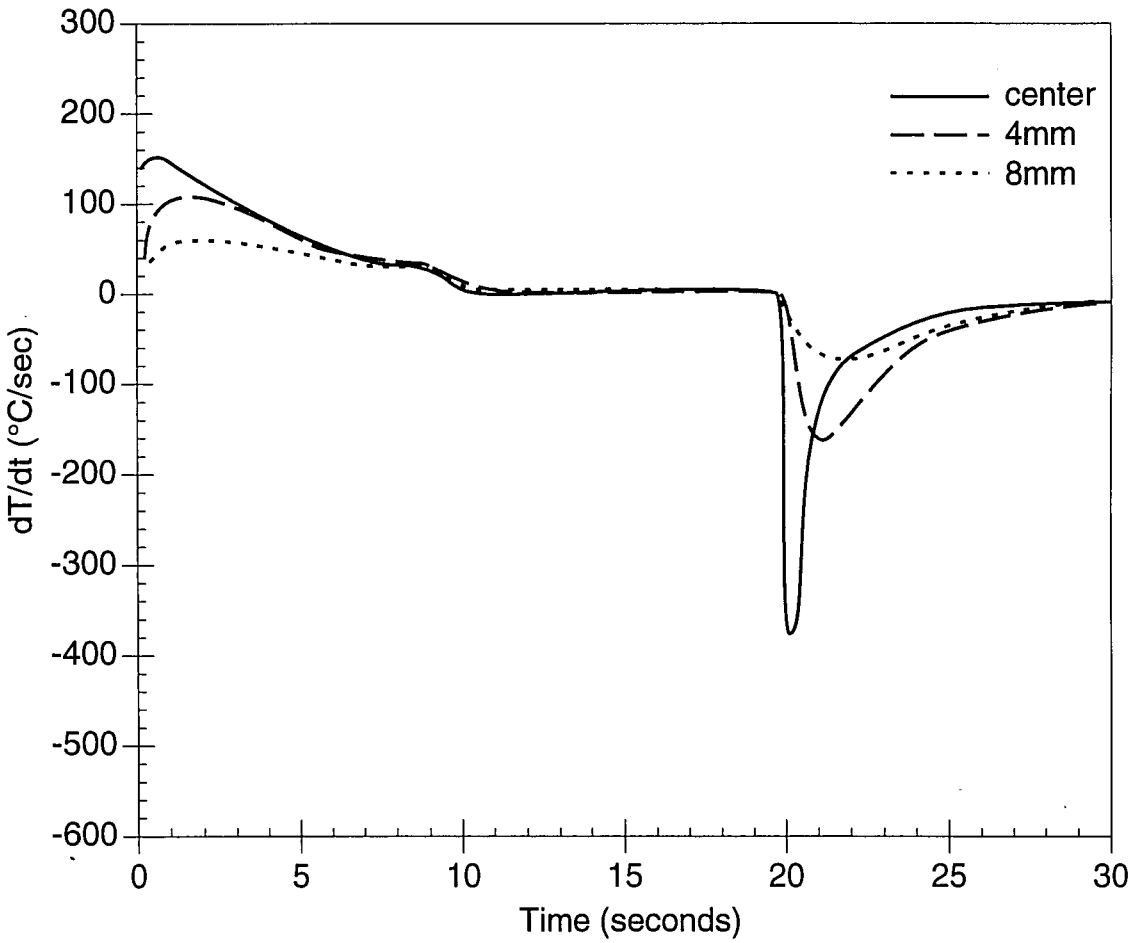

Figure B.6: Thermal cycle heating and cooling rates during cycling between 25 and 750°C as measured by thermocouples located at 4 mm intervals above the center of the specimen (see Fig. 2.7). Accuracy: ± 10°C/sec or 17%, whichever is greater.

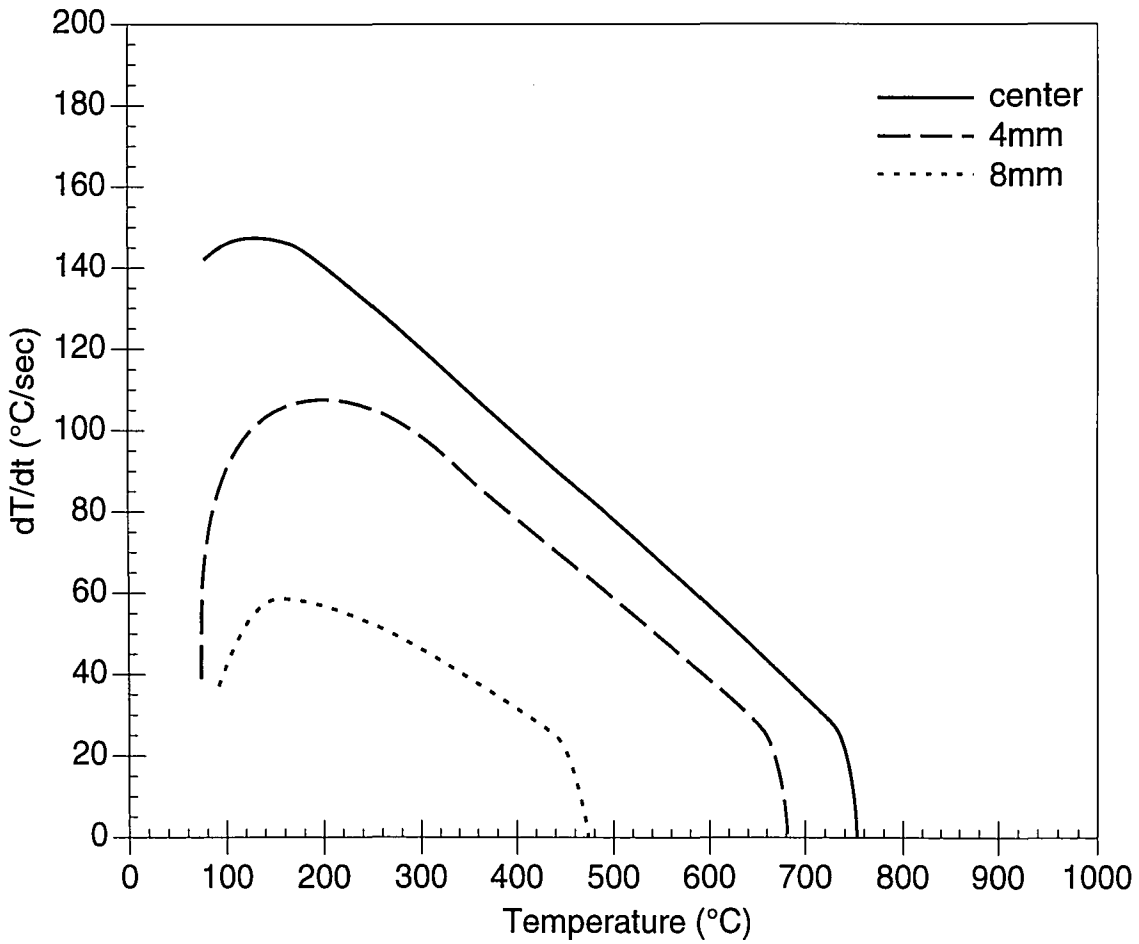

Figure B.7: Thermal cycle heating rate vs. temperature during heating from 25 to 750°C as measured by thermocouples located at 4 mm intervals above the center of the specimen (see Fig. 2.7). Accuracy: ± 10°C/sec or 17%, whichever is greater.

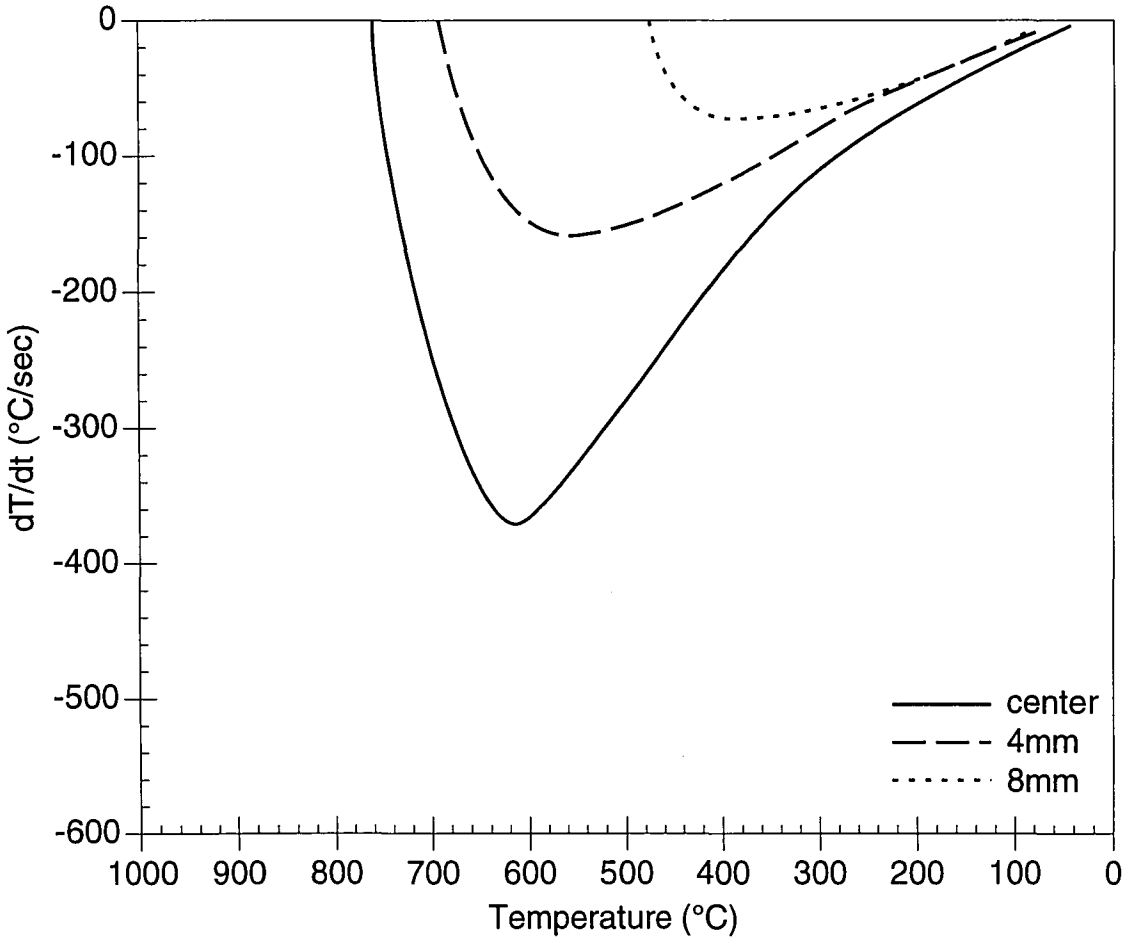

Figure B.8: Thermal cycle cooling rate vs. temperature during cooling from 750 to 25°C as measured by thermocouples located at 4 mm intervals above the center of the specimen (see Fig. 2.7). Accuracy: ± 10°C/sec or 17%, whichever is greater.

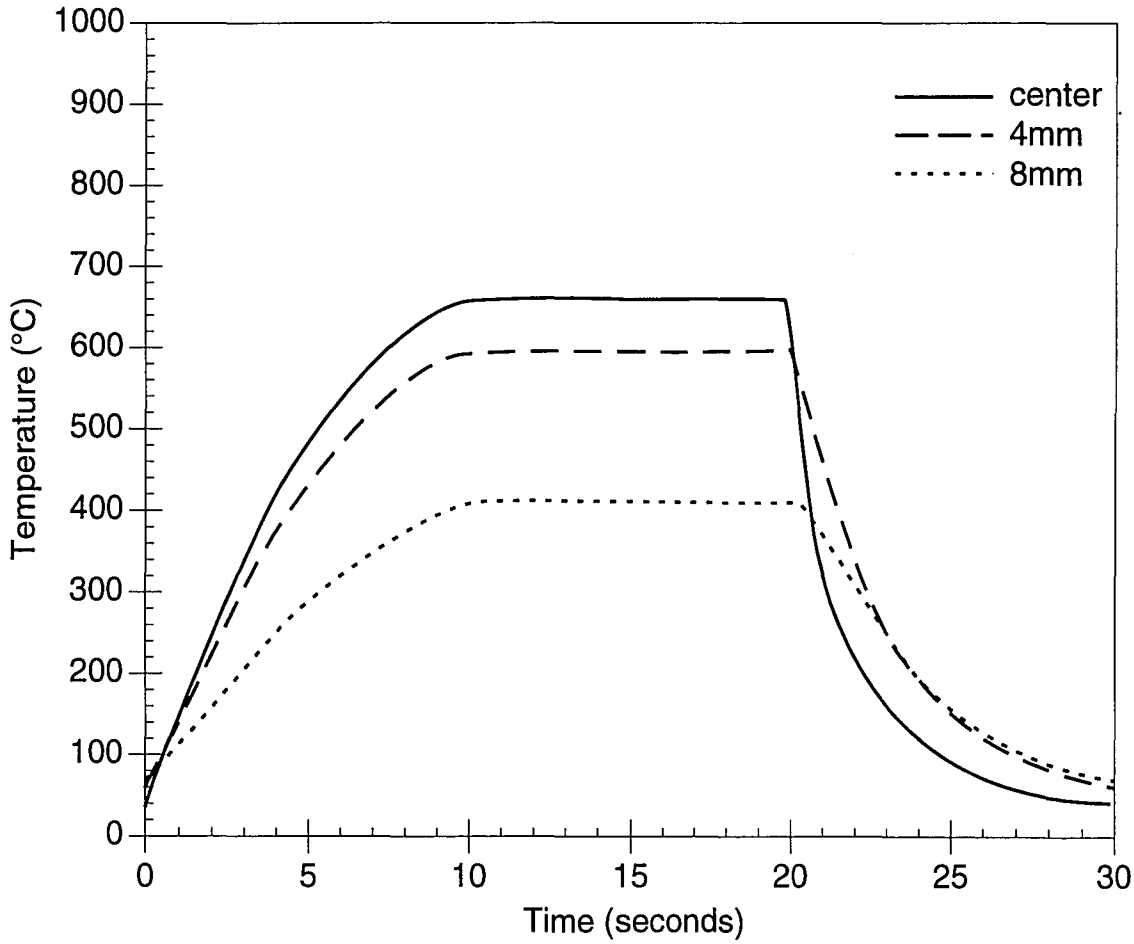

Figure B.9: Thermal cycle temperature profile during cycling between 25 and 650°C as measured by thermocouples located at 4 mm intervals above the center of the specimen (see Fig. 2.7). Accuracy: ± 2.2°C or 0.75%, whichever is greater.

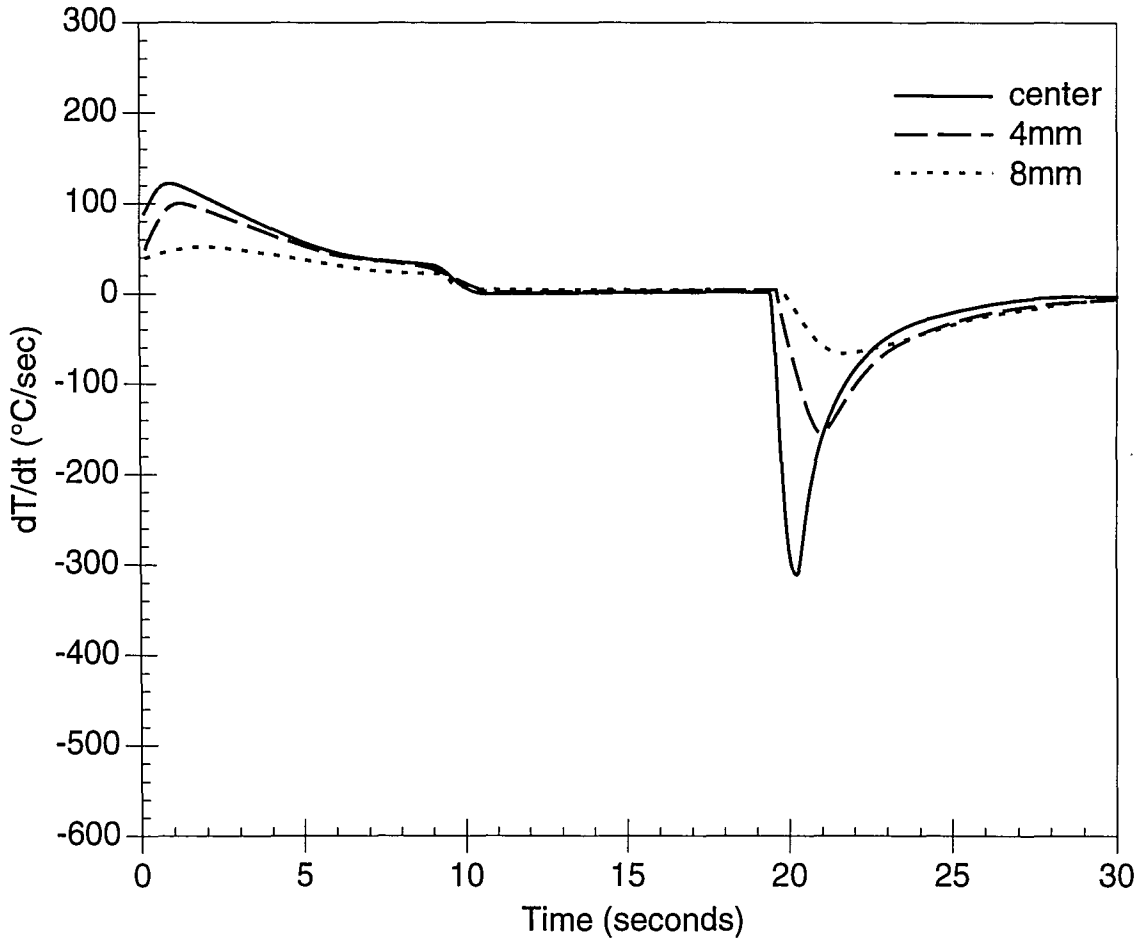

Figure B.10: Thermal cycle heating and cooling rates during cycling between 25 and 650°C as measured by thermocouples located at 4 mm intervals above the center of the specimen (see Fig. 2.7). Accuracy: ± 10°C/sec or 17%, whichever is greater.

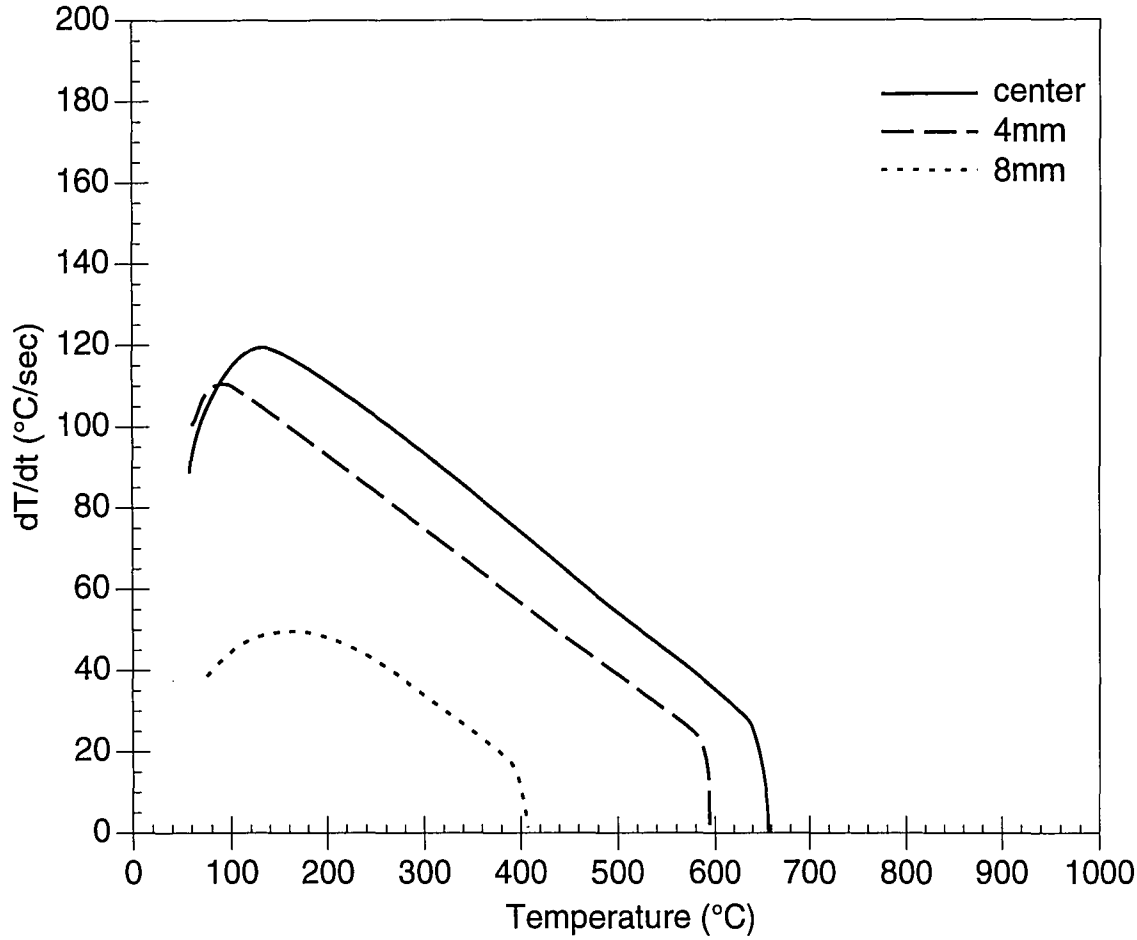

Figure B.11: Thermal cycle heating rate vs. temperature during heating from 25 to 650°C as measured by thermocouples located at 4 mm intervals above the center of the specimen (see Fig. 2.7). Accuracy: ± 10°C/sec or 17%, whichever is greater.

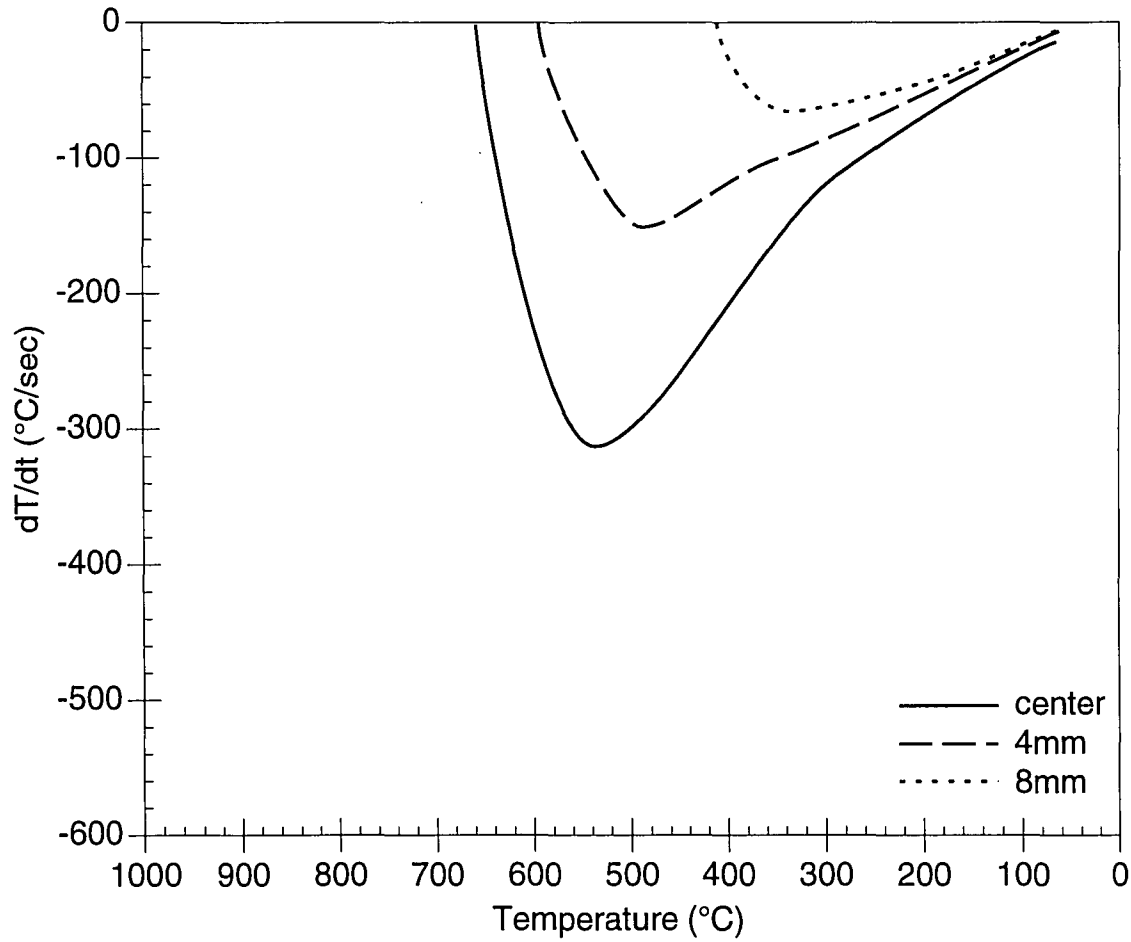

Figure B.12: Thermal cycle cooling rate vs. temperature during cooling from 650 to 25°C as measured by thermocouples located at 4 mm intervals above the center of the specimen (see Fig. 2.7). Accuracy: ± 10°C/sec or 17%, whichever is greater.

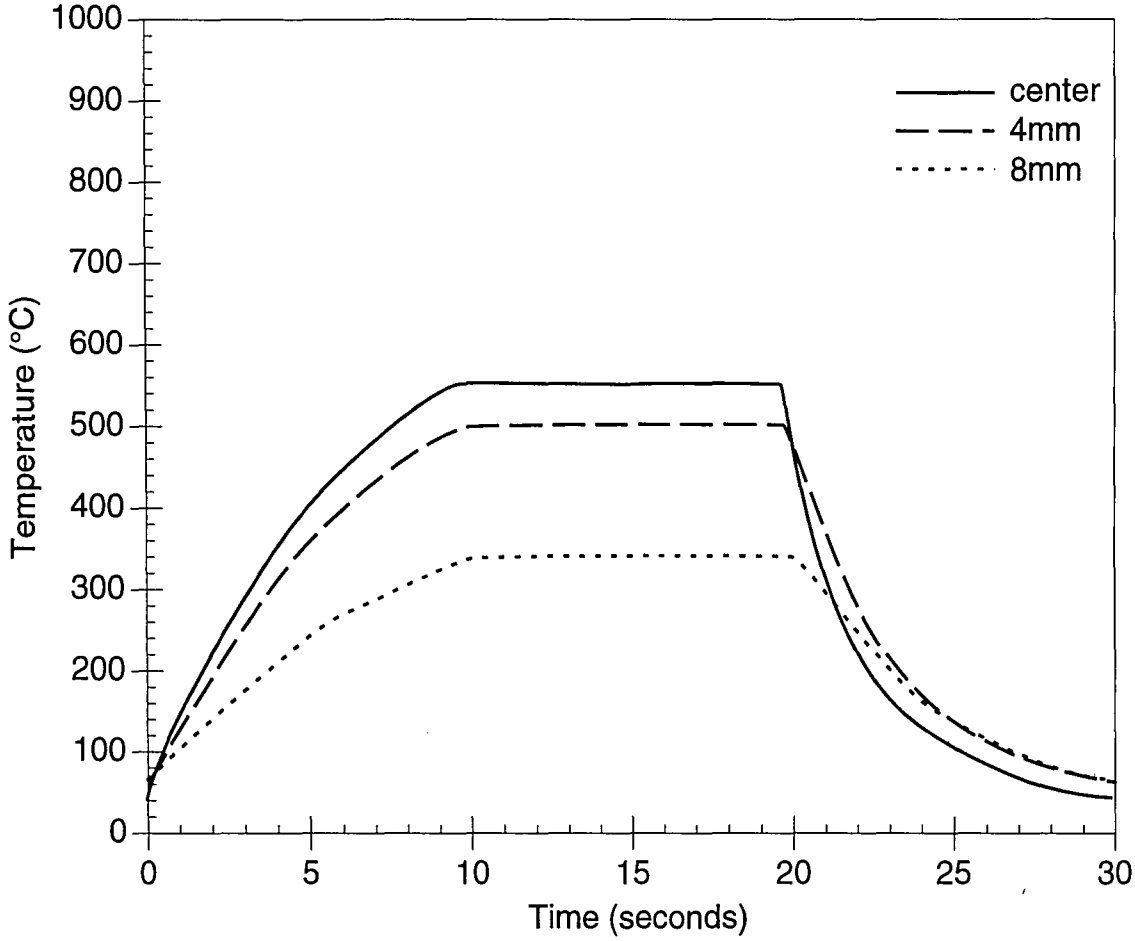

Figure B.13: Thermal cycle temperature profile during cycling between 25 and 550°C as measured by thermocouples located at 4 mm intervals above the center of the specimen (see Fig. 2.7). Accuracy: ± 2.2°C or 0.75%, whichever is greater.

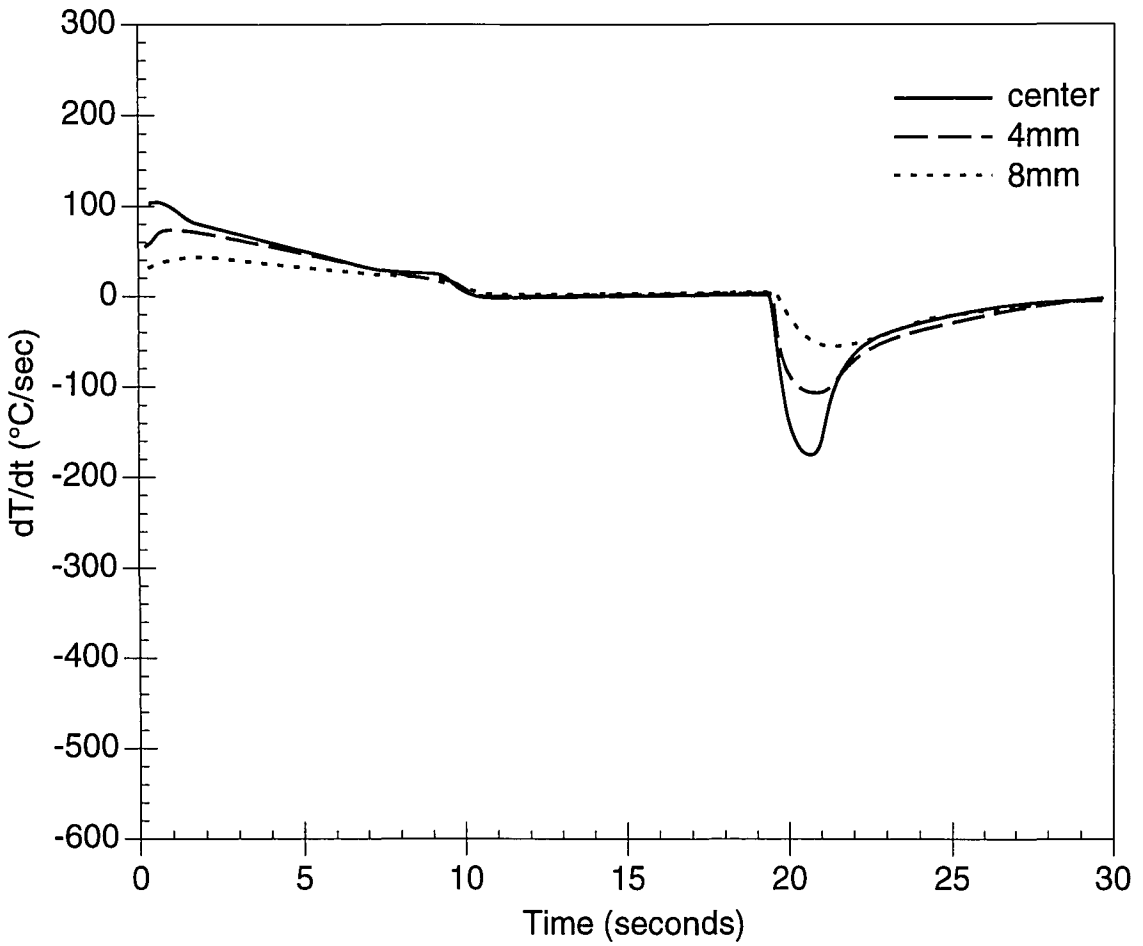

Figure B.14: Thermal cycle heating and cooling rates during cycling between 25 and 550°C as measured by thermocouples located at 4 mm intervals above the center of the specimen (see Fig. 2.7). Accuracy: ± 10°C/sec or 17%, whichever is greater.

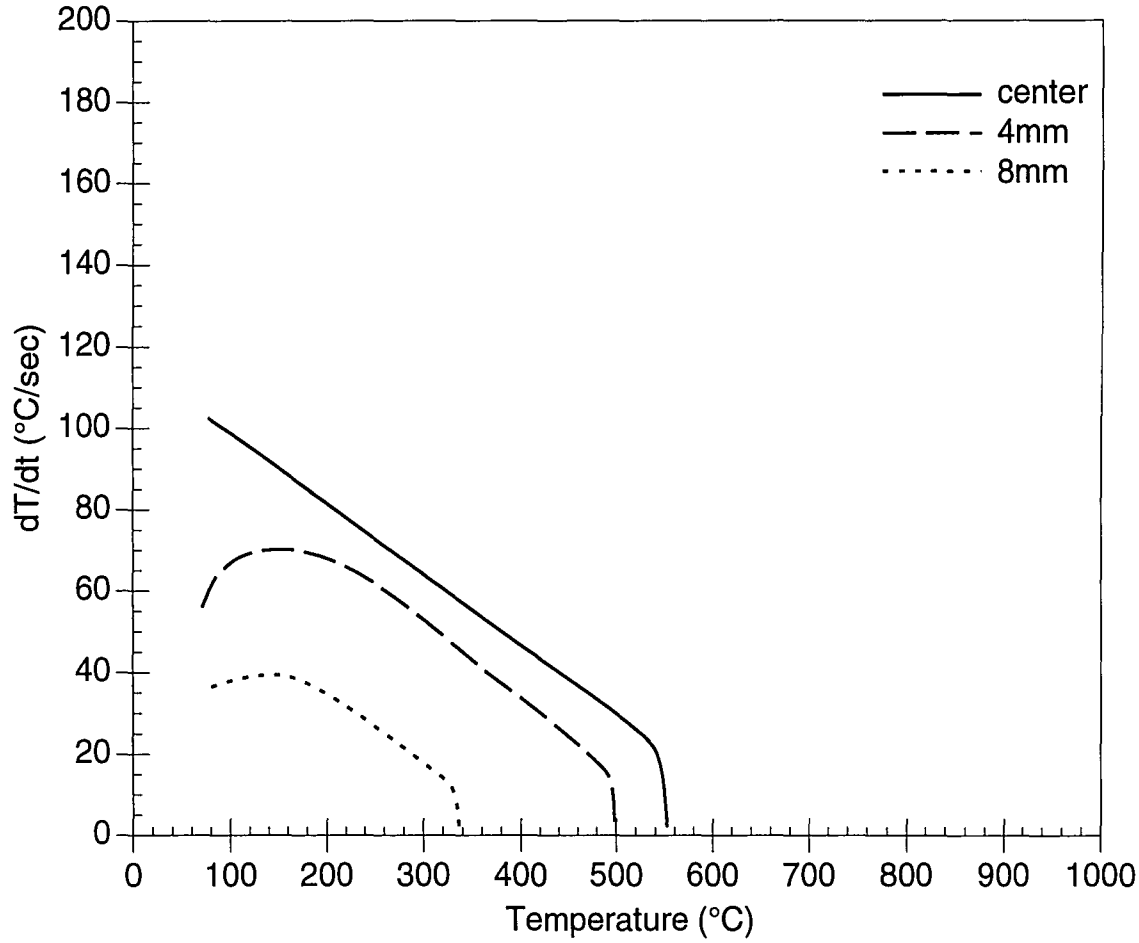

Figure B.15: Thermal cycle heating rate vs. temperature during heating from 25 to 550°C as measured by thermocouples located at 4 mm intervals above the center of the specimen (see Fig. 2.7). Accuracy: ± 10°C/sec or 17%, whichever is greater.

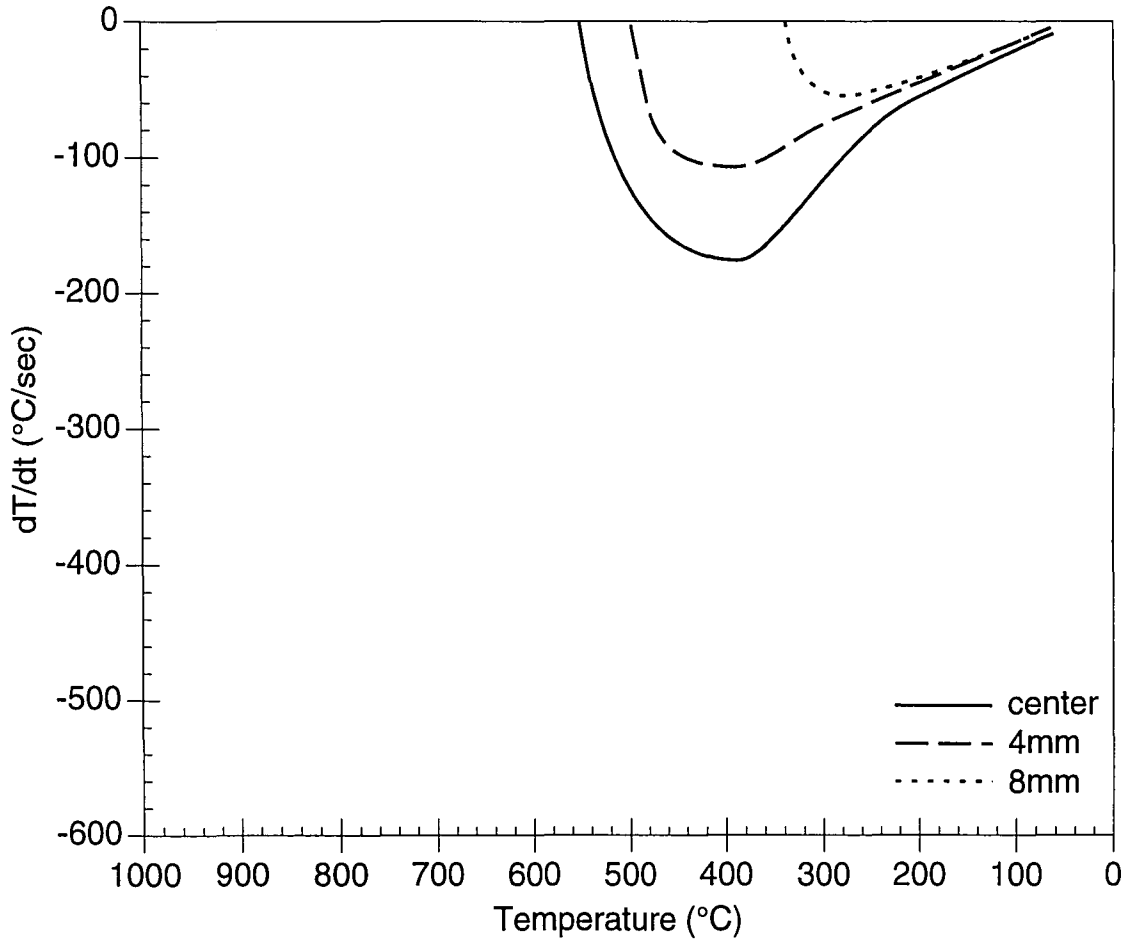

Figure B.16: Thermal cycle cooling rate vs. temperature during cooling from 550 to 25°C as measured by thermocouples located at 4 mm intervals above the center of the specimen (see Fig. 2.7). Accuracy: ± 10°C/sec or 17%, whichever is greater.

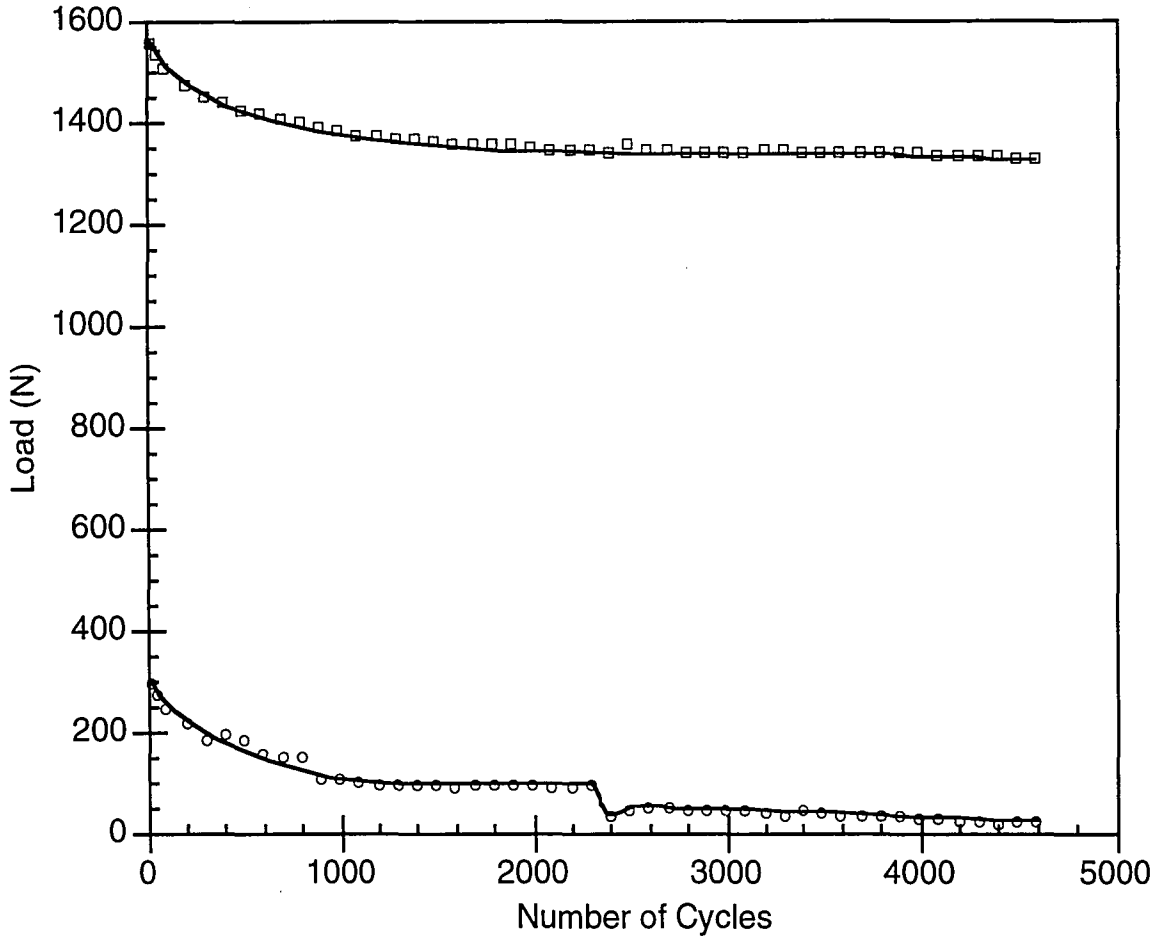

Figure B.17: Typical load drift of the maximum and minimum loads over the course of a test cycling between 25 and 900°C. Jumps in the load are due to adjustments in temperature as it drifted out of the ± 10°C tolerance. Accuracy: ±0.5%.

VITA

William David Dunfee was born on January 16, 1969 in Abington, Pennsylvania to Darlene H. and William S. Dunfee. He earned his Bachelor of Science in Mechanical Engineering from Drexel University in Philadelphia, Pennsylvania in June 1992. While at Drexel, he participated in its co-operative education program, spending a total of 18 months in industry working for American Meter Company and then Instrumentation Technology Associates, Inc. (ITA). After the completion of his co-op, he continued part time and later as a consultant for ITA, gaining experience in the aerospace industry through designing, testing and operating materials processing equipment which conducted experiments aboard the Space Shuttle.

Upon graduation from Drexel, William continued his studies at Lehigh University under a Baldwin fellowship in pursuit of a Master of Science Degree in Applied Mechanics. Under the guidance of Dr. Robert P. Wei, he studied the environmentally enhanced thermal fatigue of gamma-based titanium aluminides. Part of the results of this thesis research was presented at the 1993 TMS fall meeting under the title of "Thermal Fatigue of γ-Titanium Aluminide in Hydrogen". A technical paper was prepared accordingly and has been accepted to be included in the proceedings of the TMS Symposium on Fatigue and Fracture of Ordered Intermetallic Materials. Two additional papers entitled "Thermal Fatigue Testing of γ-Titanium Aluminide in Hydrogen and Air" and "Thermal Fatigue of γ-Titanium Aluminide in Gaseous Environments" have been accepted for presentation at the ASTM Second

Symposium on Thermal-Mechanical Fatigue Behavior of Materials and the 1994 TMS fall meeting, respectively.

William is a member of both the Phi Eta Sigma National Honor Society and Tau Beta Pi Engineering Honor Society.

END

OF

TITLE